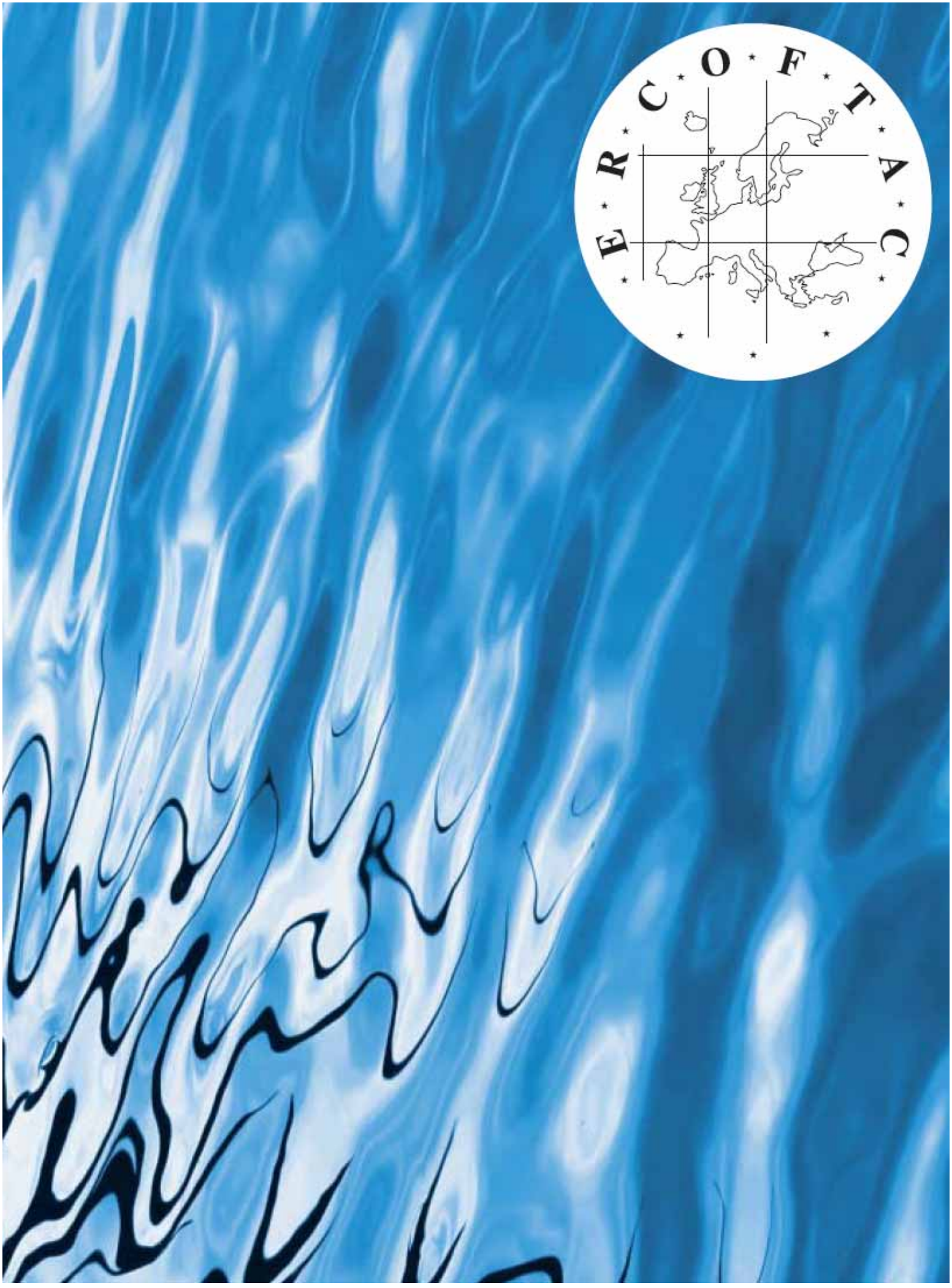
E · R · C · O · F · T · A · C

European Research Community On Flow, Turbulence and Combustion

ERCOFTAC is a leading European association of research, education and industry groups in the technology of flow, turbulence and combustion. The main objectives of ERCOFTAC are: To promote joint efforts of European research institutes and industries with the aim of **exchanging technical and scientific information**; to promote **Pilot Centres** for collaboration, stimulation and application of research across Europe; to stimulate, through the creation of **Special Interest Groups**, well-coordinated European-wide research efforts on specific topics; to stimulate the creation of advanced **training** activities; and to be influential on funding agencies, governments, the European Commission and the European Parliament.

www.ercoftac.org

ERCOFTAC Bulletin 78, March 2009

TABLE OF CONTENTS

SPECIAL THEME

'Environmental Fluid Mechanics'

EDITOR Borhani, N.

EDITORIAL BOARD Dick, E.
Elsner, W.
Geurts, B.J.

DESIGN & LAYOUT Borhani, N.

CIRCULATION 850 copies

SUBSCRIPTIONS AND SUBMISSIONS

ERCOFTAC Bulletin
ERCOFTAC Coordination Centre
EPFL-STI-IGM-ERCOFTAC
ME G1 465, Station 9
CH-1015 Lausanne VD
Switzerland

Tel: +41 21 693 3503
Fax: +41 21 693 5960
Email: ercoftac@epfl.ch

HOSTED, PRINTED & DISTRIBUTED BY

ÉCOLE POLYTECHNIQUE
FÉDÉRALE DE LAUSANNE

NEXT *ERCOFTAC* EVENTS

ERCOFTAC Spring Festival

4th May 2009

Budapest University of Technology and Economics, Budapest, Hungary.

ERCOFTAC SPC, IPC & EC Meetings

5th May 2009

Budapest University of Technology and Economics, Budapest, Hungary.

Best Practice Guidelines for Computational Fluid Dynamics of Dispersed Multi-Phase Flows

Editors

Martin Sommerfeld, Berend van Wachem
&
René Oliemans

The simultaneous presence of several different phases in external or internal flows such as gas, liquid and solid is found in daily life, environment and numerous industrial processes. These types of flows are termed multiphase flows, which may exist in different forms depending on the phase distribution. Examples are gas-liquid transportation, crude oil recovery, circulating fluidized beds, sediment transport in rivers, pollutant transport in the atmosphere, cloud formation, fuel injection in engines, bubble column reactors and spray driers for food processing, to name only a few. As a result of the interaction between the different phases such flows are rather complicated and very difficult to describe theoretically. For the design and optimisation of such multiphase systems a detailed understanding of the interfacial transport phenomena is essential. For single-phase flows Computational Fluid Dynamics (CFD) has already a long history and it is nowadays standard in the development of air-planes and cars using different commercially available CFD-tools.

Due to the complex physics involved in multiphase flow the application of CFD in this area is rather young. These guidelines give a survey of the different methods being used for the numerical calculation of turbulent dispersed multiphase flows. The Best Practice Guideline (BPG) on Computational Dispersed Multiphase Flows is a follow-up of the previous ERCOFTAC BPG for Industrial CFD and should be used in combination with it. The potential users are researchers and engineers involved in projects requiring CFD of (wall-bounded) turbulent dispersed multiphase flows with bubbles, drops or particles.

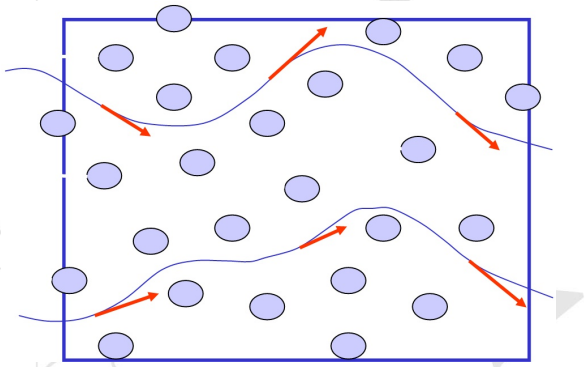

Table of Contents

* * *

Copies of the Best Practice Guidelines can be acquired electronically from the website:

www.ercoftac.org

Or from:

Ms. Anne Laurent,
ADO-ERCOFTAC,
Ave. Franklin Roosevelt 5,
B-1050 Brussels, Belgium.

The price per copy is €90, €45 and €30 for ERCOFTAC industry, academic-and student members, respectively; and €180 for non-members.

SPECIAL THEME

Environmental Fluid Mechanics

Bernard J. Geurts

Chairman of Ercoftac's Large Eddy Simulation Special Interest Group.

Multiscale Modeling and Simulation, Mathematical Sciences,
University of Twente, P.O. Box 217, 7500 AE Enschede, The Netherlands.
Anisotropic Turbulence, Fluid Dynamics Laboratory, Eindhoven University of Technology,
P.O. Box 513, 5600 MB Eindhoven, The Netherlands.

b.j.geurts@math.utwente.nl

Ever since images of Earth as a unique and isolated spot in the universe became available from missions to the Moon some forty years ago, we have realized more clearly the limitations of our habitat. The recently developed Google-Earth system has intensified and modernized this awareness. It brought amazement about Earth's natural beauty to the general public, as well as impressed a sense of vulnerability of our Planet as a single, highly connected and interdependent system.

Accelerated climate change and the ever-increasing pressure on the natural environment due to human activities, provide a strong and timely incentive for research in the field of environmental fluid mechanics (EFM). The nature of this problem area, and the significant problems associated with precise field-experimentation, place a strong emphasis on accurate modeling and simulation, and, on physical scale-experiments, to clarify basic transport mechanisms and nonlinear interactions.

Turbulence plays a dominant role in questions related to environmental dispersion processes, including heat and mass transfer in transport of sediment, nutrients and toxic agents. The major difficulty in such flows lies in the interaction of length- and time scales of very different orders of magnitude, requiring multiscale modeling of the phenomena. This field of study requires integration of a variety of scientific and engineering disciplines in order to achieve meaningful contributions.

In this issue of the ERCOFTAC Bulletin several recent developments in computational modeling and physical experimentation relevant to EFM will be presented. The dispersion problem of aerosol in the atmosphere over urban areas is considered in two separate contributions (Castro and Xie (Southampton), and, Grinstein, Bos and Dey (Los Alamos)). Vila and Van den Dries (Wageningen) consider an extension of this problem to reacting flows in a turbulent atmospheric boundary layer. Gobert, Le Duc and Manhart (TU Munich), and, Pospisil and Jicha (Brno) present basic small-scale modeling for the motion of dispersed particles in turbulent flow. Luethi et al. (ETHZ) discuss the effect of rotation on the 2D-3D structure of turbulent flow, based on detailed particle tracking velocimetry (PTV); this is particularly important for understanding transport processes on large atmospheric and oceanic scales. Lakehal (Ascomp) presents a computational study on the building-block exchange process between the atmosphere and the upper layers of the oceans, which is an important area of improvements of global climate models. On the scale of coastal flows, Armenio and Roman (Trieste) present a computational modeling study of dispersion and exchange processes in the Bay of Trieste. Finally, the general problem of sediment transport is illustrated by a contribution by Uijttewaal (Delft), focusing on shallow mixing layers relevant to river systems, and, by Baas and Best (Bangor and Illinois), presenting experimental findings on the motion of dense clay suspensions over smooth and rough river beds.

It is hoped that the contributions in this ERCOFTAC Bulletin will stimulate further research and collaboration in Environmental Fluid Mechanics, and thus contribute to answering challenges of modern times in which we live.

www.ercoftac.org

LES for Modelling the Urban Environment

I.P. Castro & Z-T. Xie

School of Engineering Sciences, University of Southampton, UK.
i.castro@soton.ac.uk

1 Introduction

For many obvious reasons there is increasing interest in being able to predict flow and pollutant dispersion within urban environments, particularly regions like city centres. Current meteorological codes used to compute weather systems do not have grid sizes much below O(10) km in the horizontal, with perhaps a few points vertically within the atmospheric boundary layer. They are usually also not designed to be able to cope with high topological gradients (ground slopes). For these reasons, among others, very different computational approaches are required for computing flows at scales down to O(1)m, say, and in regions containing very many (usually) sharp-edged buildings. Such areas might have domain sizes of hundreds of meters and have been termed 'the street scale' region (see [1], where it was also suggested that the entire city domain be termed the 'city scale', with 'neighbourhood scale' for regions in between street scale and city scale). There are increasing numbers of full-scale field campaigns in which velocities and concentrations are measured within urban areas (see [13] for a recent example). Whilst these can be extremely useful, they are inevitably limited in terms of the data obtained and the extent to which conclusions about the physical processes can be unambiguously made. Computational approaches arguably have much greater potential in this regard. However, even the most optimistic projections of available computer power over the next few decades suggest that it is very unlikely that a single computational tool could be created for accurate modelling of such street scale regions simultaneously with complete city scale regions, and beyond to mesoscale domains.

One of the UK Natural Environment Research Council's collaborative centres is the National Centre for Atmospheric Science, whose Weather Directorate's strategy includes the objective of developing tools to allow prediction of flow, turbulence and dispersion within urban environments. In 2004 a possible route towards this goal was identified, having two major constituent parts. It was recognised that (i) standard RANS modelling was likely to be inadequate for street-scale flows, (ii) LES techniques represented perhaps the lowest-order approach which has any hope of capturing those genuine unsteady features in such flows which crucially affect dispersion processes, and (iii) modern commercially available engineering-type codes have much more sophisticated numerics and meshing strategies than even a decade ago, and have sophisticated pre- and post-processor tools. So rather than developing new versions of meteorological-type codes, the first part of the approach was to validate the use of commercially available codes FLUENT, STAR-CD or CFX for, initially, neutrally stable street scale flows, using available experimental data and (more limited) DNS data for boundary layer flows over very rough surfaces comprising arrays of cuboid obstacles. The second strand was to develop appropriate ways of using the output from meteorological codes (like the UK Met Office's Unified Model) to provide dynamic boundary conditions for the street scale computation.

This paper presents some of our most important conclusions from the work undertaken thus far in the context of the first of these two strands. We have found (i) that, perhaps surprisingly at first sight, LES for flows over such complex surfaces is in fact less technically demanding than for smooth surfaces at similar Reynolds numbers (the flow dynamics are dominated by obstacle-scale motions rather than thin boundary layers), (ii) that a highly efficient filter technique can be used to provide appropriate turbulence inlet conditions, and (iii) that the overall approach can yield flow and concentration results in good agreement with experimental data. §2 outlines the basic numerical methods used and shows some typical validation results whilst §3 presents further results for a generic urban-type surface. The final section, §4, presents some results obtained for a real case an extensive 'street-scale' region of central London for which flow, turbulence and scalar concentration data are available from both the site itself and a wind tunnel model.

2 Techniques and validation

In view of space limitations, only a brief description of the numerical methods is given here; more extensive details can be found in [21], hereafter denoted by XC.

The filtered continuity and Navier-Stokes equations are written as follows,

$$\begin{aligned} &\frac{\partial u_i}{\partial x_i} = 0 \\ &\frac{\partial u_i}{\partial t} + \frac{\partial u_i u_j}{\partial x_j} = -\frac{1}{\rho}\left(\frac{\partial p}{\partial x_i} + \delta_{i1}\frac{\partial \langle P\rangle}{\partial x_1}\right) \\ &\qquad\qquad + \frac{\partial}{\partial x_j}\left(\tau_{ij} + \upsilon\frac{\partial u_i}{\partial x_j}\right) \end{aligned} \tag{1}$$

The dynamical quantities, u_i, p are resolved-scale (filtered) velocity and pressure respectively and τ_{ij} is the subgrid-scale (SGS) Reynolds stress. δ_{i1} is the Kronecker-delta and υ is the kinematic viscosity. $\partial\langle P\rangle/\partial x_1$ is the driving force, a constant streamwise pressure gradient. For the sub-grid stresses the classical Smagorinsky SGS model, or a very similar model discussed in [24], was used and in the near-wall region the Lilley damping function was also applied. This reduces the filter width within the viscosity-affected region so that energy-carrying eddy sizes scale appropriately.

For complex geometries like those in view here, where multiple separation and attachment processes occur, it is impossible to satisfy the common criterion that the distance between the centroid of the first cell in (local) wall units should be of order unity. However, one of the conclusions of our earlier work is that this is, in fact, not necessary. A typical urban-like surface is shown in figure 1 and it turns out that the drag of such surfaces is

almost entirely form drag. The turbulent motions generated at scales of O(h), where h is an appropriate dimension of the typical roughness element, are dominant and it is not necessary to resolve fine details of the individual (and very thin) boundary layers on each of the element surfaces. This means, too, that applying standard wall-law conditions (i.e. log-law parameters for the near-wall points) is quite adequate, even though it is fundamentally inappropriate as there are probably very few, if any, regions on the element surfaces where log-law conditions actually apply in practice.

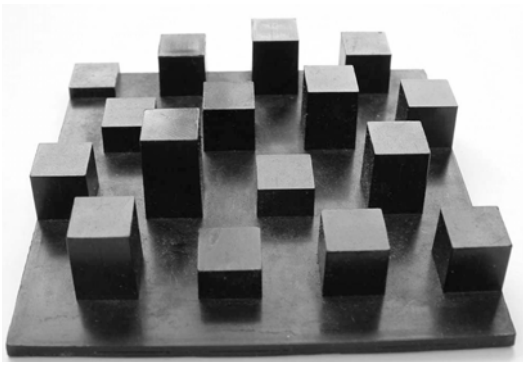

Figure 1: *Random height roughness array.*

However, it is necessary to resolve each of the roughness elements adequately (see also [20, 11, 12]). XC showed that, in the context of a staggered array of cubical elements (arranged as in fig.1 but with each element a cube of height h), structured meshes, uniform in the region of the roughness elements, with around 15-20 nodes over the height of the cube, yielded mean velocity, surface pressure and turbulence data in good agreement with both experimental data and fully-resolved DNS results [3]. We will show below results of computations for the surface shown in figure 1. A computational domain embodying four of the complete units shown in figure 1 was used, in a 2x2 arrangement, with the oncoming flow normal to the elements at the top of the view and periodic conditions applied in the streamwise and lateral directions. Note that each of the four units contains 16 elements, whose heights are distributed normally, with a standard deviation of 0:3h where h is the average height of the elements. Experimental data are available for this surface from a comprehensive programme of measurements in a wind tunnel boundary layer developing over the surface (with $h = 10$mm, [2]). Stress free conditions were applied at the top of the domain, which was at $z/h = 10$, where $z = 0$ is the bottom surface. The computations thus represented fully-developed flow in a half-channel - practically easier to compute than a boundary layer flow and common in LES computations of atmospheric boundary layers (e.g. [16, 19]). If the emphasis is on the roughness sub-layer and canopy regions, channel computations with a domain height not too dissimilar to the experimental boundary layer thickness are quite adequate (see also XC).

For time-stepping, a second-order backward implicit scheme was used with a time step of $0.002T$ ($T = h/u_\tau$ where u_τ is the usual friction velocity appropriate for the entire surface - related therefore to the total surface drag). The initial duration of most of the runs was $150T$, whereas the subsequent averaging duration for all the statistics was approximately $300T$. [3] found that for their array of uniform cubes, with a spanwise domain size of $8h$, the converging flow contained quite strong, large-scale structures having longitudinal vorticity. These rolls, typically having a spanwise wavelength of about $4h$, gave rise to significant dispersive stresses (i.e. stresses which arise from spatial inhomogeneities in the time-averaged fields) and adequate time-averaging was necessary to resolve statistics unequivocally (i.e. to reduce these dispersive stresses to zero above the near-wall region). They found that an averaging time of about $400T$ was necessary. For the present surface, there was little evidence of such rolls, partly no doubt because of the more random nature of the surface but also perhaps because the spanwise domain was limited to two repeating units (compared with four in [3] and see also [5, 6]). So the $300T$ averaging time in the present case was quite suffcient for obtaining converged statistics.

For spatial differencing we used either a deferred correction second-order central scheme (for the hexahedral mesh run with FLUENTv.6) or the second-order monotone advection and reconstruction scheme (MARS, for the polyhedral mesh used with STAR-CD4). The former employed 2.3 million cells, with 16x16x16 per hxhxh in the near-wall region, and the latter had 1.3 million cells with 13x13x13 per hxhxh in the near-wall region. It must be emphasized that provided discretisation of all terms in Eq.(1) was at least second-order accurate in both space and time, results did not depend perceptibly on the particular LES code employed, nor indeed on the particular mesh chosen provided there was enough resolution in the wall region (as discussed above, with smallest grid sizes no greater than around 0:06h near the building edges). It is known that polyhedral meshing is much more flexible than the alternatives for complex geometries and it is also more accurate and less memory consuming than the widely used tetrahedral mesh (see, for example, [17] and note also [4]). Figure 2 shows views of the two meshes used in obtaining the results discussed below.

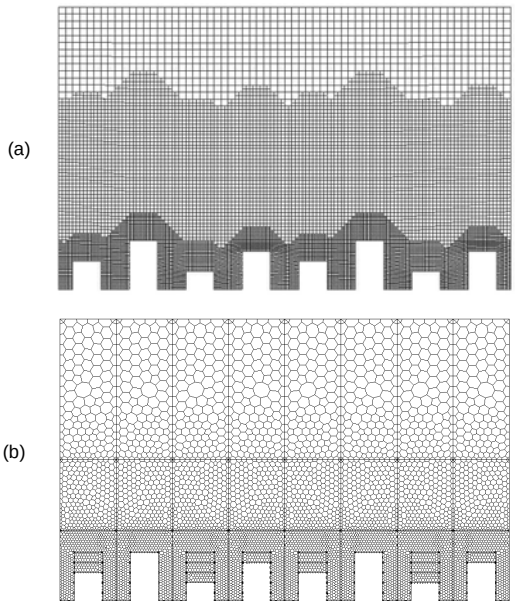

Figure 2: *Side-views of meshes, from a vertical-transverse cut across the tallest element. (a): hexahedral mesh; (b): polyhedral mesh.*

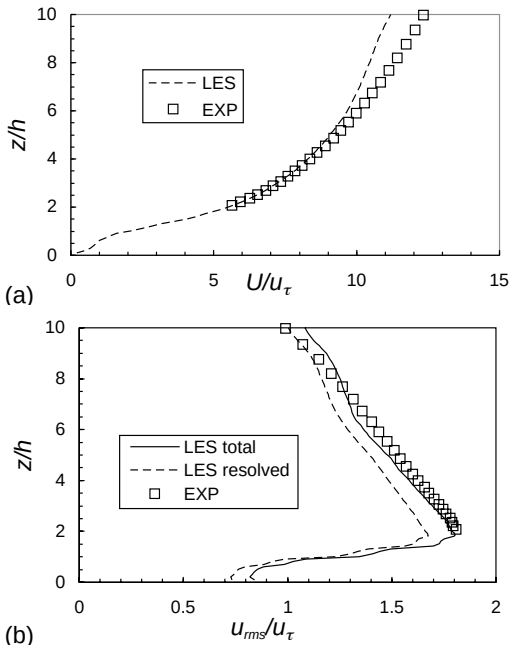

Figure 3: *Vertical profiles of spatially averaged mean velocity (a), axial velocity r.m.s. (b).*

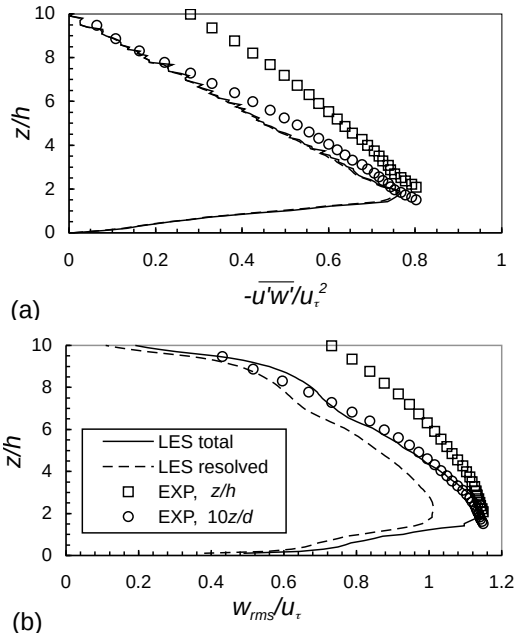

Figure 4: *Vertical profiles of spatially averaged vertical velocity r.m.s. (a) and Reynolds shear stress (b). Open circles refer to the experimental data but have the ordinate scaled by boundary layer thickness, δ=10 rather than h.*

As an example of the extensive validation process undertaken for arrays of both cubical obstacles and the random-height array shown in figures 1, 3 & 4 plot the spatially averaged mean streamwise velocity, velocity r.m.s. and the Reynolds shear stress profiles for the latter case. Periodic conditions were used for inlet and outlet conditions and symmetry at the upper boundary, as discussed earlier. Note that the boundary layer thickness over the wind tunnel array was 137mm, while the depth of the computational domain is 100mm. This causes inevitable differences in the upper region of the domain for the quantities involving the vertical velocity fluctuations (i.e. w_{rms} and $\overline{u'w'}$). Normalising the height by the boundary layer thickness (or domain height) leads to much closer collapse, as shown in figure 4. We emphasise here that although profiles over the entire domain height must clearly depend on the domain height - the latter is essentially a half-channel height - the flow in the roughness sublayer is not strongly dependent on domain height. This was demonstrated in [3] and it allows sensible comparisons with the near-surface region of boundary layer flows over the same roughness, provided the boundary layer thickness is not too much smaller than the computational domain height. Notice also that the sub-grid contributions to the r.m.s. velocities are not insignificant; in figure 3b, for example, good agreement with experiment is obtained only once the sub-grid stress component is included. It is worth mentioning the rather subtle point that whilst it is not possible to calculate the sub-grid energy from the sub-grid stress tensor (whose trace is zero), one can approach the matter the other way around and estimate the sub-grid energy posthoc using the sub-grid model which is supposed to represent the unresolved portion of the energy spectrum. This is what was done to deduce the additional contributions providing the (estimated) total stresses and energy in the figure 3, but we emphasise that it is not strictly exact.

Results obtained within the canopy region (for arrays of cubical obstacles) and axial velocity energy spectra (see [21]) confirmed the deduction made from earlier experimental measurements, that at least as far as the large-scale dynamics which determine the surface drag are concerned, flows over surfaces of these kinds are essentially Reynolds number independent. This is a very different situation than obtains for smooth-surface flows which, as is well-known, provide a severe test for LES approaches; unless the grid is fine enough to allow virtually a DNS-type resolution, some kind of matching to a near-surface RANS approach, or equivalent, has to be employed to surmount the difficulty.

Using LES for typical practical situations (as illustrated later) exacerbates the difficulties posed by having to supply appropriate boundary conditions. Periodic conditions (in the axial direction) are not appropriate for spatially developing flows and, even if the upstream flow may be taken as essentially steady, one requires an efficient method of inserting appropriate small-scale turbulence at the upstream boundary at each time step. A number of methodologies have been developed to achieve this, including 'modified periodic' methods (e.g. [15]), techniques based on proper orthogonal decomposition [10, 8, 18], and synthetic turbulence generation, usually based on filtering methods (e.g. [14]). Many of these are quite expensive in terms of the overheads in computing time needed just to provide inlet conditions.

We have developed a very efficient and fully three-dimensional version of a filter method [22]. It involves supplying appropriately chosen vertical profiles of Reynolds stresses and integral length scales and, in tests using classical turbulent channel flows, was shown not only to be very much more time-efficient than the nearest equivalent previously published [14] but also more efficient in terms of generating fully developed channel turbulence in as short an axial fetch as possible. The computational efficiency arises specifically through assuming an exponential form for the spatial correlation coefficients, so that the new fluctuating velocity field at each time step can be efficiently formed as an appropriate combination of the previous time step's field and a new 2D filtered random field. In fact, at all but the smallest scales, an exponential correlation is rather more physical than alternative forms like the commonly used

Gaussian, so the method is also more physically appealing than many alternatives. As an example of results obtained with the method figure 5 shows profiles of axial mean velocity and rms turbulence, compared with experimental data, for the case of a staggered 25% area coverage array of cubes in a channel. The computations used either periodic conditions or the new, efficient filter method for supplying inlet turbulence (with standard zero-gradient conditions at the downstream boundary). Appropriate in flow stress profiles were used, with considerably simplified profiles of integral length scales (L_x,L_y,L_z for the axial velocity). The results are not very sensitive to the precise values of these scales - changing all three by a factor of two has only marginal effect on the turbulence (fig.5b). However, if they are not specified at all, so that the inlet turbulence has no genuine spatial structure, then the turbulence decays rapidly. Specifying only axial structure via an enforced L_x profile (i.e. with no cross-stream structure so that L_y,L_z are both zero, as done in [9]) is also clearly insufficient. With sensible choices, based on experimental data, the turbulence levels are close to those obtained assuming periodic boundary conditions. The full methodology and validation experiments are presented in [22].

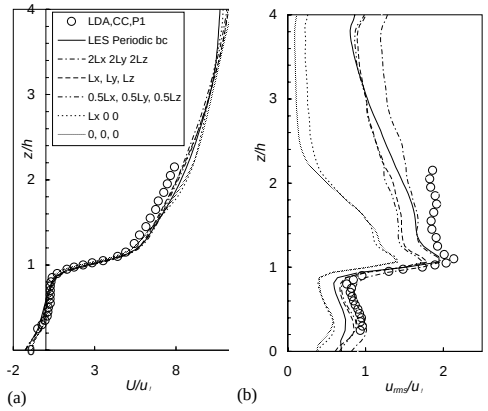

Figure 5: *Influence of integral length scale on mean velocity and turbulence at a typical location though a staggered array of cubes. The domain was 16h in length and 4hx4h in cross-section.*

3 Further results for a generic surface

A number of interesting features have been identified from the LES results obtained over the generic urban-type surface represented by the random-height array shown in figure 1. We comment here on two of these. Firstly, LES allows mean and fluctuating information on the element (building) surface pressures to be obtained. Figure 6 shows mean surface pressures and it is immediately clear that the four tallest elements (one in each of the four identical units within the domain, see §2) experience significantly higher surface pressures on the front face than experienced by the other elements. In fact, it turns out that 22.4% of the total surface drag is provided by these tallest elements - very much higher than might be anticipated solely on the basis of their contribution to the total frontal area 'seen' by the flow. Figure 7 shows variations of the front-to-back pressure difference on each of the 16 elements within one unit, which emphasises the relatively large pressures on the tallest element. Although scalar concentration computations and results cannot be discussed in detail here, figure 6 includes an example of such data: time-averaged pathlines for scalar sources located within the roughness canopy. Time-dependent versions of these are also available of course, and this provides a major motivation for using a genuinely unsteady method like LES for such flows - RANS computations cannot in principle (and do not in practice) yield adequate results of this type.

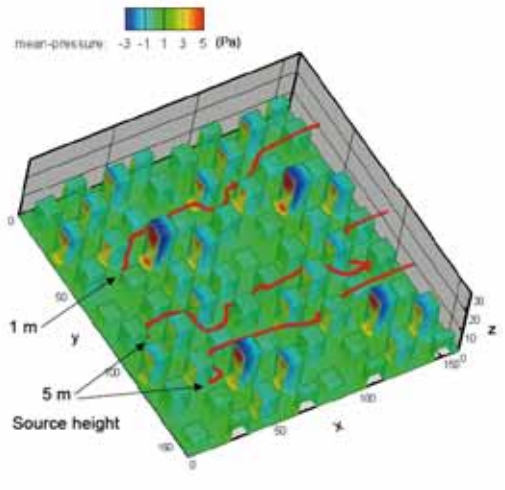

Figure 6: *Surface static pressure contours for the array shown in figure 1.*

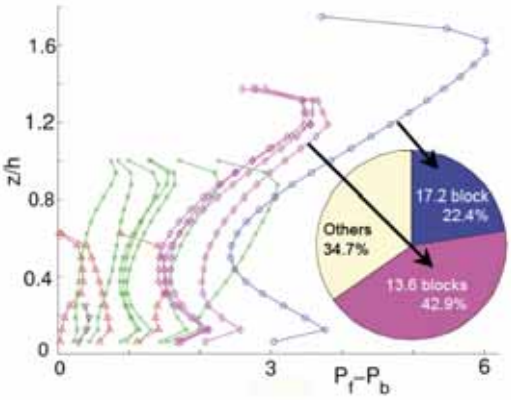

Figure 7: *Normalised profiles of laterally integrated pressure difference between front and back faces of the elements.*

Secondly, it was found that details of the flows around each element are very dependent on element size and location and can be crucially different from those that occur over isolated obstacles. Figure 8 shows mean velocity vectors on a horizontal plane at $z/h = 0.5$ (i.e. in the middle of the canopy region) and on a vertical plane behind the tallest element. Just outboard from the sides of the latter the flow contains a counter-rotating vortex pair, indicated in the bottom view. The sense of the rotation is opposite to what would normally occur for an isolated object of the same shape, for which the cross-stream circulations have the same sense as those in a trailing vortex system behind, for example, a delta wing. The reason for the difference can be identified by considering the flows induced by the somewhat lower (but not equal height) elements located just downstream but, in any case, the results emphasise that even the qualitative behaviour of the flow around a particular object surrounded by others may be entirely different from what might be expected. Detailed studies of the nature of the flow within the canopy region can be found in [5, 23].

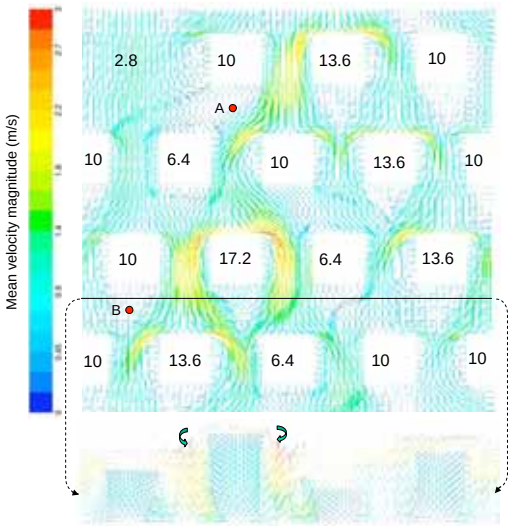

Figure 8: *Mean velocity vectors (U, V) at $z = 0.5h$ (top, flow is from top to bottom) and (V, W) on the vertical plane just behind the tallest element (bottom, looking upstream). Only a small section of the full computational domain (four of the complete 16-block units illustrated in fig.1) is shown. Element heights (in mm) are shown in the upper figure.*

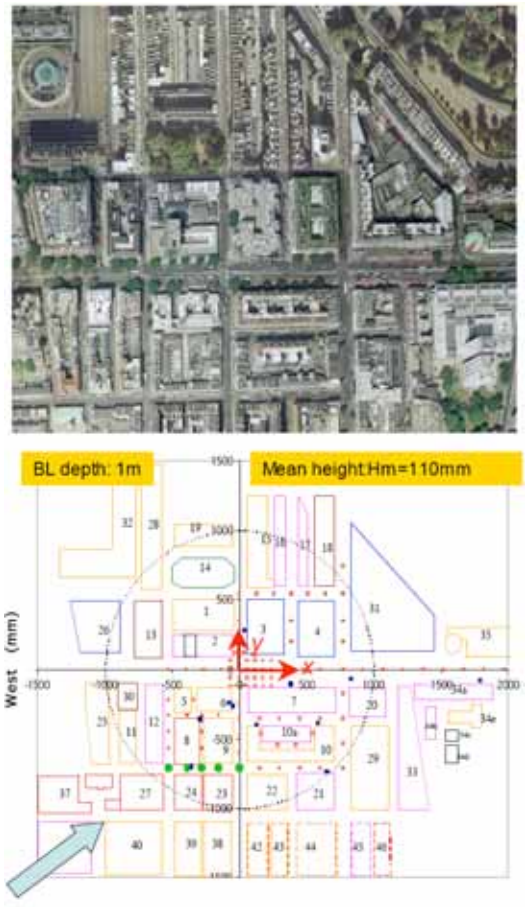

Figure 9: *The DAPPLE site in London (top) and a plan of the 1:200 scale wind tunnel model used at the EnFlo laboratory, University of Surrey (bottom). Note the arrow at bottom left, indicating the mean wind direction. Coordinate dimensions are in mm, with roof heights indicated on each building.*

4 A practical case

We conclude by presenting results from an LES computation of the flow and dispersion over an area of London surrounding the Marylebone Road. This was a site used for an extensive field campaign, with dispersion from various point sources measured at numerous locations under various wind conditions (also measured). A full wind-tunnel model was constructed, allowing a more comprehensive set of data to be obtained for the same source and (simulated) wind conditions. Details can be found at www.dapple.org.uk and a sample publication discussing flow field measurements is [7]. Our computation used a polyhedral mesh of about 1.5 million cells with the smallest ones (adjacent to building surfaces) of around $h = 16$ where h is, again, the average building height. The inlet turbulence generation scheme described earlier was used, with symmetric conditions at the lateral boundaries and a stress-free boundary at the top ($z = 10h$). No 'tweaking' of the inlet turbulence profiles was done; we simply employed profiles appropriate for the simulated atmospheric boundary layer upstream of the wind tunnel model. Figure 9 shows a Google map of the actual site, along with a plan of the wind tunnel model, and figure 10 shows the surface mesh. Because of the much greater detail in the wind tunnel database the computations simulated the wind tunnel situation, using the same Reynolds number and wind direction (shown in figure 9).

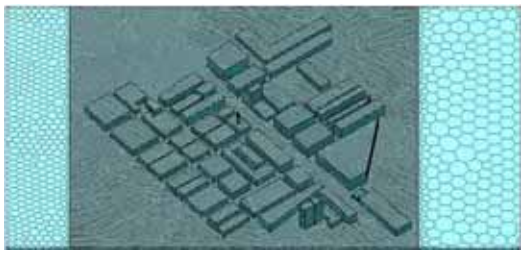

Figure 10: *A section of the polyhedral mesh topology at the ground surface of the computational domain.*

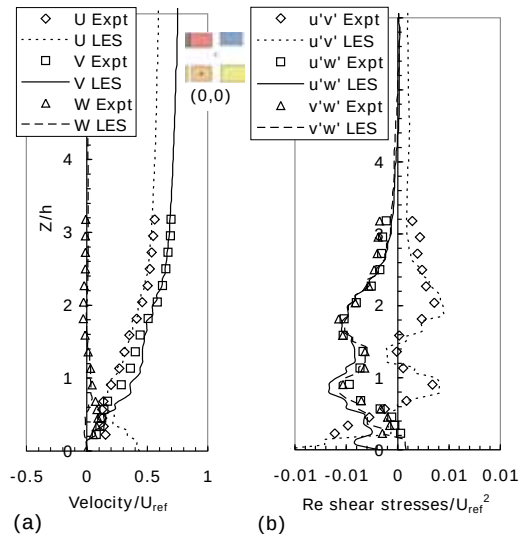

Figure 11: *Velocity (a) and turbulence shear stress (b) profiles at the Marylebone Road - Gloucester Place intersection. Experimental data is from LDA measurements.*

Two sets of results are shown - vertical profiles of velocity and turbulence at the intersection of Marylebone Road and Gloucester Place, figure 11, and the mean

scalar concentration at pedestrian height, figure 13, arising at various locations (shown in figure 12) downwind of a steady source positioned at pedestrian height ($0.07h$, also identified in figure 12). Note first, from figure 11, that there is encouragingly good agreement between experiment and computations for all components of mean velocity and Reynolds stresses. Similar agreement was evident elsewhere in the domain. One of the major motivations for the DAPPLE programme was to acquire scalar concentration data for known meteorological conditions, to allow testing of modelling approaches. So the crucial question in the present context is whether LES yields adequate concentration data. Figure 13, which includes results from corresponding RANS computations, demonstrates that it does. Indeed, it is perhaps remarkable that the time-averaged (normalised) concentrations agree so well with measured values over nearly four orders of magnitude. Note particularly that RANS approaches do not yield such good agreement - there can be differences as great as an order of magnitude at particular locations. Careful scrutiny of all the data showed that this was partly because RANS does not capture the detailed unsteady nature of the flow within the canopy, which is crucial in determining the dispersion processes.

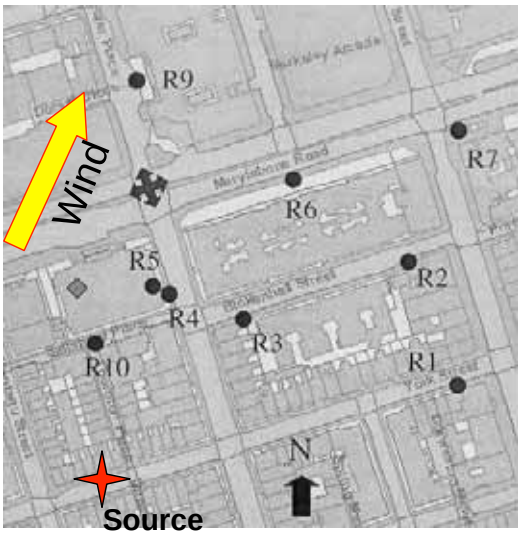

Figure 12: *Plan of the field site. The major intersection is shown with a cross at left and the source location is also shown - bottom left. Wind tunnel (and field) receptor locations are numbered R1-10 and shown in the plan, except R8, which is further down Marylebone Road beyond the top right of the view.*

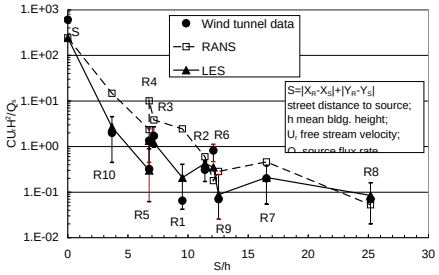

Figure 13: *Scalar concentration at $z/h = 0.25$ as function of normalised 'walking distance' (S/h) from the source.*

It is concluded that appropriately designed LES approaches have great potential for modelling environmental flows, particularly perhaps those in urban environments. Whilst space has not permitted a discussion of how these street-scale computations can be driven by large-scale fluctuations arising from mesoscale processes, we have already implemented a scheme allowing such fluctuations to drive the input turbulence formulation. There is also, it seems, great promise for this important aspect of the overall approach.

Acknowledgements

Thanks are due to the UK Natural Environment Research Council, who funded much of the work summarised in this paper through NCAS grants DST/26/39 and RH/H12/38. Computations were performed on the university of Southampton's IRIDIS system.

References

[1] Britter R.E. & Hanna S.R., Flow and dispersion in urban areas, Ann. Rev. Fluid Mech. 35, 469-496, 2003.

[2] Cheng H. & Castro I.P., Near wall flow over urban-like roughness, Boundary-Layer Meteorol. 104, 229-259, 2002.

[3] Coceal O., Thomas T.G., Castro I.P. & Belcher S.E., Mean flow and turbulence statistics over groups of urban-like cubical obstacles, Boundary Layer Meteorol., 121, 491519, 2006.

[4] Choudhury D, Kim S.E., Makarov B.P. & Carey C., Improved numerical methods for CFD solutions on unstructured meshes, ERCOFTAC bulletin 62, 13-18,2004.

[5] Coceal O., Thomas T.G. & Belcher S.E., Spatial variability of flow statistics within regular building arrays, Boundary Layer Meteorol., 2007a.

[6] Coceal O., Dobre, A., Thomas T.G. & Belcher S.E., Structure of turbulent flow over regular arrays of cubical roughness, J. Fluid Mech., 589, 375-409, 2007b.

[7] Dobre A., Arnold S.J., Smalley R.J., Boddy J.W.D., Barlow J.F., Tomlin A.S. & Belcher S.E., Flow field measurements in the proximity of an urban intersection in London, UK. Atmos. Environ. 39, 4647-4657, 2005.

[8] Druault P., Lardeau S., Bonnet J.-P., Coiffet F., Delville J., Lamballais E., Largeau J.F. & Perret L., Generation of three-Dimensional turbulent inlet conditions for large-eddy simulation, AIAA J. 42(3) 447-456, 2004.

[9] Hanna S.R., Tehranian S., Carissimo B., Macdonald R.W. & Lohner R., Comparisons of model simulations with observations of mean flow and turbulence within simple obstacle arrays, Atmos. Environ. 36, 5067-5079, 2002.

[10] Johansson P.S. & Andersson H.I., Generation of in flow data for inhomogeneous turbulence, Theor. and Comput. Fluid Dyn., 18, 371389, 2004.

[11] Kanda M., Large-Eddy Simulations of the effects of surface geometry of building arrays on turbulent organised structures, Boundary Layer Meteorol. 118. 151-168, 2006.

[12] Kanda M., Moriwaki R. & Kasamatsu F., Large-eddy simulation of turbulent organized structures within and above explicitly resolved cube arrays, Boundary Layer Meteorol. 112, 343-368, 2004.

[13] Kastner-Kline P. & Rotach M.W., Mean flow and turbulence characteristics in an urban roughness sublayer, Boundary Layer Meteorol. 111, 55-84, 2004.

[14] Klein M., Sadiki A. & Janicka J., A digital filter based generation of in flow data for spatially developing direct numerical simulation or large eddy simulation, J. Comp. Phys. 186, 652-665, 2003.

[15] Lund T., Wu. & Squires D., Generation of turbulent in flow data for spatially developing boundary layer simulation, J. Comp. Phys., 140, 233-258, 1998.

[16] Moeng C.-H., A Large-Eddy Simulation model for the study of planetary boundary layer turbulence, J. Atmos. Sci. 41, 2052-2062, 1984.

[17] Peric M., Flow simulation using control volume of arbitrary polyhedral shape, ERCOFTAC bulletin 62, 25-29, 2004.

[18] Perret L., Delville J., Manceau R. & Bonnet J.P., Genera-

tion of turbulent in flow conditions for large eddy simulation from stereoscopic PIV measurements, Int. J. Heat Fluid Flow 27(4) 576-584, 2006.

[19] Shaw R. H. & Schumann, U., Large Eddy Simulation of turbulent flow above and within a forest, Boundary Layer Meteorol. 61, 47-64, 1992.

[20] Stoesser T., Mathey F., Frohlich J. & Rodi W., LES of flow over multiple cubes. ERCOFTAC Bulletin 56, 2003.

[21] Xie Z.-T. & Castro I.P., LES and RANS for turbulent flow over arrays of wall-mounted cubes, Flow,Turbulence and Combustion, 76 (3), 291-312, 2006.

[22] Xie Z.-T. & Castro I.P., Effcient generation of in flow conditions for Large Eddy Simulation of street-scale flows, Flow,Turbulence and Combustion, in press, 2008, DOI: 10.1007/s10494-008-9151-5.

[23] Xie Z.-T., Coceal O. & Castro I.P., Large-eddy simulation of flows over random urban-like obstacles, Bound. Layer Meteorol., in press, 2008.

[24] Yoshizawa A., Statistical theory for compressible turbulent shear flows, with the application to subgrid scale modelling, Phys. Fluids 29, 2152-2164, 2006.

LES Based Urban Dispersal Predictions for Consequence Management

F. Grinstein, R. Bos & T. Dey

Applied Physics Division, X-3-MA, Los Alamos National Laboratory, USA.
fgrinstein@lanl.gov

Abstract

It is unlikely that we will ever have a deterministic predictive framework for the study of flows in urban scale scenarios purely based on computational fluid dynamics. This is due to the inherent difficulty in modeling and validating all relevant physical sub-processes and acquiring all the necessary and relevant boundary condition information. On the other hand, this case is representative of very fundamental ones for which whole-domain scalable laboratory (or field) studies are impossible or very difficult, but for which it is also crucial to develop predictability. In this paper, we discuss a framework for detailed dispersal predictions in urban and regional settings based on effective linkage of strong motion codes - capable of simulating detailed energetic and contaminant sources, and large-eddy simulation - capable of emulating contaminant transport due to wind and turbulence fields in built-up areas. Challenging technical aspects of the simulation approach are outlined and recent progress is reviewed in this context.

1 Introduction

Hazardous chemical, biological, or radioactive (CBR) releases in urban environments may occur (intentionally or accidentally) during urban warfare or as part of terrorist attacks on military bases or other facilities. The associated contaminant dispersion is complex and semi-chaotic. Urban predictive simulation capabilities can have direct impact in many threat-reduction areas of interest, including, urban sensor placement and threat analysis, contaminant transport (CT) effects on surrounding civilian population (dosages, evacuation, shelter-in-place), education and training of rescue teams & services, onsite contaminant mitigation, assessing strategies, pyroclastic flows (visibility), and predicting CT from targets or missile intercepts. Detailed simulations for the various processes involved are in principle possible, but generally not fast.

Predicting urban airflow accompanied by CT presents extremely challenging modeling requirements [1]. Because of the configurations with very complex geometries and unsteady buoyant flow physics involved, the widely varying temporal and spatial scales quickly exhaust current modeling capabilities. Crucial technical issues include both, turbulent fluid transport and boundary condition modeling, and post-processing of the simulation results for practical consequence management. Relevant fluid dynamic processes to be simulated include, detailed energetic and contaminant sources, complex building vortex shedding, flows in recirculation zones, and modeling dynamic subgrid-scale (SGS) turbulent and stochastic backscatter. The simulation model must also incorporate a consistent stratified urban boundary layer with realistic wind fluctuations, solar heating including shadows from buildings and trees, aerodynamic drag and heat losses due to the presence of trees, surface heat variations and turbulent heat transport.

Because of the short time spans and large air volumes involved, modeling a pollutant as well mixed globally is typically not appropriate. It is important to capture the effects of unsteady, buoyant flow on the evolving pollutant concentration distributions. In typical urban scenarios, both particulate and gaseous contaminants behave similarly insofar as transport and dispersion are concerned, so that the contaminant spread can usually be simulated effectively based on appropriate pollutant tracers with suitable sources and sinks. In some cases, the full details of multi-group particle distributions are required. In such cases, additional physics to be modeled includes particulate fall-out, as well as deposition, re-suspension and evaporation of contaminants.

Other crucial issues in the urban CT simulation process include, modeling building damage effects due to eventual blasts, addressing appropriate regional and atmospheric data reduction, and, feeding practical output of the complex combined simulation process into 'urbanized' fast-response models - capable of translating flow and atmospheric variability into local (neighborhood) CT variability. Despite the inherent physical uncertainties and model trade-offs some degree of reliable prediction of CT within urban areas appears to be possible (e.g.[2]).

The industrial-standard for plume prediction technology presently in use is based on idealized sources, rough urban canopy models, and gaussian similarity solutions ('puffs') - originally intended to model effects of large scale flow dynamics over flat terrain. Diffusion is used in such models to emulate the effects of turbulent dispersion caused by complex building geometry and by wind gusts of comparable and larger size. Plume/puff models provide fast but unrealistic predictions for typical urban scenarios (e.g.[3]) where they cannot capture dispersal driven by inherently unsteady vortex dynamics. A practical example is given in Figure 1, showing simulated CT in Times Square, New York City (from [4]). The figure depicts the so-called fountain effect occurring behind tall buildings. The fountain effect is the systematic migration of contaminant from ground level up the downwind side of buildings followed by continuous ejection into the air flowing over their tops. It has been observed in field experiments [5] and reported in wind tunnel studies [6], and is believed to be driven by arch vortices [7] lying behind the buildings (Figure 2).

2 Urban Flow Simulation

The advantages of the computational fluid dynamics (CFD) representation to simulate CT transport and dispersion, include the ability to quantify complex geometry effects, to predict dynamic nonlinear processes faithfully, and to treat turbulent problems reliably in regimes where experiments, and therefore model validations, are impossible or impractical. Solving for urban flow and dispersion is a problem for time-dependent, aerodynamic CFD methods. Computing urban aerodynamics accurately is a time-intensive, high-performance computing problem. Using this technology for the emergency assessment of blasts, industrial spills, transportation accidents, or terrorist CBR attacks requires very-tight time constraints that suggest simple approximations, which unfortunately produce inaccurate results.

Unavoidable trade-offs demand choosing between fast (but inaccurate) and much slower (but accurate) models. Relevant time domains can be identified which require appropriate corresponding time-accurate ('full physics') simulation codes, involving physical processes that occur in microseconds-to-milliseconds, and seconds-to-one-hour ranges. Target codes (strong-motion and LES, respectively, discussed below) for these domains are integrated with appropriate mesoscale / atmospheric reduced data. Linking codes between the various time domains allows the results of one to be used as the initial conditions for the next. The suite of full-physics simulations is used to develop source term, buoyant rise, and flow field parameterizations in urban environments for later use with fast-response high-fidelity analytical model tools (e.g.[5,8]).

2.1 Energetic and Contaminant Source Modeling

Early-time phenomenology during explosive release of contaminants includes shock wave propagation and material flow at peak pressures that may be 10^5 or more times ambient atmospheric pressures. The upward material velocities in the resulting fireball may be supersonic and deformations large. Fireballs even for large chemical explosions may not equilibrate with the surrounding atmosphere until reaching the tropopause far above any urban skyline. Building and ground materials can be fragmented and entrained in the flow being released as suspended atmospheric particles. The CASH strong motion code [9] includes appropriate methods for accurately modeling explosions, including state-of-the-art models for high explosive performance, and for the deformation and failure of other materials. It can model shock wave propagation in the atmosphere and the ground. CASH utilizes a lagrangian hydrodynamic solution method as its base solver, and also contains an arbitrary Lagrangian-Eulerian solver. While it can model many aspects of solid deformation and failure, the detailed generation of rubble and dust during fragmentation of building materials due to blasts remains poorly understood. Consequently, we are also investigating the use of codes based on particle and discrete element methods to understand and capture the phenomenology of this latter process. Principal among these is CartaBlanca [10], which uses the material point method and provides promising results on a number of related problems. Regardless of which code is being employed, a calculation is run until shock strength and deformation effects are small enough to map to the dispersal code for the remainder of the simulation.

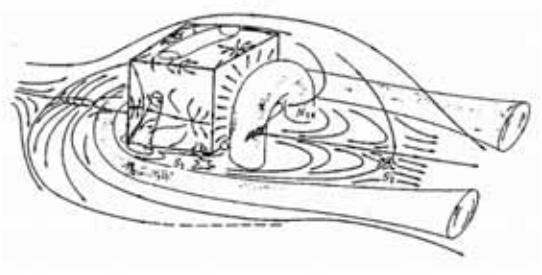

Figure 2: *Arch vortices governing the flow dynamics past a surface mounted cube [7].*

2.2 The LES Approach for Urban Contaminant Transport

Direct numerical simulation (DNS) - resolving all relevant space/time scales - is prohibitively expensive for most practical flows at moderate-to-high Reynolds number, and especially so for urban CT studies. On the other end of the CFD spectrum are the standard industrial methods such as the Reynolds-Averaged Navier-Stokes (RANS) approach which simulate the mean flow and approximately model the effects of turbulent scales. These are generally unacceptable for urban CT modeling because they are unable to capture unsteady vortex-driven plume dynamics. LES [11] constitutes an effective intermediate approach between DNS and the RANS methods. LES is capable of simulating the key unsteady flow features that cannot be handled with RANS (or gaussian plume methods) and provides higher accuracy than RANS. In LES, the large energy containing structures are resolved whereas the smaller, presumably more

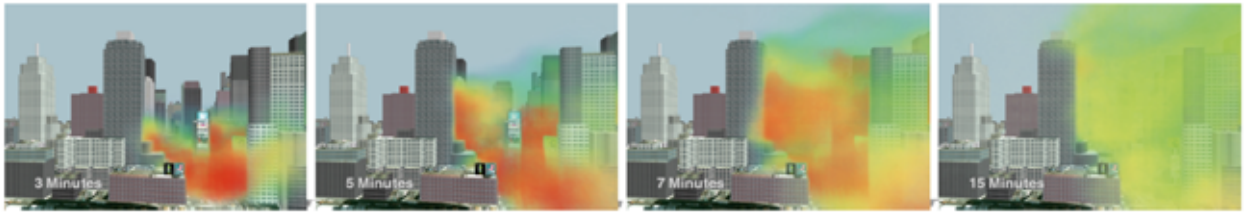

Figure 1: *CT from an instantaneous release in Times Square, New York City as predicted by the FAST3D-CT MILES model (from [4]). Concentrations shown at 3, 5, 7 and 15 minutes after release. The figure demonstrates the typical complex unsteady vertical mixing patterns caused by building vortex and recirculation patterns, and predicts endangered regions associated with the particular release scenario. Vortex dynamics driven CT can not be captured by plume/pluff modeling.*

isotropic, structures are filtered out and unresolved SGS effects are modeled.

Adding to the physics based difficulties in developing and validating SGS models for LES, are truncation terms due to discretization that are comparable with SGS models in typical LES strategies [12]. LES resolution requirements can thus become prohibitively expensive for practical flows and regimes. Implicit LES (ILES, MILES) [13] effectively address the seemingly insurmountable issues posed to LES by under-resolution, by relying on the use of SGS modeling and filtering provided implicitly by physics capturing numerics. Popular high-resolution finite-volume numerics such as flux-corrected transport (FCT), piecewise-parabolic method, and hybrid algorithms are typically used for ILES. ILES theoretical analysis focuses on the modified flow equations satisfied by the numerically calculated solutions, which provide the framework to reverse engineer physically desirable features into the numerics design. Recent Taylor-Green Vortex studies using ILES, LES, and DNS [14] demonstrate robust capabilities of ILES in simulating transition to turbulence and turbulence decay (e.g. Figure 3). Extensive ILES verification and validation studies of turbulent flows in areas of engineering, geophysics, and astrophysics has been reported [13].

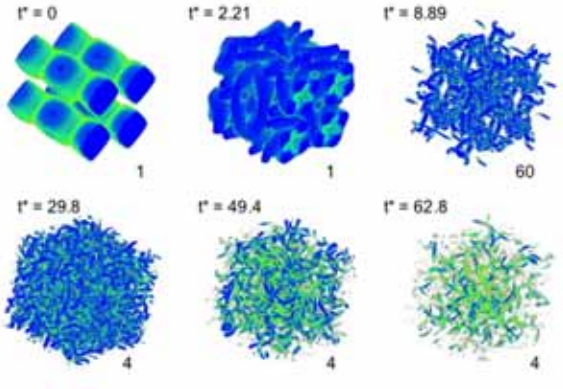

Figure 3: *Flow visualizations ranging from the initial Taylor-Green vortex configuration at $t^* = 0$, to transition ($t^* \sim 9$) to increasingly organized smaller-scale vortices (top row), and then to fully developed (disorganized) worm-vortex flow characteristic of turbulence ($t^* > 30$), from [15].*

The ILES urban CT model discussed here is the FAST3D-CT code. It involves a scalable, low dissipation, 4th order phase-accurate FCT convection algorithm [2], implementing direction-split convection, 2nd-order predictor-corrector temporal integration, and time-step splitting techniques. The relevant system of equations for the problem under consideration involves the time-dependent buoyant flow equations for mass and momentum conservation,

$$\begin{cases} \partial_t(\rho) + div(\mathbf{v}\rho) = 0 \\ \partial_t(\rho\mathbf{v}) + div(\rho\mathbf{v}\otimes\mathbf{v}) = div(\mathbf{S}) - grad(P) + f \\ \quad \mathbf{f}_x = \mathbf{f}_y = 0; \mathbf{f}_z = \rho g(1 - T/T_o) \\ \partial_t(\Theta) + \mathbf{v}\cdot grad(\Theta) = \alpha_h \nabla^2\Theta \\ \partial_t(\eta_i) + \mathbf{v}\cdot grad(\eta_i) = 0,\ i = 1,\dots \end{cases}$$

where ρ is the mass density, $\mathbf{v}$ is the velocity field, $\mathbf{S}$ is the viscous stress, g is the acceleration due to gravity, T and Θ denote fluid and potential temperatures, respectively, α_h denotes molecular heat diffusivity coefficient, and the η_i are pollutant concentration tracers modeling different contaminants and/or release scenarios. The flow equations must be supplemented with an equation of state, appropriate inflow, outflow, and wall boundary-condition models. The unsteady equations can be closed with an ideal-gas equation of state and the relationship between fluid and potential temperatures (e.g.[15]). The potential temperature has the convenient property of being conserved during vertical movements of a gas parcel, provided heat is not added or removed during such excursions; in this way, the said parcel can be identified or labeled by its potential temperature. The model uses rough-wall-boundary condition models for the surface stress and the heat transfer from the walls, and convective conditions at outflow boundaries. Other required physical models include the ability to emulate multi-phase flows, particulate transport dynamics, seasonally-adjusted drag and heat transfer effects due to trees, solar heating effects, and stochastic turbulent backscatter (e.g.[2]).

2.3 Progress Linking Strong Motion and Dispersal Codes

In the type of simulations represented by the dispersal of contaminants due to an energetic release of energy in an urban environment, no one code can adequately simulate the full range of physics involved, nor should a user want that to be the case. Codes such as CASH and FAST3D-CT have been specifically developed to simulate very precise ranges of the relevant physics. CASH has the ability to simulate the strong motion regime where shocks are present due to an energetic source (such as a high explosive) but is not able to do the dispersal of contaminants in the atmosphere over a the size of a typical urban setting. On the other hand FAST3D-CT is not able to handle shocks or solid material descriptions. The solution we have proposed is to use results of a strong motion code (e.g., CASH) as detailed initial-condition energetic and contaminant sources to the dispersal code (e.g. FAST3D-CT) at a time when shocks are no longer present or reduced to neglible levels. The calculations then proceed as in a regular dispersal simulation. We have been able to establish such a link using an early version of FAST3D-CT [16] to simulate flow over a flat terrain (e.g. Figure 4). Using a FAST3D-CT restart file with an ambient logarithmic atmospheric boundary layer (ABL) profile, we overwrite a cylindrical sub-volume with the results from a 2D axially-symmetric simulation of the detonation of a 1-ton high explosive source at 2m above ground level at a time when the physics of the CASH simulation is at levels appropriate for FAST3D-CT to use ($t_o = 3.5$sec).

2.4 Urban Geometry Specification

An efficient and readily accessible data stream is used to specify the building geometry database. High-resolution (1m or smaller) vector geometry data is typically available for many major cities. From this data, building heights are determined on a regular mesh of horizontal locations with relatively high resolution (e.g. 1m). Similar tables for terrain, vegetation, and other land use variables can be extracted. These tables are interrogated during the mesh generation to determine which cells in the computational domain are filled with building, vegetation, or terrain. This process is a very efficient way to convert a simple geometric representation of an urban area to a computational grid. A grid-masking approach is used to indicate which computational cells are excluded from the calculation as well as to determine where suitable wall boundary conditions are to be applied.

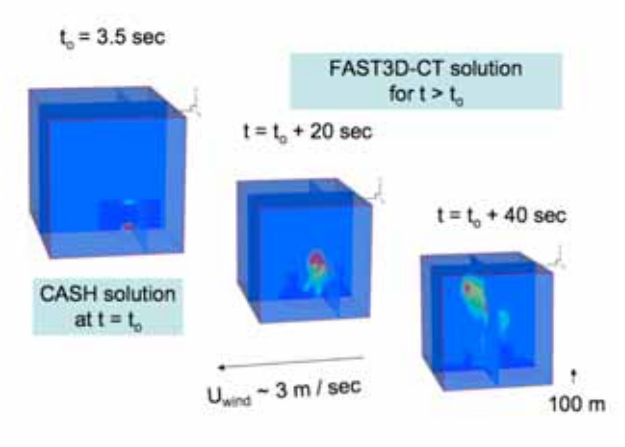

Figure 4: *Linked simulations from strong-motion and dispersal codes are visualized in terms of temperature distributions; color mapping is linear between* 293^oK *(blue)* -550^oK *(red).*

2.5 Atmospheric Boundary Layer Specification

The ABL characterization upwind of the finite urban computational domain directly affects the boundary-condition prescription required in the simulations. Numerical sensitivity studies show that wind fluctuation specifics are major factors in determining urban CT. The important length scales (tens of meters to kilometers) and time scales (seconds to minutes) in wind gusts can be resolved easily by CFD models that accurately resolve the buildings. However, single-point statistical flow data from laboratory experiments and field trials is typically inadequate and/or insufficient to fully characterize the ABL conditions used in the urban flow simulation model. Calibration of deterministic models for evolving realizations of upstream flow fluctuations in the ABL have recently used data from urban model wind-tunnel experiments [4].

2.6 Predictability

Establishing the credibility of the solutions is one of the stumbling blocks of urban CFD simulations. The goal of validating a numerical model is to build a basis of confidence in its use and to establish likely bounds on the error that a user may expect in situations where the correct answers are not known. A primary difficulty is the effective calibration and validation of the various physical models since much of the input needed from experimental measurements of these processes is typically insufficient or even nonexistent. Further, even though the individual models can all be validated separately, the larger problem of validating the overall simulation code has to be tackled as well. Validation studies with experiments require well-characterized datasets with information content suitable to initiate and evaluate unsteady simulation models as well as the cruder steady-state models. In principle, such high-quality datasets can be made available using urban models in the context of carefully controlled and diagnosed wind-tunnel experiments. Finally, a crucial convergence issue needs to be addressed here: the fact that grid independence can only be truly pursued in the context of DNS. Solutions associated with different resolutions correspond to selecting correspondingly different values of some characteristic effective Reynolds number (e.g. [14]). Some sort of convergence on large-scale measures is expected in the high-Re limit, but faster coherence breakdown with increasing resolution (effective Re) unavoidably occurs as finer dynamical features are allowed to contribute and affect the larger scales. This difficulty is actually inherent to any LES approach (and to ILES in particular), given that the smallest characteristic resolved scale is determined by a resolution cutoff wavelength prescribed by a spatial-filtering process - irrespective of whether the characteristic filter-length is or not itself resolved by grid resolution. Moreover, SGS modeling issues typically cannot be meaningfully addressed independently of other crucial aspects controlling simulation performance, i.e. boundary condition and other modeling used for the various physical sub-processes. The observational simulation process - as determined by all models involved - is unavoidably intrusive, and appropriate verification and validation metrics have to be identified.

Acknowledgements

Los Alamos National Laboratory is operated by the Los Alamos National Security, LLC for the U.S. Department of Energy NNSA under Contract No. DE-AC52-06NA25396.

References

[1] Britter, R.E., and Hanna, S.R., Flow and Dispersion in Urban Areas, Ann. Rev. Fluid Mech., Vol. 35, pp. 469-496, 2003.

[2] Patnaik, G., Grinstein, F.F, Boris, J.P., Young, T.R., Parmhed, O., Large Scale Urban Simulations, Chapter 17 in, Implicit Large Eddy Simulation: Computing Turbulent Fluid Dynamics, Grinstein, Margolin, and Rider, Eds. Cambridge University Press, 2007.

[3] Pullen, J., Boris, J.P., Young, T.R., Patnaik, G., and Iselin, J.P., A Comparison of Contaminant Plume Statistics from a Gaussian Puff and Urban CFD Model for Two Large Cities, Atmos. Environment, Vol. 39, pp. 1049-1068, 2005.

[4] Patnaik, G., Boris, J.P., Young, T.R., Grinstein, F.F., Large Scale Urban Contaminant Transport Simulations with MILES, J. Fluids Engineering, Vol. 129, pp. 1524-1532, 2007.

[5] Rappolt, T.J., Measurements of Atmospheric Dispersion in the Los Angeles Urban Environment Summer 2001, Project Report 1322, Tracer ES&T, San Marcos, CA, 2002.

[6] Brown, M., Urban Dispersion - Challenges for Fast Response Modeling, in Fifth AMS Symposium on the Urban Environment, LA-UR-04-5129, LANL, Los Alamos, NM, 2004.

[7] Hussein, H.J., and Martinuzzi, R.J., Energy Balance for Turbulent Flow Around a Surface mounted Cube Placed in a Channel, Phys. Fluids, Vol. 8, pp. 764-780, 1996.

[8] Boris, J.P., The Threat of Chemical and Biological Terrorism: Preparing a Response, Comp. Science and Engineering, Vol. 4, pp. 22-32, 2002.

[9] Dey, T.N., Bos, R.J., CASH, Version 01(CASH) Code, Los Alamos National Laboratory computer code LA-CC-01-053, 2001.

[10] http://www.lanl.gov/projects/CartaBlanca/.

[11] Sagaut, P., Large Eddy Simulation for Incompressible Flows, 3rd Ed., Springer, 2005.

[12] Ghosal, S., An analysis of numerical errors in large-eddy simulations of turbulence, J. Comp Phys., Vol. 125, pp. 187-206, 1996.

[13] Grinstein, F.F., Margolin, L.G., and Rider, W.J., Eds. Implicit Large Eddy Simulation: Computing Turbulent Fluid Dynamics, Cambridge University Press, 2007.

[14] D. Drikakis, C. Fureby, F.F. Grinstein, and D. Youngs, Simulation of Transition and Turbulence Decay in the Taylor-Green Vortex, Journal of Turbulence, Vol. 8, 020, 2007.

[15] S. Pal Arya, Introduction to Micrometeorology, Academic Press, 2001, p. 65.

[16] Grinstein, F.F., Boris, J.P., Numerical Simulation Of Unsteady Buoyant Flows In Buildings, ASME Paper FEDSM2001-18059, 2001.

Atmospheric Turbulent Reacting Flows Influenced by Shallow Cumulus: A Large-Eddy Simulation Study

Jordi Vilà-Guerau de Arellano & Kees van den Dries

Meteorology and Air Quality Section, Wageningen University, The Netherlands.
jordi.vila@wur.nl

1 Introduction

Studying turbulent reacting flows in the atmospheric boundary layer (ABL), namely the lowest region of the troposphere influenced by the Earth's surface, is challenging due to the strong interactions of dynamics, radiation, phase changes and chemical transformations. In particular, the role of ABL clouds in atmospheric dispersion and chemistry is still not well understood. The presence of shallow cumulus in the atmospheric boundary layer modifies the transport, turbulent mixing and reactivity of chemical species. Vertical transport is enhanced in the cloud layer by the buoyant convection associated to latent heat release in the condensation process at cloud formation. As a result, reactants emitted at the surface reach higher altitudes (up to 3 to 4 km depending on surface forcing and free troposphere conditions) compared to the vertical distribution on clear boundary layer (limited by the ABL growth). While in the sub-cloud layer, reactants are well mixed, in the cloud layer the variability quantified by the reactant co-variances indicates the difference in the turbulent characteristics between clouds (highly turbulent) and their environment (minimum levels of turbulence). Finally, scattering of radiation by cloud droplets perturb the photolysis rates enhancing the values at cloud top and decreasing them below cloud compare to the clear sky situation.

In this research, we present numerical experiments carried out using the Dutch Atmospheric Large-Eddy Simulation (DALES) [4] to investigate the interaction of these processes on the daily ozone production. By including a semi complex chemical mechanism for the $O_3 - HO_x - NO_x - CO$ system, we are able to reproduce the vertical and diurnal variation of ozone and related species. Emphasis is placed on studying: (a) the effect of the dilution and enhanced vertical transport by shallow cumulus convection, (b) the evolution of the reactants in the sub-cloud layer and in the cloud layer and their net transport and (c) the study of potential departures of chemical equilibrium due to the presence of clouds. This research extends the previous simulation of the influence of shallow cumuli over land on a the simple chemical mechanism composed by the triad $NO - O_3 - NO_2$ [10].

2 Dynamics

The study is based on the meteorological situation described by [1]. A cloudy boundary layer characterized by the presence of clouds was observed on 21 June 1997 at the Southern Great Plains site of the Atmosphere Radiation Measurement (ARM). Based on the surface and the upper air observations, [1] proposed an idealized experiment to study the dynamics of shallow cumulus over land. Our simulation is based on exactly the same domain size and discretization and the same surface forcing. The diurnal variation of the surface turbulent fluxes yields the formation of unsteady shallow cumulus.

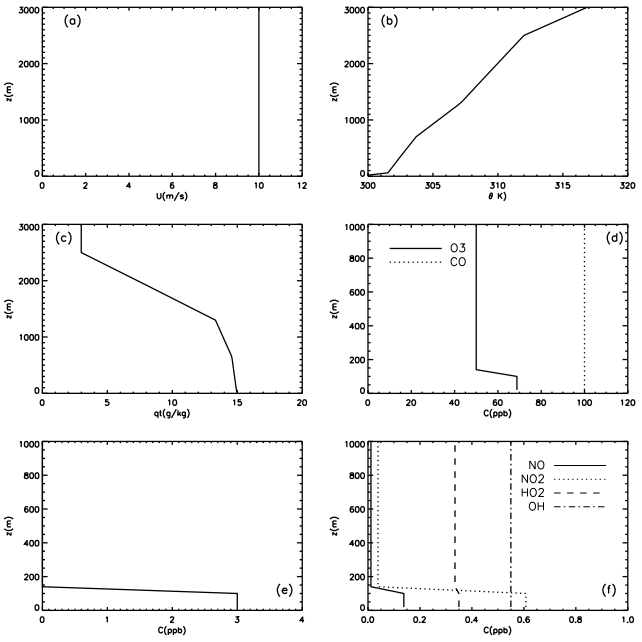

Figure 1: *Initial vertical profiles of (a) wind speed (U-component), (b) liquid water potential temperature, (c) specific humidity, (d) O_3 and CO mixing ratios, (e) RH and (f) NO, NO_2, 10*HO_2 and 1000*OH mixing ratios.*

The initial vertical profiles for the wind component U, potential temperature and specific humidity are shown at figure 1a 1b and 1c. The liquid water potential temperature and specific moisture profiles are the same as the one prescribed by [1] with the only difference to have a less stable profile (γ_θ=1.7 K/km) between 1300 and 2500 m (see figure 10a at [1]). By doing so, we are able to enhance the vertical growth rate of the cloud layer. Moreover, the only external forcing prescribe is a westerly wind equal to 10 ms^{-1}. Note that this forcing id dependent on the horizontal pressure differences. The small external tendencies representing the advection of heat and moisture are not included.

3 Chemistry

3.1 Mechanism

The semi-complex chemistry which reproduces the diurnal variability of ozone is based on [7]. The chemical mechanism includes the following reactions:

Num	Reaction	k_{298} $(ppbv^{-1}s^{-1})$
R1	$O_3 \overset{H_2O}{\rightarrow} 2OH + O_2$	$5.00\ 10^{-6}$
R2	$NO_2 \overset{O_2}{\rightarrow} NO + O_3$	$7.50\ 10^{-3}$
R3	$NO + O_3 \rightarrow NO_2 + O_2$	$4.75\ 10^{-4}$
R4	$OH + CO \overset{O_2}{\rightarrow} HO_2 + CO_2$	$6.00\ 10^{-3}$
R5	$OH + RH \rightarrow HO_2 + Prd$	$fx6.00\ 10^{-3}$
R6	$HO_2 + NO \rightarrow OH + NO_2$	$2.10\ 10^{-1}$
R7	$HO_2 + O_3 \rightarrow OH + 2O_2$	$5.00\ 10^{-5}$
R8	$2HO_2 \rightarrow H_2O_2 + O_2$	$1.67\ 10^{-1}$
R9	$OH + NO_2 \rightarrow HNO_3$	$2.75\ 10^{-1}$
R10	$OH + O_3 \rightarrow HO_2 + O_2$	$1.67\ 10^{-3}$
R11	$OH + HO_2 \rightarrow H_2O + O_2$	2.75

By using this chemical scheme, we aim at reproducing the essential reactions in the ozone diurnal variability under semi-urban or rural emission conditions without increasing the computer burden. In short, the chemical mechanism reproduce how the non-linear chemistry driven by the emissions of a generic hydrocarbon (RH) and nitric oxide (NO) yiels to an increase of the daily ozone values under the presence of transformations driven by ultraviolet radiation (reaction R1 and R2).The units of the photolysis frequencies are in s^{-1}. For this control run we have assumed that the photolysis rates j_1 and j_2 are constant on time with values equal to $2.7\ 10^{-6}\ s^{-1}$ and $8.9\ 10^{-3}\ s^{-1}$ (maximum values 21^{st} at a latitude 45N). The second-order reaction rate constants are in $ppb^{-1}s^{-1}$. The factor f of reaction R5 is variable and it ranges from 100 to 300. In the case understudy, we have taken the value equal to 300 since we are interested to have a time scale for the chemical reaction rate R5 similar to the turbulent time scale. Note that the typical turbulent time scales in cloudy boundary layers range from 10 minutes to 30 minutes. For instance, typical values of the OH mixing ratio in the ABL are equal to 0.5 ppt, and consequently the characteristic time scale for the generic hydrocarbon is around 18.5 minutes. In the numerical experiment, we have assumed that the mixing ratio of CO is fixed at 100 ppb uniformly in the whole domain. Furthermore, we have also prescribed the following emission fluxes constant on time: NO flux (0.1 $ppbms^{-1}$) and RH flux (1.0 $ppbms^{-1}$). In the simulations, the dry deposition of species is neglected. Figures 1d, 1e and 1f also show the initial profiles of the reactant species.

3.2 Photolysis perturbation by clouds

An important aspect of this study is to investigate the modification of the photolysis rates by the presence of clouds. Because clouds alter the different proportions of direct and diffuse ultraviolet radiation, the actinic flux (and therefore the photolysis rates) has different values below, in, and above the clouds [8]. We have implemented this effect by calculating at every time step a factor below and above the clouds and by applying this factor to the clear sky value of the photolysis rate j_{clear} following [2]:

$$j_{clouds} = F\ j_{clear} \tag{1}$$

Above the cloud, the factor (F) is defined as:

$$F = 1 + \alpha\ (1 - t_r)\ cos(\chi_o). \tag{2}$$

While, below the cloud, F is defined as:

$$F = 1.6\ t_r\ cos(\chi_o). \tag{3}$$

Here, t_r is the energy transmission coefficient for normal incident light, χ_o is the solar zenith angle, and α is a reaction dependent coefficient (for nitrogen dioxide α=1.2). To simplify the calculation, a linear interpolation is assumed inside the cloud scaled with the value of the liquid water content (q_l). Based on measurements of j_2 [5], the linear interpolation assumption likely overestimates the photolysis rate in the middle to lower regions of the cloud while underestimates the photolysis rate near cloud top.

The energy transmission coefficient t_r depends on the cloud optical depth and a scattering phase function asymmetry factor (γ) equal to 0.86 for the typical cloud particle size ranges under study [6]. The expression reads:

$$t_r = \frac{5\ -\ e^{-\tau}}{[4\ +\ 3\tau(1-\gamma)]}. \tag{4}$$

The cloud optical depth (τ) is calculated according to the expression given by [9]

$$\tau = \frac{3}{2}\frac{W}{\rho_l}\ r_e^{-1}, \tag{5}$$

where W is the vertically integrated liquid water ($kg\ m^{-2}$), ρ_l is the water density ($kg\ m^{-3}$) and r_e is the effective radius. Here, we have used a constant value of $r_e = 10\ \mu m$. For clouds characterized by values of $\tau < 5$ and for regions between clouds, we have assumed the photolysis rate of clear sky conditions. Regions between clouds may actually have enhanced photolysis rates due to cloud scattering. Here, we are simply investigating the importance of cloud scattering in the vertical cloud column as a first step in our research. Our control simulation includes the modification of photolysis rates due to cloud scattering.

3.3 Dependence of the reaction rate to water vapour

Notice that reaction R1 does not take into account possible spatial and temporal variations of specific moisture in the cloudy boundary layer. A possible solution to account for this variation is allowing water vapour to be "active" in the chemical system. In short, reaction R1 represents the following three reactions:

$$R12\ \ O_3\ + h\nu \rightarrow O_2 + O(^1D) \quad j_3\ varies$$

$$R13\ \ O(^1D)\ +\ M \rightarrow O(^3P) + M \quad k_{10} = 7.13\ 10^{-1}$$

$$R14\ \ O(^1D)\ +\ H_2O \rightarrow 2OH \quad k_{11} = 5.41,$$

where M is a molecule of air. In our study, the value of the specific humidity in the sub-cloud layer is around 15 g/Kg (approximately a relative humidity at the surface of RH=50% (T=305 K) at 12 LT) and at the top of the sub-cloud layer around 81%. Future numerical experiments will address the sensitivity of the results to the spatial distribution of water vapour in cloudy boundary layers by including explicitly reactions (R12)-(R14) instead of reaction (R1).

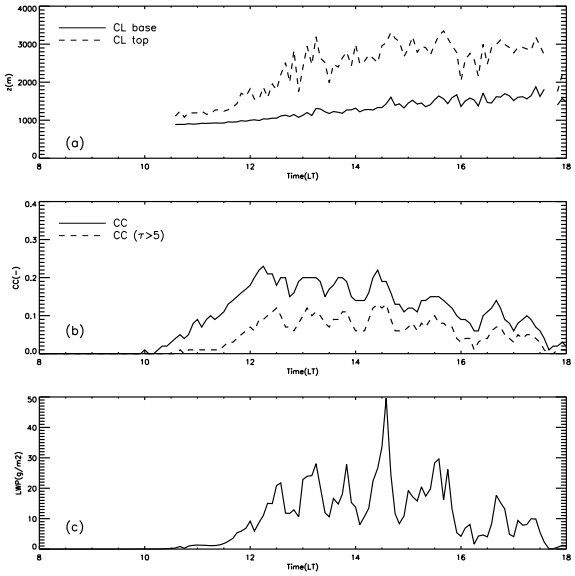

Figure 2: *Time evolution of (a) cloud base and cloud top, (b) cloud cover for the whole cloud population and the dense clouds defined with a cloud optical depth larger than 5 and (c) integrated liquid water path.*

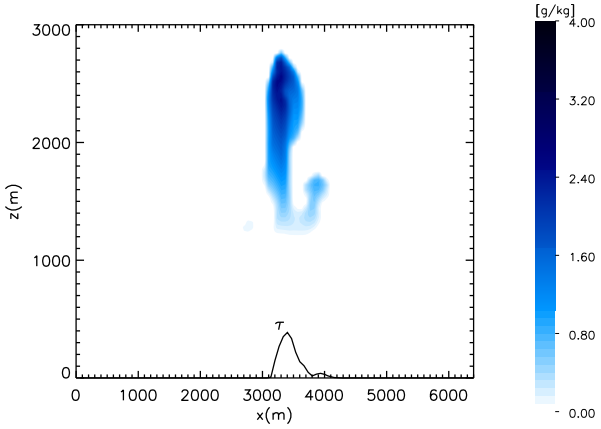

Figure 3: *Instantaneous cross section of the liquid water content at 15.45 LT. The cloud optical depth calculated according expression 5 is also included.*

4 Results

4.1 Cloud evolution and vertical structure

The main dynamic characteristics of the evolution of shallow cumulus are shown at figure 2. The results agree very well with the previous simulations summarized by [1] and [10]. In short, shallow cumulus are formed around 10 LT with a cloud base increasing linearly on time from 800 m to 1200 m. Cloud depth fluctuates over time with maximum values around 2000 m between 13 and 16 LT. Notice that from a thermodynamic perspective the cloud top height defines the boundary layer top. The values of cloud cover (figure 2b) and liquid water path (figure 2c) are characteristic of shallow cumuli over land. In the figure of cloud cover (figure 2b), we have also included the cloud cover of clouds characterized by a $\tau > 5$ since these thick clouds are the ones which perturb the photolysis rate. As the figure shows, less tha 10% of shallow cumulus exrt an influence on the photolysis rates of reactions R1 and R2.

In order to illustrate the shallow cumulus simulated by DALES, we show in figure 3 an instantaneous vertical cross section of the liquid water content and the corresponding instantaneous cloud optical depth (expression (5)). The characteristic horizontal and vertical length scales are around 500 m and between 1000-2000 m. However, during the simulation not all the clouds fully developed vertically and therefore they can be characterized as forced clouds (see the difference in the cloud covers in figure 2b). Notices that DALES is able to represent the spatial distribution of the liquid water content (q_l) with a high degree of detail which is fundamental to determine the perturbation of the photolysis rate due to the presence of clouds. As a result, we obtain very large values for τ which can have a large impact on the photolysis ratei (see discussion at figure 6).

Figure 4 shows the evolution of the vertical profiles of the thermodynamic variables spatially averaged over the whole domain. The time averaged is 1 hour. In the sub-cloud layer, all the variables are well mixed. In figure 4b, the liquid water potential temperature profile after 12 LT is conditionally unstable from 1000 m up to the limit of convection located approximately at around 2700 m. Above this level, there is an absolutely stable boundary layer. In figure 4d, the liquid water content profile shows the transition from a clear maximum near cloud base in the early stages of cloud development to a more homogeneous distribution with height once the clouds are fully vertically developed.

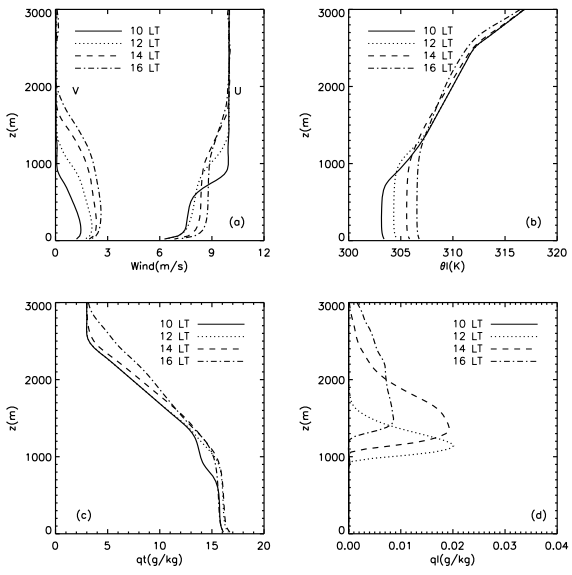

Figure 4: *Vertical profiles of (a) wind speed (U- and V-component), (b) liquid water potential temperature, (c) specific humidity and (d) liquid water (one-hour averaged).*

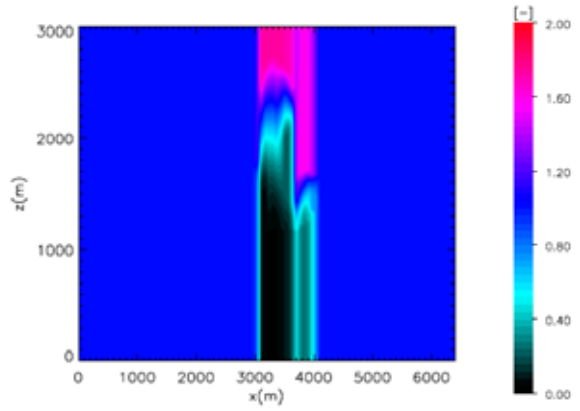

Figure 5: *Instantaneous cross section of the j_{cloud}/j_{clear} ratio for the photolysis rate of reactions (1) and (2) at 15.45 LT.*

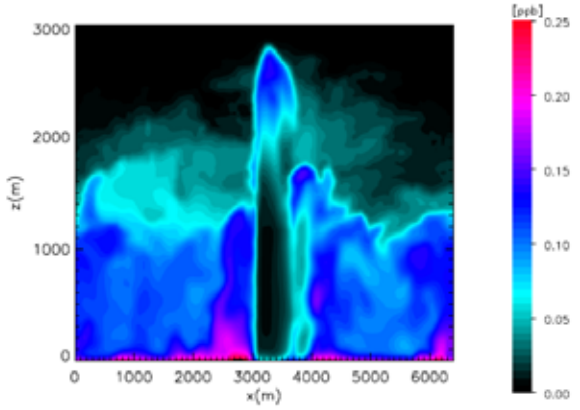

Figure 6: *Instantaneous cross section of the nitric oxide (NO) mixing ratio at 15.45 LT.*

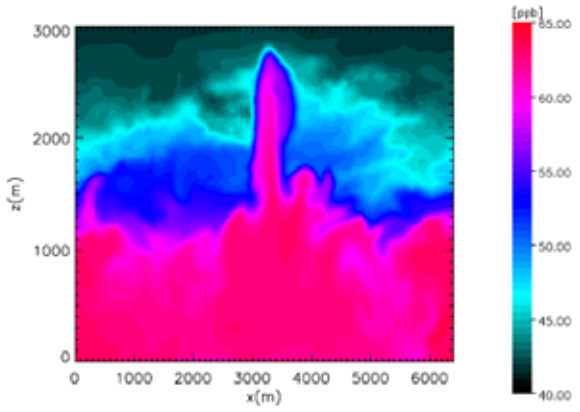

Figure 7: *Instantaneous cross section of the ozone (O_3) mixing ratio at 15.45 LT.*

4.2 Spatial patterns of radiation and reactant fields

The modification of the photolysis rate by the parameterization (1) is shown in the instantaneous cross section of the ratio j_{cloud}/j_{clear} (Figure 5). As expressed by the factors (2) and (3), there is an enhancement above the cloud, a linear decrease in the cloud and a decrease in the photolysis values below cloud compared to the cloudless study. Notice that the parameterization gives perhaps very low photolysis values because of the large *local and instanatneous* values of the cloud optical depth, *i.e.* $\tau > 300$. In consequence, below thick cloud, photolysis rate can be closer to zero, *i.e.* absence of chemical reactions R1 and R2. A possible future improvement is a better characterization of the effective radius (see expression (5)) for shallow cumuli over land. This characterization will require the validation, in future work, of these values with in-situ observations. Furthermore, the parameterization is only 1-dimensional and consequently neglects the possible contributions of the reflection at the lateral side by neighbouring clouds. In spite of these shortcomings, the main goal of the study is to have a reliable numerical tool which allow us to study simultaneously the role of dynamics, mixing, radiation and chemical transformations in turbulent reacting flows driven by the presence of clouds.

Figures 6 and 7 show the spatial distribution of the NO and O_3 mixing ratio. The intrusion of the polluted air masses into the free troposphere (almost 3000 meters) due to the extension of the atmospheric boundary layer until cloud top is well reproduced by DALES. Notice that the cloud top defines now the boundary layer height. The less abundant species (NO) is largely influenced by the photolysis perturbation. In consequence, very small values of the nitric oxide mixing ratio are found below the cloud due to the large decrease of the photolysis rate at reaction 2. In turn, a NO maximum is found near cloud top related to the increase of the UV-actinic flux due to the combined contributions of direct and diffuse ultraviolet radiation at this region and the largest mixing ratio of NO_2 available originated and ventilated from the sub-cloud layer. Once again, it will be important to contrast these numerical results with aircraft observations taken in polluted areas influenced by shallow cumuli. In figure 7, one can distinguish the large difference in ozone values within the cloud ($\approx$ 65 ppb) and around the cloud ($\approx$ 50 ppb). Furthermore, as shown by the figure, the environment around the cloud is characterized by a rather stratified layering indicating low activity of turbulence and therefore of mixing.

4.3 Vertical characteristic of the mean and flux profiles of the reactants

The results corresponding to the evolution and distribution of the chemical reactants are shown at figures 8-9. Similar to the thermodynamic vertical profiles, we found well-mixed values within the sub-cloud layer. The enhancement of the vertical transport within the cloud layer is noticeable for the inert compounds and the NO, NO_2 and HNO_3 reactants (see the profiles above 1000 m) whereas the generic hydrocarbon RH is depleted within the sub-cloud layer. In that respect, it is worth to mention the dependence of the $RH-$profile on the factor f which controls the reaction speed of reaction 5. Notice that these profiles are averaged vertical profiles over the whole domain including cloud and cloudless environment regions. As such, and in spite of the relative small cloud cover shown in figure 2b (less than 0.2), the vertical profiles show the active role of clouds in diluting and transporting reactants from the sub-cloud layer to the cloud top. However, the cloud ventilation occurs within the boundary layer since cloud top is now defining the boundary layer height [3]. At figure 9c, the OH profile is almost constant on height, with a characteristic minimum near the RH surface emissions (reaction 5) and the maximum value located at cloud base. End product

species, HNO_3 and H_2O_2 (figure 9d) show a clear difference in their vertical pattern. HNO_3 is mainly produced at the sub-cloud layer due to the abundance of NO_2 (see reaction R9) and transported upwards by the cloud whereas H_2O_2 is locally produced through out the atmospheric boundary layer.

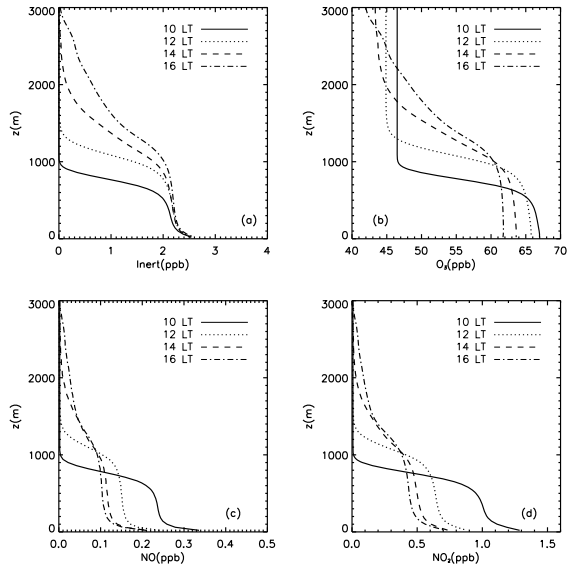

Figure 8: *Vertical profiles of the (a) inert, (b) ozone, (c) NO and (d) NO_2 (one-hour averaged).*

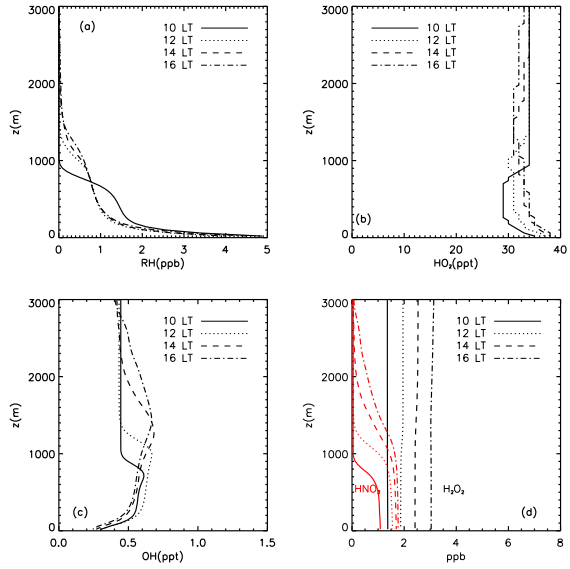

Figure 9: *Vertical profiles of the (a) generic hydrocarbon RH, (b) HO_2, (c) OH and (d) H_2O_2 and HNO_3 (one-hour averaged).*

Figures 10 and 11 show the vertical flux profiles for the inert and reactive species. Focusing first on the inert species, one can observed that the flux profile is almost constant on height in the sub-cloud layer similar to the vertical fluxes observed in dry convective boundary layers. Within the cloud layer, the flux decrease with height through out the cloud depth. This flux is entirely driven by the buoyancy flux due to the latent heat release.

Reactant emitted at the surface (NO and RH) are clearly modified due to chemical reactions departing from the linear profiles characteristic of inert species and with the following values of the flux divergence: for NO and RH the values are 0.05 ppb/hour and 3.6 ppb/hour, respectively. The latter value shows that the flux divergence largely contributes to the budget of RH and therefore it has to be taken into account.

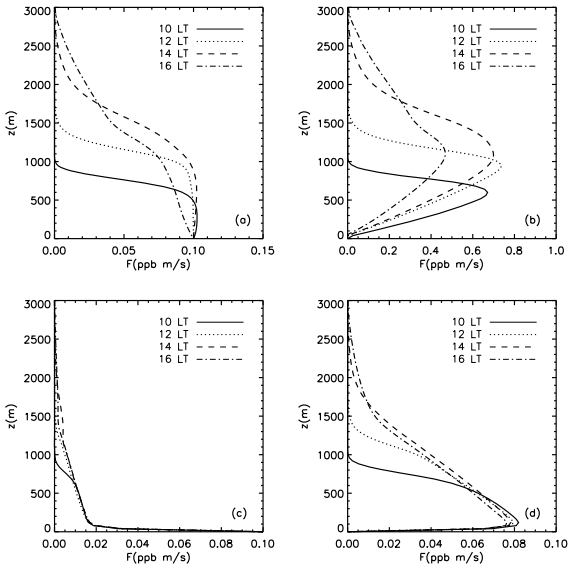

Figure 10: *Vertical flux profiles of the (a) inert, (b) ozone, (c) NO and (d) NO_2 (one-hour averaged).*

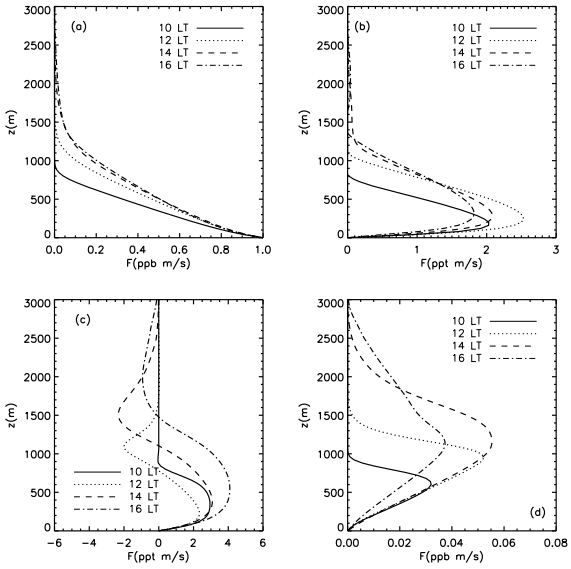

Figure 11: *Vertical flux profiles of the (a) generic hydrocarbon RH, (b) HO_2, (c) OH and (d) HNO_3 (one-hour averaged).*

In absence of deposition fluxes, the maximum flux for ozone (figure 10b) and nitric acid (figure 11d) is situated near the cloud base height where species are introduced in the cloud layer indicating the relevance of estimating and representing adequately this region in large atmospheric scale models. A previous study [10] have shown that the parameterization of shallow cumulus convection using the mass flux represents satisfactorily the transport flux within the cloud, but it tends to underestimate the flux value at cloud base.

Notice the importance of the flux divergence in all the reactant profiles. Compared to the flux profile of the inert species, all the fluxes vary with height in the sub-cloud layer. For reactants like O_3 and HNO_3 the

flux divergence changes sign between the sub-cloud layer and the cloud layer which could lead to large errors in inferring of flux profiles from observations taken from airborne platforms.

In addition to the vertical profiles, DALES results enable us quantify the volume (bulk) mixing ratio of the inert and reactant species in the subcloud-layer and the cloud layer. Figure 12 shows the time evolution of the sub-cloud layer mixing ratio and the cloud layer mixing ratio for the inert compound and ozone, nitric oxide and the generic hydrocarbon. Although the mixing ratio are higher for all the species in the sub-cloud layer, it is noticable the role of shallow cumulii in ventilating species to higher altitudes within the boundary layer. Notice also that the amount of specices ventilated is dependent on their chemical reactivity (for instance compare the inert compound with the nitric oxide and the hydrocarbon). Further research will be addressed to better quantified this effect by conditional averaging.

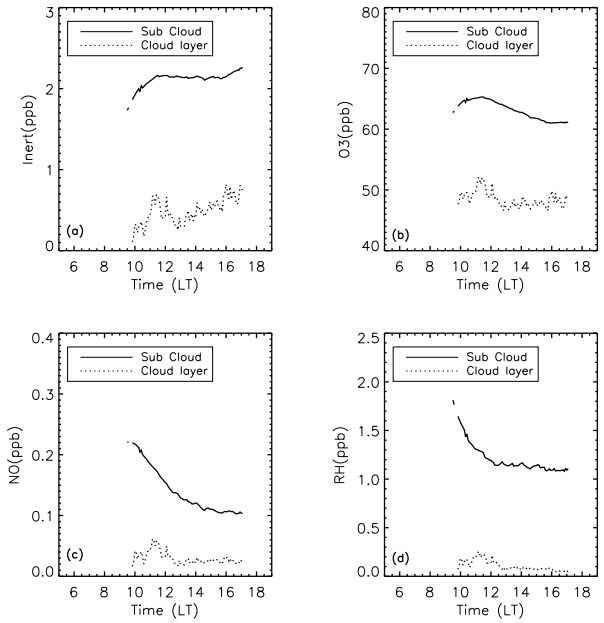

Figure 12: *Time evolution of the bulk mixing ratio in the subcloud layer and the cloud layer for (a) inert, (b) O_3, (c) N) and (d) generic hydrocarbon RH.*

4 Conclusions

The spatial distribution and evolution of the system $O_3 - HO_x - NO_x - CO$ influenced by the dynamic and radiative processes associated to shallow cumuli field is simulated by using the large-eddy simulation DALES. These first results show the capacity of reproducing the dynamic, radiation and chemical transformation with a high degree of accuracy. Therefore, we are confident that the DALES-chemistry will allow us to carry out process studies and support data interpretation of the turbulent-radiative reacting flows influenced by the presence of clouds.

The presence of clouds increases the volume in which species are transported, which leads to a dilution of reactant mixing ratio within the boundary layer. Mixing ratios of tracers below cloud decrease by up to 12% while mixing ratios averaged in the volume defined from the surface to the maximum elevation where tracers are vertically transported decrease by up to 50% compared to the clear sky situation. Furthermore, reactants transported to elevated regions remain at those levels following the clouds dissipation, which should have an effect on simulating nocturnal chemistry of the residual layer. The vertical flux profile show a large variation with height due to the chemical transformations and the cloud dynamics. In consequence, flux divergence should be taken into account in inferring flux estimation from upper air observations.

The perturbation of photodissociation rates due to the presence of clouds is discussed comparing a simulation that uses a photodissociation rate perturbed by the cloud with one that uses clear sky values. By analyzing the instantaneous fields of the mixing ratio, we find differences up to a 40% below the cloud base height and up to 20% close to cloud top, which indicates a large variability in the reactant distribution, an important aspect in the interpretation of the chemical processes in and around clouds.

References

[1] Brown, A. R., R. T. Cederwall, A. Chlond, P. G. Duynkerke, J. Golaz, J. M. Khairoutdinov, D. Lewellen, A. Lock, M. K. Macveen, C. Moeng, R. A. J. Neggers, A. P. Siebesma and B. Stevens, Large-eddy simulation of the diurnal cycle of shallow cumulus convection over land. *Quart. J. Roy. Meteorol. Soc.*, 128(B), 1075–1094, 2002.

[2] Chang, J., R. Brost, I. Isaksen, S. Madronich, P. Middleton, W. Stockwell and C.J.Walcek, A three-dimensional eulerian acid deposition model: physical concepts and formulation. *J. Geophys. Res.-Atmosphere*, 92, 14681–14700, 1987.

[3] Cotton, W. R., G. Alexander, R. Hertenstein, R. Walko, R. McAnelly and M. Nicholls, Cloud venting- a review and some new global annual estimates. *Earth Science Reviews*, 39, 169–206, 1995.

[4] Dosio, A., J. Vilà-Guerau de Arellano, A. A. M. Holtslag and P. J. H. Builtjes, Dispersion of a passive tracer in buoyancy- and shear-driven boundary layers. *J. Appl. Meteorol.*, 42, 1116–1130, 2003.

[5] Früh, B., T. Trautmann, M. Wendisch and A. Keil, Comparison of observed and simulated NO_2 photodissociation frequencies in a cloudless atmosphere and in continental boundary layer clouds. *J. Geophys. Res.-Atmosphere*, 105, 9843–9857, 2000.

[6] Joseph, J. H., W. J. Wiscombe and J. A. Weinman, The delta-Eddington approximation for radiative transfer flux. *J. Atmos. Sci.*, 33, 2452–2458, 1976.

[7] Krol, M. C., M. J. Molemaker and J. Vilà-Guerau de Arellano, Effects of turbulence and heterogeneous emissions on photochemically active species in the convective boundary layer. *J. Geophys. Res.-Atmosphere*, 105, 6871–6884, 2000.

[8] Madronich, S., Photodissociation in the atmosphere: 1. Actinic fluxes and the effects of ground reflections and clouds. *J. Geophys. Res.-Atmosphere*, 92, 9740–9752, 1987.

[9] Stephens, G., The parameterization of radiation for numerical weather prediction and climate models. *Mon. Wea. Rev.*, 112, 826–867, 1984.

[10] Vilà-Guerau de Arellano, J., S. Kim, M. C. Barth and E. G. Patton, Transport and chemical transformations influenced by shallow cumulus over land. *Atmos. Chem. Phys.*, 5, 3219–3231, 2005.

On LES of Particle Laden Flow: The Effect of the Subgrid Scale Turbulence

C. Gobert, A. le Duc, M. Manhart

TU München, Fachgebiet Hydromechanik, Germany.
ch.gobert@bv.tum.de

Abstract

This paper focuses on the simulation of particle laden flow by Large Eddy Simulation (LES). In LES, the smallest scales are not resolved. In this work we investigate the effect of the smallest scales on particles transported with the flow. We conduct an a priori and an a posteriori analysis (i.e. DNS and LES) of homogeneous isotropic turbulence at $Re_\lambda = 34.1$ and $Re_\lambda = 50$. The particles are tracked in Lagrangian formulation.

We found that, dependent on Stokes number (i.e. particle diameter and density respectively), the effect of the small scales can be considerable. At first sight, one might assume that the effect of small scale turbulence is largest for inertia free particles. In the present work we present results that suggest that this assumption might not always be valid.

1 Introduction

Particle laden flows in nature often reach Reynolds numbers for which direct numerical simulation (DNS) is not possible on nowadays computers. For detailed numerical predictions of such flows, large eddy simulation (LES) is considered to be an appropriate method. This paper focuses on the simulation of a particle-laden flow by LES.

In a LES, the Navier-Stokes equations are solved on a grid coarser than the smallest scales of the flow field. In order to reconstruct the effect of the unresolved scales (subgrid scales, SGS), on the resolved scales, a model is required. In the present work, this model is referred to as fluid-SGS model.

In many applications (e.g. prediction of sedimentation processes, dispersion of aerosols in the atmosphere) a suspension of rigid particles is present in the flow. Often the dynamics of the carrier fluid are only of secondary interest; it is more important to predict the distribution of the suspended phase.

A recently published review article by Guha [10] gives a comprehensive overview of state of the art computational methods for particle laden flows and relevant transport mechanisms. For the non-specialist, we give a brief description of a selection of such transport mechanisms, namely dispersion, preferential concentration, preferential sweeping and turbophoresis.

Dispersion means spreading out of particles due to turbulence, i.e. in a turbulent flow a small cloud of particles will grow in size. This effect was already analyzed by Taylor [25] and later in more detail by many other authors such as Reeks [18] or Wang and Stock [28].

Preferential concentration, preferential sweeping and turbophoresis lead to an inhomogeneous distribution of particles in the flow due to various mechanisms. Preferential concentration stands for inhomogeneities resulting from centrifugal forces acting on particles swirling in a vortex [8, 22, 31, 2]. Preferential sweeping results from the interaction of centrifugal forces and gravity [27]. Due to preferential sweeping, turbulence can increase the sink velocity of suspended particles. Turbophoresis stands for an effect found in wall bounded particle laden flows. Due to inhomogeneities in turbulent kinetic energy, particles may tend to accumulate close to walls [3, 19, 33]. According to these authors, the particles "flee" from turbulence, thus the word "turbophoresis".

It is still unknown to which extend these effects can be reconstructed in LES. It is not evident which of the mechanisms mentioned evolve due to large scale effects only (resolved in LES) and which ones are effected by small scale turbulence (not resolved in LES). In dependence on particles and flow, the corresponding eddies might be in the subgrid range and a particle-SGS model will be required.

Up to now, only a few particle-SGS models were proposed. For example Wang and Squires [29] proposed a particle-SGS model based on the reconstruction of the kinetic energy seen by the particles. They solve a transport equation for the SGS kinetic energy and model the SGS fluctuations as random process for tracing particles. Another model was proposed by Shotorban and Mashayek [21]. They solve a Langevin equation in order to reconstruct the SGS fluctuations seen by the particles. These are both stochastic models. Kuerten proposed a deterministic model [12]. In this model, the particles see a fluid velocity field where the smallest resolved scales of the LES are amplified. This method is called approximate deconvolution method (ADM).

All these models show certain benefits and deficits. For example, it is clear that an ADM model cannot reconstruct effects of unresolved scales; an ADM model amplifies the effects of the scales which are merely resolved. Stochastic models can reconstruct the effects of unresolved scales. Shotorban and Mashayek show that their stochastic model gives good results for particles with small inertia but shows deficits for particles with large inertia.

Thus, the development of a particle-SGS model is still an unsolved issue. In order to develop a new particle-SGS model it is important to know which assumptions on the small scales are valid and which effects are to be modeled. In this work we attempt to describe the effects of small eddies on the particles. We do not propose a specific model but we try to find out which quantities should be reconstructed by a model, i.e. in this work we do not aim at constructing a particle-SGS model but we analyze the most relevant effects of the smallest scales.

Our work is closely related to an analysis conducted by Fede and Simonin [7]. They analyzed the effects of small scales on particles by DNS of isotropic turbulence at Taylor-microscale based Reynolds number $Re_\lambda = 34.1$. In their work, they record velocity statistics

along particle trajectories in order to quantify turbulence seen by the particles. They differentiate between small scale and large scale turbulence with the aid of spatial spectral filters at various cutoff wave numbers (a priori analysis).

In the present work, we conducted an a priori and an a posteriori analysis of isotropic turbulence at Taylor-microscale based Reynolds numbers of $Re_\lambda = 34.1$ and $Re_\lambda = 50$. A priori analysis means comparison of DNS data and filtered DNS data, a posteriori analysis means comparison of DNS and LES data. We compute particle dynamics for a wide range of particle diameters and particle density, respectively (Stokes numbers based on the Kolmogorov time scale range between $St = 0$ and $St = 100$). In comparison to the work by Fede and Simonin, we cover a wider range of parameters (Reynolds and Stokes numbers) and, in addition to the a priori analysis, we conduct an a posteriori analysis. On the other hand, we do not study variations of the filter used in the a priori analysis.

2 Numerical simulation of the carrier fluid

In this paper, we investigate forced isotropic turbulence. We performed a DNS of the carrier fluid by solving the Navier-Stokes equations for incompressible flows of Newtonian fluids

$$\operatorname{div} \mathbf{u} = 0 \tag{1}$$

$$\frac{\partial \mathbf{u}}{\partial t} + \mathbf{u}.\nabla \mathbf{u} = -\frac{1}{\rho}\nabla p + \nu \Delta \mathbf{u}. \tag{2}$$

Here, $\mathbf{u}$ represents the fluid velocity, ρ the density, ν the kinematic viscosity and p the pressure.

For solving equations (1) and (2), we used a Finite-Volume method. This method is a modified version of the projection or fractional step method proposed independently by [4] and [26]. For spatial discretization a second order scheme (mid point rule) was implemented. For advancing in time, we use the third order Runge-Kutta scheme proposed by Williamsson [30] with constant time step Δt. The continuity equation (1) is satisfied by solving the Poisson equation for the pressure.

Isotropic turbulence enforces periodic boundary conditions in all three directions. Therefore, the Poisson equation could be solved by a direct method using Fast-Fourier transformations. In a parallel computation, this would involve a large communication overhead. We circumvented this by solving the Poisson equation by an iterative solver proposed by Stone [23].

Turbulence was forced with a slightly modified version of the deterministic forcing scheme proposed by Sullivan et al. [24]. They propose a forcing scheme where the energy in the spectral modes below a certain wave number κ_1 is held constant. With this forcing scheme we could not observe an increase of energy in the low wave number range, i.e. the spectrum's peak coincides with the lowest resolved wave number. This is in contrast to the spectrum one obtains using e.g. the forcing schemes by Eswaran and Pope [6] or Overholt and Pope [16]. In order to facilitate comparison with works using one of these forcing schemes, we decided to force only the modes in a given range $[\kappa_0, \kappa_1]$. Thus, in contrast to Sullivan et al. we do not force the modes at the lowest resolved wave numbers. This is in accordance with the forcing schemes proposed by Eswaran and Pope and Overholt and Pope and leads to a decay in the spectrum at the smallest wave numbers.

We computed the flow at two Reynolds numbers, namely $Re_\lambda = 34.1$ and $Re_\lambda = 50$. The Reynolds number $Re_\lambda = \frac{\lambda u_{\mathrm{rms}}}{\nu}$ is based on the transverse Taylor microscale λ and the rms value of one (arbitrary) component of the fluctuations u_{rms}.

In all computations the flow was solved in a cube on a staggered Cartesian equidistant grid. The size of the computational box and the cell width was chosen in dependence of the Reynolds number.

Fede and Simonin [7] studied particle laden isotropic turbulence by DNS at $Re_\lambda = 34.1$. In order to facilitate comparison of the present work to their work, we performed the DNS at $Re_\lambda = 34.1$ with the same dimensions of the computational domain and the same cell width Δx as they did, namely a box of length $L = 16.23\lambda$ and cells of width $\Delta x = 0.1268\lambda$.

The larger the Reynolds number, the wider the range between the largest and smallest scales. In order to cover the whole spectrum, we followed the advice given by Pope [17]. We set the computational box to at least 11 integral length scales and used a grid with cell width Δx less than $1.5\eta_K$ where η_K is the Kolmogorov length scale. In table 1 this information is summarized.

DNS		
Re_λ	34.1	50
L/λ	16.23	24.50
$\Delta x/\lambda$	0.1268	0.09570
$\Delta x/\eta_K$	1.46	1.31
N	128^3	256^3
$[\kappa_0, \kappa_1]\lambda$	[1.0, 1.5]	[0.5, 1.5]
$\epsilon\lambda/u_{rms}^3$	0.4414	0.2825
η_K/λ	0.08694	0.07295
$\tau_K u_{rms}/\lambda$	0.2578	0.2661
L_f/λ	1.485	1.882

Table 1: Simulation parameters and Eulerian statistics from DNS of forced isotropic turbulence. Reynolds number Re_λ, length of computational box L, cell width Δx, number of grid points N, range of forced wavenumbers $[\kappa_0, \kappa_1]$, rate of dissipation ϵ, Kolmogorov length scale η_K, Kolmogorov time scale τ_K and Integral length scale L_f.

In order to quantify the effect of the smallest scales on the particles, we conducted an a priori and an a posteriori analysis, i.e. DNS and LES. In the a priori analysis the particles were traced using the whole spectrum but for computing statistical quantities we filtered the fluid velocity using a box filter, i.e. we computed

$$\hat{\mathbf{u}}(\mathbf{x}, t) = \frac{1}{\Delta^3} \iiint_{[-\Delta/2, \Delta/2]^3} \mathbf{u}(\mathbf{x} + \mathbf{r}, t) d\mathbf{r}. \tag{3}$$

Δ is the filter width. In this work, we set Δ to $\Delta = 5\Delta x$. $\hat{\mathbf{u}}$ does not contain the high wavenumber fluctuations an thus mainly large scales. The effect of the small scales can be analyzed be comparing $\mathbf{u}$ with $\hat{\mathbf{u}}$.

In LES, only the large scales are resolved. Due to the LES model, an LES field will still be different from $\hat{\mathbf{u}}$. Therefore we also conducted Large Eddy Simulations, i.e. we solved the LES equations

$$\operatorname{div} \bar{\mathbf{u}} = 0 \tag{4}$$

$$\frac{\partial \bar{\mathbf{u}}}{\partial t} + \bar{\mathbf{u}}.\nabla \bar{\mathbf{u}} = -\frac{1}{\rho}\nabla \bar{p} - \operatorname{div} \tau + \nu \Delta \bar{\mathbf{u}}. \tag{5}$$

$\bar{\cdot}$ denoted filtering implied in the LES. $\tau_{ij} = \overline{u_i u_j} - \bar{u}_i \bar{u}_j$ is the SGS stress tensor. In a LES, $\overline{u_i u_j}$ cannot be computed directly because not $\mathbf{u}$ but $\bar{\mathbf{u}}$ is computed. Thus, τ needs to be modeled (fluid-SGS model). We implemented the Lagrangian dynamic Smagorinsky model proposed by [14]. Parameters for the LES can be found in table 2.

Forcing in LES was accomplished in the same manner as for DNS, i.e. the energy in the forced wave numbers is identical in DNS and LES. In LES, the energy in the high wavenumber spectrum is not resolved. Thus, the resolved kinetic energy

$$\bar{k}_f = \frac{1}{2L^3 T} \int_0^T \iiint_{[0,L]^3} \bar{u}_i^2(\mathbf{x}, t) d\mathbf{x} dt \qquad (6)$$

is less than in DNS. All data were made dimension free by normalizing with the DNS quantities $u_{rms} = \sqrt{\frac{2}{3} k_f}$ and λ. More details for the flow solver can be found in [13].

	LES	
Re_λ	34.1	50
L/λ	16.23	24.50
$\Delta x/\lambda$	0.5073	0.3828
N	32^3	64^3
$\bar{k}_f/k_f$	0.871	0.891

Table 2: Parameters for LES of forced isotropic turbulence.

The spectra from LES and DNS are plotted in figure 1. The spectra show that all scales are well resolved in DNS. In LES, a significant part of the high wavenumber spectrum is not resolved.

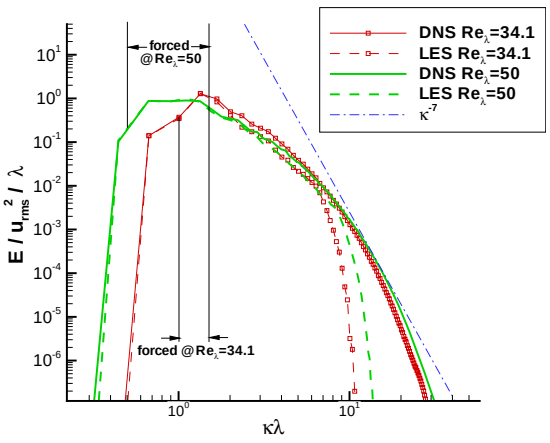

Figure 1: *Instantaneous energy spectrum functions from LES and DNS at $Re_\lambda = 34.1$ and $Re_\lambda = 50$ together with a line proportional to κ^{-7}.*

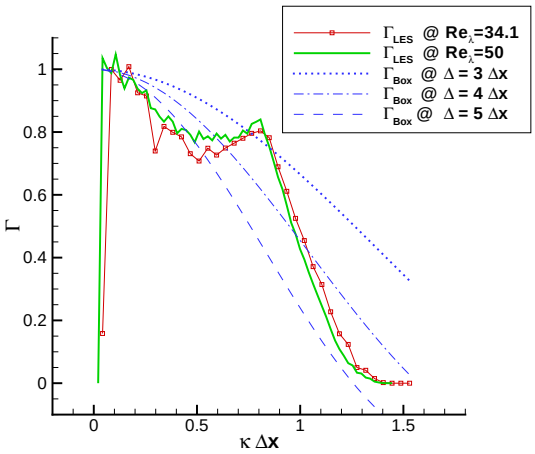

Figure 2: *Filter transfer functions from comparison of DNS and LES data (a posteriori analysis, equation (7)) and of a box filter at various filter widths (for the a priori analysis, equation (8)).*

The resolution of the LES and the filter width were chosen such that LES data and filtered DNS data are comparable. The LES model and LES resolution given in table 2 implicitly define a filter transfer function Γ_{LES}. This can be computed a posteriori from

$$\Gamma_{LES}(\kappa) = \left(\frac{\bar{E}(\kappa)}{E(\kappa)} \right)^{1/2}. \qquad (7)$$

Here, $\bar{E}(\kappa)$ is the energy spectrum function from LES and $E(\kappa)$ is the energy spectrum function from DNS.

We chose the filter width of the box filter such that its transfer function is comparable to Γ_{LES}. Therefore we computed the transfer function for a box filter Γ_{box} at filter width Δ,

$$\Gamma_{box}(\kappa) = \frac{2 \sin(0.5 \kappa \Delta)}{\kappa \Delta}. \qquad (8)$$

In figure 2, these transfer functions are shown for the performed simulations and for a box filter with $\Delta = 3\Delta x$, $\Delta = 4\Delta x$ and $\Delta = 5\Delta x$. For $\Delta = 4\Delta x$, the square deviation $\|\Gamma_{box} - \Gamma_{LES}\|_{L^2}$ is minimized. This shows that $\Delta = 4\Delta x$ would be a good choice for the filter width.

On the other hand, in a finite volume context, cell averages are computed. Thus, integrals over complete cells are known. If the filter width is set to $\Delta = 4\Delta x$, then $\mathbf{u}$ must be integrated in each coordinate over 3 complete and 2 half cells. In this case, an approximation error from integration would occur. Therefore we did not use $\Delta = 4\Delta x$ but we set $\Delta = 5\Delta x$. Then, integrals can be evaluated exactly.

3 Discrete particle simulation

For computing the suspended phase, single particles are traced. In this study we focus on dilute suspensions. Thus, only effects of the fluid on the particles are considered; effects of the particles on the fluid and particle-particle interactions are neglected (one way coupling).

For computing traces of particles we assume that the acceleration of a particle $\frac{d\mathbf{v}}{dt}$ is given by Stokes drag only,

$$\frac{d\mathbf{v}}{dt} = -\frac{c_D Re_p}{24 \tau_p} (\mathbf{v} - \mathbf{u}). \qquad (9)$$

Here, $\mathbf{v}(t)$ denotes the particle velocity. τ_p is the particle relaxation time, i.e. the timescale for the particle to adapt to the velocity of the surrounding fluid. The particle Reynolds number Re_p is based on particle diameter and particle slip velocity $\|\mathbf{u}-\mathbf{v}\|$ which leads to a nonlinear term for the Stokes drag. The drag coefficient c_D was computed in dependence of Re_p according to the scheme proposed by Clift et al. [5].

The fluid velocity $\mathbf{u}$ must be evaluated at the particle position $\mathbf{x}_p(t)$, i.e. $\mathbf{u} = \mathbf{u}(\mathbf{x}_p(t), t)$. Hence, these values must be interpolated. Yeung and Pope [32] and Balachandar and Maxey [1] recommend the use of third or fourth order interpolation schemes. Meyer and Jenny [15] showed that, in addition, conservativity of the interpolation scheme is an important issue. If the interpolation scheme is not conservative, particles may cluster due to numerical errors. In the present work, this is an issue because we analyze inhomogeneities in the particle distribution. Thus, we decided to use the second order conservative scheme described in [9].

In DNS, equation (9) was solved together with the Navier-Stokes equations (1) and (2). In LES, we solved

$$\frac{d\bar{\mathbf{v}}}{dt} = -\frac{c_D Re_p}{24\tau_p}(\bar{\mathbf{v}} - \bar{\mathbf{u}}) \tag{10}$$

together with the filtered Navier-Stokes equations (4) and (5).

In this study we considered particles at Stokes numbers $St = \frac{\tau_p}{\tau_K}$ in the range from $St = 0$ to $St = 100$ based on the Kolmogorov time scale τ_K. For small Stokes numbers, the Stokes drag is a stiff term. The numerical scheme for integrating equations (9) and (10) must be capable to handle this. We solved equations (9) and (10) by a Rosenbrock-Wanner method (see e.g. [11]). This method is a fourth order method with adaptive time stepping. The stiff term in equations (9) and (10) is linearized in each time step and discretized by an implicit Runge-Kutta scheme.

In all simulations we traced 24 fractions of particles with 80000 particles per fraction. The Stokes numbers of the 24 fractions range from 0 to 100 based on the Kolmogorov time scale, i.e. $0 \leq \tau_p \leq 100\tau_K$. The particles were initialized at random positions (homogeneous distribution) inside the computational box and traced until a statistical steady state was obtained. Then, 1000 time records were taken with a time interval of $\Delta t = 0.25\lambda/u_{rms}$. With this time interval, the Lagrangian correlation functions could be resolved for all Stokes numbers.

4 Analysis of the SGS turbulence seen by the particles

The motivation behind this work is to provide data for the development of a particle-SGS model. LES with a perfect fluid- and particle-SGS model would give, in a statistical sense, the same particle trajectories as DNS. Therefore we analyzed particle statistics in the a priori analysis along exact trajectories, i.e. we solved the particle transport equation (9) using the (unfiltered) fluid velocity $\mathbf{u}$ and not the filtered velocity $\hat{\mathbf{u}}$. $\hat{\mathbf{u}}$ was recorded along the particle paths to differentiate between large scale and small scale turbulence but $\hat{\mathbf{u}}$ did not affect the particle trajectories.

In the a posteriori analysis particle trajectories were computed by solving equation (10). No particle-SGS model was employed. In the following a priori and a posteriori results all statistics are based on averaging over particles and time, denoted by $\langle\cdot\rangle$.

In isotropic turbulence, long-term dispersion can be computed from the product of kinetic energy of the particles and the Lagrangian integral time scale which is a characteristic time scale of the autocorrelation of particle velocity [25]. Therefore, we analyzed the effects of small scale turbulence on kinetic energy and integral time scale.

4.1 Kinetic energy of the fluid

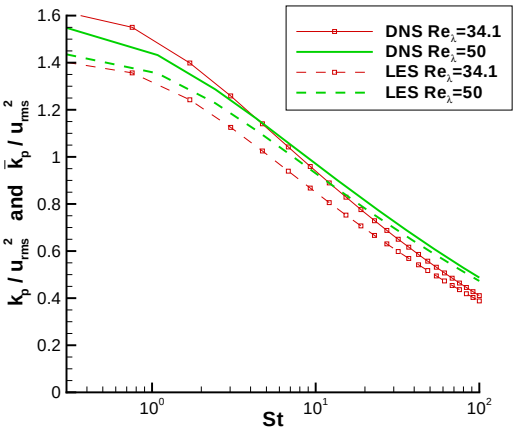

Figure 3: *Kinetic energy of the particles at* $Re_\lambda = 34.1$ *and* $Re_\lambda = 50$. *Results from DNS and LES.*

The kinetic energy of the carrier fluid in DNS is greater than in LES, $k_f > \bar{k}_f$ (cf. table 2). Thus, it is to be expected that the kinetic energy of the particles in DNS is greater than in LES,

$$k_p = \frac{1}{2}\langle v_i^2 \rangle \; > \; \frac{1}{2}\langle \bar{v}_i^2 \rangle = \bar{k}_p. \tag{11}$$

In figure 3 the kinetic energy of the particles k_p and $\bar{k}_p$ is shown. Evidently equation (11) holds and at large Stokes number the kinetic energy of the particles decreases. This is because high Stokes number particles are not affected by small scale (i.e. high frequency) fluctuations in the carrier fluid due to their inertia.

At high Stokes numbers, k_p and $\bar{k}_p$ collapse. Thus, the kinetic energy of particles with high Stokes number is independent of small scales.

A question addressed in several works [20, 29, 7] is whether preferential concentration is an effect of large scale or small scale turbulence. In the present framework we address this question by comparing the effects of Stokes number St on kinetic energy of the fluid seen by the particles in DNS and in LES. If mainly small scale turbulence drives preferential concentration, then particle distributions in LES will differ to a great extend from particle distributions in DNS. This should be detectable in the kinetic energy of the fluid seen by the particles.

We recorded kinetic energy from DNS

$$k_{f@p} = \frac{1}{2}\left\langle u_i^2(\mathbf{x}_p, t)\right\rangle, \tag{12}$$

filtered DNS data

$$\hat{k}_{f@p} = \frac{1}{2}\left\langle \hat{u}_i^2(\mathbf{x}_p, t)\right\rangle \tag{13}$$

and kinetic energy from LES

$$\bar{k}_{f@p} = \frac{1}{2}\left\langle \bar{u}_i^2(\mathbf{x}_p, t)\right\rangle . \qquad (14)$$

$\hat{k}_{f@p}$ and $\bar{k}_{f@p}$ differ due to the difference in filtering and LES model (i.e. difference between Γ_{box} and Γ_{LES}) and due the different particle trajectories.

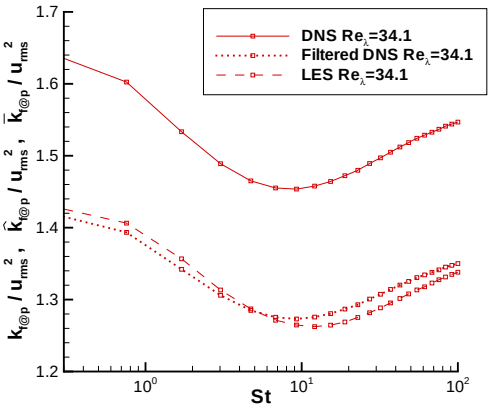

Figure 4: *Kinetic energy of the carrier fluid seen by the particles at* $Re_\lambda = 34.1$. *Results from DNS, filtered DNS and LES.*

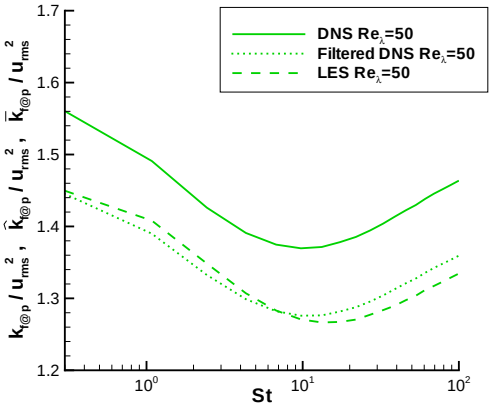

Figure 5: *Kinetic energy of the carrier fluid seen by the particles at* $Re_\lambda = 50$. *Results from DNS, filtered DNS and LES.*

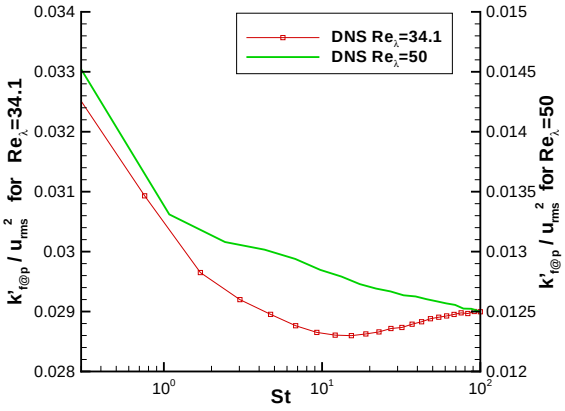

Figure 6: *Kinetic energy of the small scales of the carrier fluid seen by the particles at* $Re_\lambda = 34.1$ *(left axis) and* $Re_\lambda = 50$ *(right axis). Results from the a priori analysis (i.e. DNS and filtered DNS).*

In figures 4 and 5 these energies are depicted. An effect of the Stokes number on $k_{f@p}$ can be observed. At first this effect is surprising because in the simulations the particles do not affect the carrier flow (one way coupling), i.e. k_f does not depend on Stokes number. On the other hand, $k_{f@p}$ is sampled along particle trajectories which differ for different Stokes numbers. This underlines inhomogeneities in the spatial particle distribution, i.e. preferential concentration. Particles with Stokes numbers of about $St \approx 10$ accumulate in regions of low kinetic energy. It can be seen that $\bar{k}_{f@p}$ is very close to $\hat{k}_{f@p}$. This means that the inhomogeneity of particle distributions is mainly recovered by LES and suggests that in the present configuration preferential concentration is an effect of the large scales.

A somewhat different question is whether the Stokes number dependence of $k_{f@p}$ is due to variations in the energy of large eddies or energy contained in small structures. This question can be addressed in the a priori analysis. In figure 6, the kinetic energy of the small scale fluctuations of the fluid seen by the particles computed in the a priori analysis

$$k'_{f@p} = \frac{1}{2}\left\langle \left(u_i\left(\mathbf{x}_p, t\right) - \hat{u}_i\left(\mathbf{x}_p, t\right)\right)^2\right\rangle \qquad (15)$$

is depicted. It should be noted that for limiting Stokes number $St = 0$ and $St = \infty$, the kinetic energy at particle locations $k_{f@p}$ tends towards $k_{f@p} = 1.5u_{rms}^2$ because particles are distributed uniformly at these Stokes numbers. Because of the same reason, $k'_{f@p} = k_{f@p} - \hat{k_{f@p}}$ for these Stokes numbers.

Figures 4 to 6 give evidence that, for small $St < 10$, particles with higher Stokes number tend to concentrate at locations with lower kinetic energy. This holds for both Reynolds numbers and for large and small scale kinetic energy. For higher Stokes numbers, we observe different behavior dependent on Reynolds number. For the smaller $Re = 34.1$ we observe that both, large and small scale kinetic energies increase with Stokes number $St > 10$. At $Re = 50$, the large scale kinetic energy at particle locations shows a minimum at $St = 10$ and tends towards the theoretical limiting value, but the small scale kinetic energy at particle location decreases monotonously over the Stokes number range considered. The different behavior between $Re = 34.1$ and $Re = 50$ might be due to the difference in filter width.

4.2 Analysis of the SGS turbulence seen by the particles - integral time scale

The life time of small eddies is very low, i.e. small scale fluctuations in the carrier fluid are seen as high frequency fluctuations by the particles. High frequency fluctuations of the carrier flow lead to high frequency fluctuations in the particle velocity. Therefore, the small scales lead to faster decorrelation of the particle velocity. This effect can be seen in the Lagrangian correlation functions of the particle velocity from DNS and LES

$$R_p(\tau) = \frac{\langle \mathbf{v}(t).\mathbf{v}(t+\tau)\rangle}{\langle \mathbf{v}(t).\mathbf{v}(t)\rangle} \qquad (16)$$

$$\bar{R}_p(\tau) = \frac{\langle \bar{\mathbf{v}}(t).\bar{\mathbf{v}}(t+\tau)\rangle}{\langle \bar{\mathbf{v}}(t).\bar{\mathbf{v}}(t)\rangle}, \qquad (17)$$

depicted in figure 7. R_p decays faster than $\bar{R}_p$, i.e. particle velocity decorrelates faster in DNS than in LES.

The rate of decay of R_p can be quantified by the Lagrangian integral time scale

$$t_p = \int_0^\infty R_p(\tau)d\tau. \tag{18}$$

The smaller the integral time scale, the shorter is the time span within which the velocity of a particle is autocorrelated. Figure 8 shows the integral time scale from DNS t_p and LES

$$\bar{t}_p = \int_0^\infty \bar{R}_p(\tau)d\tau. \tag{19}$$

It is apparent that the scales resolved in DNS but not in LES lead to shorter integral time scales, i.e. faster decorrelation.

Closely related to the autocorrelation of the particle velocity and its integral time scale is the autocorrelation of the fluid velocity seen by the particle and its integral time scale

$$R_f(\tau) = \frac{\langle \mathbf{u}(\mathbf{x}_p(t),t).\mathbf{u}(\mathbf{x}_p(t+\tau),t+\tau)\rangle}{\langle \mathbf{u}(\mathbf{x}_p(t),t).\mathbf{u}(\mathbf{x}_p(t),t)\rangle} \tag{20}$$

$$t_{f@p} = \int_0^\infty R_f(\tau)d\tau. \tag{21}$$

Again, large scale and small scale effects can be separated by comparing $t_{f@p}$ with the integral time scale computed from filtered DNS and LES data,

$$\hat{t}_{f@p} = \int_0^\infty \hat{R}_f(\tau)d\tau \tag{22}$$

$$\bar{t}_{f@p} = \int_0^\infty \bar{R}_f(\tau)d\tau \tag{23}$$

where $\hat{R}_f$ and $\bar{R}_f$ are defined as in equation (20) but $\mathbf{u}$ is replaced by $\hat{\mathbf{u}}$ and $\bar{\mathbf{u}}$ respectively. $t_{f@p}$, $\hat{t}_{f@p}$ and $\bar{t}_{f@p}$ are depicted in figure 9.

Wang and Stock [28] give an analytical expression for $t_{f@p}$ in dependence on Stokes number. They point out that for $St \to \infty$ the particles do not move any more and thus $t_{f@p}$ converges towards the Eulerian integral time scale. This asymptotical behavior can be seen in figure 9.

In figure 10, the difference between $t_{f@p}$ and $\bar{t}_{f@p}$ is plotted. The maximum deviation is attained between $St = 7$ and $St = 10$, dependent on Reynolds number. This result means that the significance of small scale turbulence does not always decrease with Stokes number.

It is clear that for $St \to \infty$ particles are not affected by turbulence. Thus, one might assume that the significance of small scale turbulence is maximized for $St = 0$. The results shown in figure 10 are in contrast to this assumption. Based on these results, we conclude that the effect of small scale turbulence on inert particles can be greater than on inertia free particles.

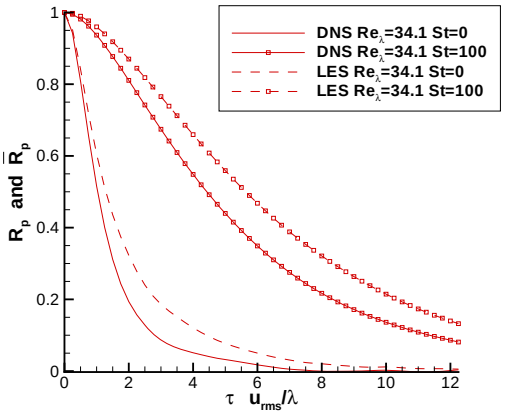

Figure 7: *Lagrangian correlation function of the particle velocity from LES and DNS at* $Re_\lambda = 34.1$ *and* $Re_\lambda = 50$. *Stokes numbers shown:* $St = 0$ *and* $St = 100$.

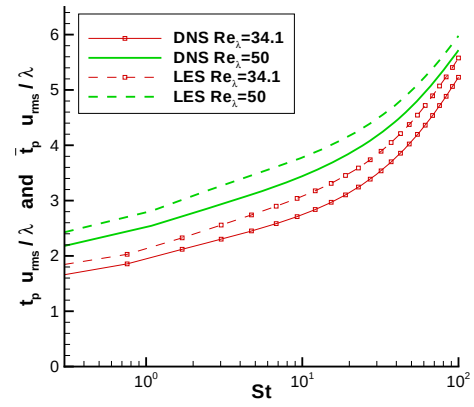

Figure 8: *Lagrangian integral time scale of the particle velocity from LES and DNS at* $Re_\lambda = 34.1$ *and* $Re_\lambda = 50$.

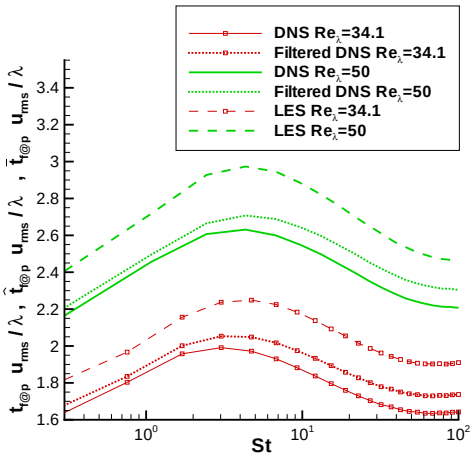

Figure 9: *Lagrangian integral time scale of the fluid velocity seen by the particles from DNS, filtered DNS and LES at* $Re_\lambda = 34.1$ *and* $Re_\lambda = 50$.

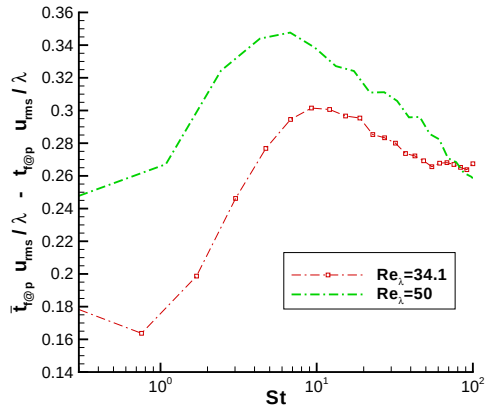

Figure 10: *Difference between DNS and LES results for the Lagrangian integral time scale of the fluid velocity seen by the particles at* $Re_\lambda = 34.1$ *and* $Re_\lambda = 50$.

5 Conclusion

In this work, the effect of small scale turbulence on a suspended phase was investigated. DNS and LES of particle laden forced homogeneous isotropic turbulence was conducted. The effect of small eddies was quantified by comparing DNS to filtered DNS data (a priori analysis) and by comparing DNS to LES data (a posteriori analysis).

Aim of this work is to provide insight to the effect of small scale turbulence on suspended particles in order to construct a particle-SGS model that is capable to reconstruct the desired effects on the suspended phase at high Reynolds numbers where DNS is not possible.

Particle dispersion depends on kinetic energy and integral time scale. Thus, we focused on these two quantities. The analysis showed that in LES kinetic energy is underestimated and integral time scale is overestimated for all Stokes numbers. Furthermore, we analyzed the flow seen by the particles. From this, we draw conclusions on preferential concentration.

One might assume that the effect of the small scales is maximized at $St = 0$ because inertia free particles follow small changes in the flow instantly. In our work we found that this assumption is not always justified. We recorded the autocorrelation function of the fluid velocity seen by the particles. In LES, this function decays slower than in DNS. We found that in our configuration the rate of decay computed from DNS and LES deviates most between $St = 7$ and $St = 10$ (Stokes number based on the Kolmogorov time scale). This suggests that it is not obvious that the effect of the small scales is maximized for inertia free particles.

References

[1] S. Balachandar and M. R. Maxey. Methods for evaluating fluid velocities in spectral simulations of turbulence. J. Comput. Phys., 83(1), 1989.

[2] J. Bec, L. Biferale, M. Cencini, A. Lanotte, S. Musacchio, and F. Toschi. Heavy particle concentration in turbulence at dissipative and inertial scales. Phys. Rev. Lett., 98(8), 2007.

[3] M. Caporaloni, F. Tampieri, F. Trombetti, and O. Vittori. Transfer of particles in nonisotropic air turbulence. J. Atmos. Sci., 32:565Ű568, March 1975.

[4] A. J. Chorin. Numerical solution of the Navier Stokes equations. Math. Comput., 22, 1968.

[5] R. Clift, J. R. Grace, and M. E. Weber. Bubbles, Drops and Particles. Academic Press, New York, 1978.

[6] V. Eswaran and S. B. Pope. An examination of forcing in direct numerical simulations of turbulence. Computers and Fluids, 16(3):257Ű278, 1988.

[7] P. Fede and O. Simonin. Numerical study of the subgrid fluid turbulence effects on the statistics of heavy colliding particles. Phys. Fluids, 18(4), 2006.

[8] J. R. Fessler, J. D. Kulick, and J. K. Eaton. Preferential concentration of heavy particles in a turbulent channel flow. Phys. Fluids, 6(11):3742Ű3749, November 1994.

[9] C. Gobert, F. Schwertfirm, and M. Manhart. Lagrangian scalar tracking for laminar micromixing at high schmidt numbers. In Proceedings of the 2006 ASME Joint U.S.-European Fluids Engineering Summer Meeting, Miami, Fl., 2006.

[10] A. Guha. Transport and deposition of particles in turbulent and laminar flow. Ann. Rev. Fluid Mech., 40(1):311Ű341, 2008.

[11] E. Hairer and G. Wanner. Solving Ordinary Differential Equations II. Stiff and Differential-Algebraic Problems. Springer Series in Computational Mathematics. Springer-Verlag, 1990.

[12] J. G. M. Kuerten. Subgrid modeling in particleladen channel flow. Phys. Fluids, 18, 2006.

[13] M. Manhart. A zonal grid algorithm for DNS of turbulent boundary layers. Computers and Fluids, 33(3):435Ű461, 2004.

[14] C. Meneveau, T. S. Lund, and W. H. Cabot. A lagrangian dynamic subgrid-scale model of turbulence. J. Fluid Mech., 319:353Ű385, 1996.

[15] D. W. Meyer and P. Jenny. Conservative velocity interpolation for pdf methods. Proc. Appl. Math. Mech., 4(1):466Ű467, December 2004.

[16] M. R. Overholt and S. B. Pope. A deterministic forcing scheme for direct numerical simulations of turbulence. Computers and Fluids, 27(1):11Ű28, January 1998. [17] S. B. Pope. Turbulent Flows. Cambridge University Press, 2000.

[18] M. W. Reeks. On the dispersion of small particles suspended in an isotropic turbulent fluid. J. Fluid Mech., 83:529Ű546, 1977.

[19] M. W. Reeks. The transport of discrete particles in inhomogeneous turbulence. J. Aerosol Sci., 14(6):729Ű739, 1983.

[20] B. Shotorban and F. Mashayek. Modeling subgridscale effects on particles by approximate deconvolution. Physics of Fluids, 17(8), 2005.

[21] B. Shotorban and F. Mashayek. A stochastic model for particle motion in large-eddy simulation. Journal of Turbulence, 7, 2006.

[22] K. D. Squires and J. K. Eaton. Preferential concentration of particles by turbulence. Phys. Fluids, 3:1169Ű1178, May 1991.

[23] H.L. Stone. Iterative solution of implicit approximations of multidimensional partial differential equations. SIAM J. Num. Anal., 5(3):530Ű558, 1968.

[24] N. P. Sullivan, S. Mahalingam, and R. M. Kerr. Deterministic forcing of homogeneous, isotropic turbulence. Phys. Fluids, 6(4), 1994.

[25] G. I. Taylor. Diffusion by continuous movements. Proceedings of the London Mathematical Society, s2-20:196Ű212, 1922.

[26] R. Temam. On an approximate solution of the Navier Stokes equations by the method of fractional steps (part 1). Arch. Ration. Mech. Anal, 32, 1969.

[27] L. P. Wang and M. R. Maxey. Settling velocity and concentration distribution of heavy particles in homogeneous isotropic turbulence. J. Fluid Mech., 256:27Ű68, 1993.

[28] L. P. Wang and D. E. Stock. Dispersion of heavy particles by turbulent motion. J. Atmos. Sci., 50, 1993.

[29] Q. Wang and K. D. Squires. Large eddy simulation of particle-laden turbulent channel flow. Phys. Fluids, 8(5):1207Ű1223, 1996.

[30] J. H. Williamson. Low-storage Runge-Kutta schemes. J. Comput. Phys., 35, 1980.

[31] C. Y. Yang and U. Lei. The role of the turbulent scales in the settling velocity of heavy particles in homogeneous isotropic turbulence. J. Fluid Mech., 371:179Ű205, September 1998.

[32] P. K. Yeung and S. B. Pope. An algorithm for tracking fluid particles in numerical simulations of homogeneous turbulence. Journal of Computational Physics, 79(2), 1988.

[33] J. Young and A. Leeming. A theory of particle deposition in turbulent pipe flow. J. Fluid Mech., 340:129Ű159, June 1997.

Numerical Modeling of Particulate Matter Behaviour in Urban Ground Surface Boundary Layer

J. Pospisil & M. Jicha

Brno University of Technology, Czech Republic.
pospisil.j@fme.vutbr.cz & jicha@fme.vutbr.cz

Abstract

This paper introduces CFD technique for modeling of PM10 (particulate matter 10μm) behavior in urban areas, with focus on description of processes in the ground surface boundary layer. Description of deposition and re-suspension processes is introduced and applied on the regional numerical model of the city of Brno. The threshold velocity of re-suspension was obtained from the small scale modeling of PM10 dispersion in a street canyon located inside the regional model. Predicted concentration fields were compared with theoretical studies and in situ measurement.

1 Introduction

Increasing of the PM (particulate matter) concentration level in cities stimulates an intensive research focused on better understanding of particles behavior during their lifetime period in urban areas. The highest concentrations of PM are generally present in inner parts of urban areas, specifically at a close vicinity of major traffic paths. Many parameters influence formation, transport and deposition of particles at these locations. Particles behavior is influenced by transportation in moving air, settling due to gravity, interaction with buildings walls, deposition on a ground surface and re-suspension of once deposited particles that are lifted by a local air movement and dispersed into surroundings. Therefore, particles behavior is very complex process difficult for an accurate mathematical description.

The numerical models for prediction of PM concentration fields in urban areas fall in two categories: i) a detail solution of PM dispersion processes with simplified quantification of PM sources [1] and ii) a solution of concentration fields for gas species (NOx) with a known correlation to PM [2]. The CFD modeling falls in the both groups and represents the only tool capable to take into account detail geometry of urban areas and the interaction between moving cars and ambient air [3]. Numerical models of large areas are necessary for a correct description of long-distance PM10 transport. On the other side, small scale models are necessary for a detailed prediction of PM concentrations in a close vicinity of traffic paths. Nesting of both types of numerical models enables correct, complex and effective numerical prediction of PM concentration fields.

It is impossible to accurately quantify production of all real PM sources in urban areas. In this study we focus on sources directly connected with flow conditions of the ground surface boundary layer, namely deposition and re-suspension. Re-suspension represents the most intensive source of PM10 in large urban areas. Particles spend a long time in urban areas and travel through long distances. The deposition is one of the major possible ways of separation of PM10 from a lower part of atmosphere. In numerical models of urban areas the deposition is considered as a sink of PM10 (negative source).

2 Mathematical description

2.1 Particle deposition

Deposition occurs on all solid and liquid surfaces located in a polluted atmosphere. Particles deposition in a boundary layer is described with inclusion of turbulent transport and particle settling [4]

$$F = K\frac{dC}{dz} + v_s C \tag{1}$$

where v_s is the settling velocity of the particles, K is the eddy diffusivity for mass transfer of the species with the concentration C and F is the downward mass flux.

The eddy diffusivity is correctly solved by CFD technique in fully turbulent flow. Wall functions substitute the accurate solution of eddy diffusivity in surface boundary layers. Close to the surface, the eddy diffusivity is nearly zero. The Brownian diffusivity of particles greater than 1 m is near zero too. The downdraft mass flux is then controlled by the deposition velocity calculated as [5]

$$v_s = \frac{D_p^2 \rho_p g C_c}{18\mu} \tag{2}$$

where D_p and ρ_p are respectively the particle diameter and density, υ is the air dynamic viscosity, g is the gravitational acceleration. C_c is the slip correction factor expressed as

$$C_c = 1 + \frac{2\lambda}{d_p}\left[1.257 + 0.4\exp(-\frac{1.1 d_p}{2\lambda})\right] \tag{3}$$

where λ is the mean free path of gas molecules.

2.2 Particle re-suspension

From different studies [6] follows that re-suspension of once deposited particles is the most intensive source of urban airborne particles during 'dry periods'. Re-suspension process of once deposited particles depends on an actual air velocity field above the ground surface, a local slit load, a surface roughness, particle geometry and other particle parameters. Coarse particles (d>2.5μm) are very often able to re-suspend from dry surfaces. On the other side, fine particles and ultra fine particles show only limited tendency to re-suspend from all surfaces. This results from a significant amount of a liquid fraction forming particles smaller than 2.5μm and existence of the Van der Waals force between ultra-fine particles

and surfaces. Re-suspension of particles is generally impossible from wet and adhesive surfaces. From above mentioned follows that the re-suspension process is very complex and its mathematical description is generally connected with high value of uncertainty.

The re-suspension of particles settled on surfaces results from interaction of aerodynamic, electrostatic and mechanical forces, Fig. 1.

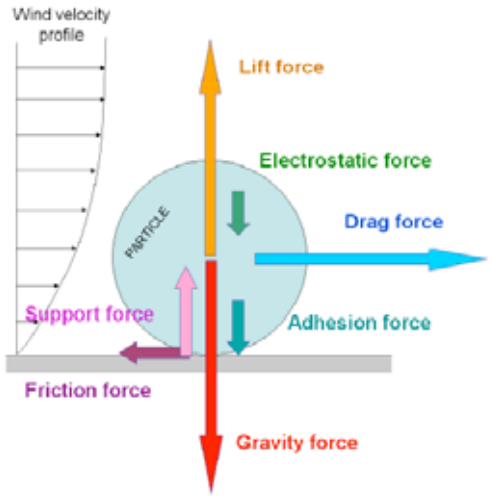

Figure 1: *Particle interaction of aerodynamic, electrostatic and mechanical forces.*

The Saffman lift force due to a velocity gradient near walls is important aerodynamic interaction. This lift force is oriented perpendicularly to a direction of flow affecting deposited particles in a viscous fluid.

An electro static force on the charged particles can be calculated only for the known particle charge and the magnitude of electric field. This information is not common for dispersion studies and the electro static force is commonly excluded from the calculations.

The Saffman lift force and the fluid turbulence are sufficient to suspend fine and ultra fine particles. Coarse particles are often moved by the drag force along the surface. The turbulent intensity of a stream can also influence the air drag force affecting particles. The drag force affecting particles in boundary layer was expressed in form [7]

$$F_d = \frac{\pi d^2 C_{fx} \rho U^2}{8} \tag{4}$$

where C_{fx} is the local shear stress coefficient, ρ is the air density, U is the free-stream air flow velocity. An irregular shape of particles together with a surface roughness cause irregular bouncing of particle against walls. This behavior prepares good conditions for the following lift up of particles in a boundary flow.

Various forms of equations can be found in literature for determination of the windblown dust flux. Algorithms solve the dust flux either from the wind velocity and the threshold wind velocity (5) [8] or from the friction velocity and the threshold friction velocity (6) [9]

$$F = C_{TF} u^2 (u - u_t) \tag{5}$$

where F is the dust flux, u is the wind velocity, u_t is the threshold wind velocity and C_{TF} is the constant representing character of the soil surface (disturbed/undisturbed).

$$F = C u_*^3 a_g \left(u_* - u_{*t}\right) \tag{6}$$

where a_g is the constant expressing effect of non-instantaneous wind velocity (1.2), u_* is the friction velocity, u_{*t} is the threshold friction velocity and C is an empirical constant.

The friction velocity for a neutrally stable atmosphere can be determined in a couple of ways. From the logarithmic wind velocity profile, the wind velocity is related to the friction velocity as

$$u = \frac{u_*}{k} \ln\left(\frac{z-d}{z_0}\right) \tag{7}$$

where k is the von Karman constant (0.4), z_0 is the aerodynamic roughness length and d is the displacement height.

The wind velocity of re-suspension is the lowest velocity of air at the height 10m above the ground, for which the re-suspension represents a significant contribution in an urban air PM10 concentration. The wind threshold velocity of the re-suspension is strongly influenced by an actual geometry of an urban area, air density and geometry of particles. From carried out studies, the corresponding urban threshold velocity of the re-suspension is 2.4m for the studied area.

The previous section discussed the wind threshold velocity of re-suspension with utilizing of the driving wind velocity above the 'buildings roof' level. But numerical models describing processes in boundary layer require much more detail approach to a correct description of re-suspension. From this reason, we focussed on the particular street canyon in the city of Brno. The numerical model of the studied canyon was build up. Series of calculations were carried out with focus on detail description of an air flow above a ground and a road surface. We considered spherical particles with diameter 10m, density of particles 1200kg/m3, parametrical roughness of surface 0.0003m and wind profile displacement 0m. The street canyon threshold velocity of re-suspension was determined as 0.75m/s (at height 0.35m). Different studies on determination of the threshold velocity of particle re-suspension were carried out in recent years. Majority of these studies considered particle re-suspension from a flat horizontal surface that fit well to detail solution of a bottom part of the studied street canyon. We compared the predicted street canyon threshold velocity of re-suspension 0.75m/s with results derived from formulations published by Cornelis and Gabriels [10] and Saho and Lu [11]. From the Cornelis and Gabriels [10] formulation, we derived the threshold velocity of re-suspension 0.724m/s. From the Saho and Lu [11] formulation, we derived the threshold velocity of re suspension 0.957m/s. The predicted street canyon threshold velocity of re-suspension for PM10 particles showed good agreement with the mentioned theoretical studies.

3 Simplified description of particles deposition and re-suspension fluxes

It is impossible to accurately quantify production of all real PM sources. Therefore, an appropriate simplification of particles production description is convenient for a numerical solution of PM concentration fields.

The simplification used in this study assumes equivalence between the particles deposition rate on smooth dry surfaces and the particles re-suspension rate from these surfaces influenced by wind velocity higher than the threshold velocity of re-suspension. Stable deposition is assumed on grassy surfaces and smooth dry surfaces influenced by wind velocity lower than the threshold veloc-

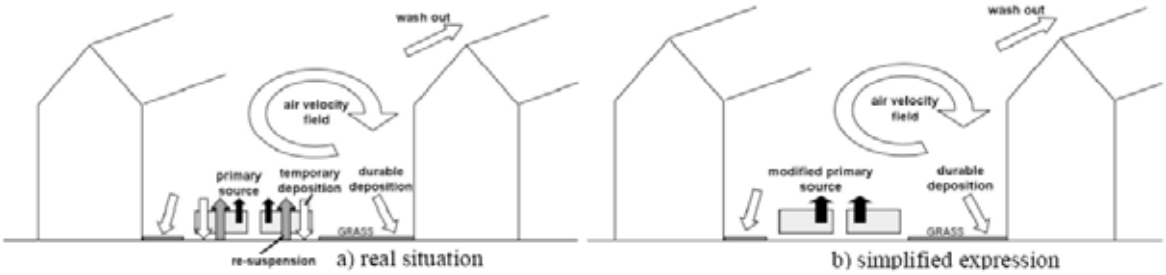

Figure 2: *Particles fluxes in a street canyon.*

ity of re-suspension. The modified primary source term represents the only particles source term prescribed in the numerical model, see fig. 2. The modified primary source was assigned in the near road surface air layer, where major amount of airborne particles is generated. From this air layer, particles disperse into surrounding.

4 PM10 dispersion modeling on regional scale model

Above mentioned description of deposition and re-suspension was utilized for PM10 dispersion modeling on a regional model. The regional solution domain involves the city of Brno and a nearby surrounding. The solution domain covers an area of 12x12km. Due to large modeled area, it is impossible to accurately involve geometry of all objects. The parametrical roughness is used as a convenient substitution of ground cover geometry. The primary ground surface was build up in accordance with the actual terrain profile. The regional model ground plan was divided in 576 square control regions with the side length 500m. A convenient parametrical roughness was assigned within these regions.

The ground cover was divided in seven groups that represent the most common ground covers in the studied area. Corresponding parametrical roughness values were derived for all considered ground covers: water surface, meadow, forest, separate buildings up to 3 floors, continuing buildings rows up to 3 floors, separate buildings above 3 floors, continuing buildings rows above 3 floors. The primary ground surface was refined at terminal control volumes size with the top view dimensions 50x50m. The 900m high air layer was modeled above the primary ground surface. This air layer was subdivided into 19 sub-layers. The lowest sub-layer height was 2.125m and the highest sub-layer height was set to 100m.

4.1 Traffic related PM sources

The primary car exhaust emission factor is determined for considered car fleet composition - diesel engines to petrol engines = 1 to 3. The particular emission factor values were derived from software MEFA v.02 (Mobile Emission FActors) published by the Ministry of Environment of the Czech Republic. The primary car exhaust emission factor value was determined as 0.0179g/km car.

A non-exhaust particle source related with traffic involves primary particles and the re-suspended particles. Primary non-exhaust particles are released from cars, tires and road surfaces. The emission factors of non-exhaust particles released from cars and tires can be derived from different studies. Amount of the primary road surface particles is a function of a road surface material and an actual road state. Re-suspended particles are silt road particles drawn up from a road surface. The re-suspension process intensity is fully dependant on an actual road silt load. The total PM10 emission factor is a sum of the exhaust particles emission factor and the non-exhaust emission factors. The average total PM emission factor of the regional model domain was derived from a previous study carried out in the studied area as 0.06265g/km car.

A corresponding traffic activity was derived from the Brno Transport Research Center database. Portions of traffic paths passing through individual control regions (500x500m) were specified. A traffic activity (car km/day) at traffic paths portions was multiplied by the total emission factor. The average total PM emission factor serves for the determination of the only particles source term prescribed in the numerical model. The source term was assigned at the air layer close to the ground surface, where major quantity of airborne particles is generated.

The inlet/outlet boundary conditions were assigned on side walls of the regional model. The ground surface utilizes the wall boundary condition with appropriate parametrical roughness. The top of the domain uses condition of a wall with no friction. As a model of turbulence, $k - \epsilon$ *RNG* model was used.

5 Results and discussion

In calculations, we presume coarse spherical particles with diameter 10m. Density of the particles is set to 1200kg/m3. The figure 3 shows the predicted PM10 concentration field obtained from the regional model for wind velocity 2 m/s and 3 different wind directions. The cuts of concentration fields are drawn in height 3m above the ground surface. The left column in the Fig.3 collects concentration fields obtained from calculations without inclusion of deposition. The right column shows the results with inclusion of deposition process. Inclusion of the deposition process decreases PM10 concentration only by 1-4% in central parts of the city due to small areas enabling a durable deposition. The decrease of PM10 concentration by 8-17% is observed in residential areas of the city. The most intensive decrease of PM10 concentration occurs in outskirts areas richly covered by greens and forests. The PM10 concentration fields show higher concentration along roads with the highest traffic rate. At the bottom of the concentration fields, the interstate highway passes around the city. Intensive traffic on this highway causes significantly higher PM10 concentrations along this traffic path.

The regional background PM10 concentration 15g/m3 was derived from a measurement carried out outside of the urban area. The north part of the city of Brno is without any intensive local sources of par-

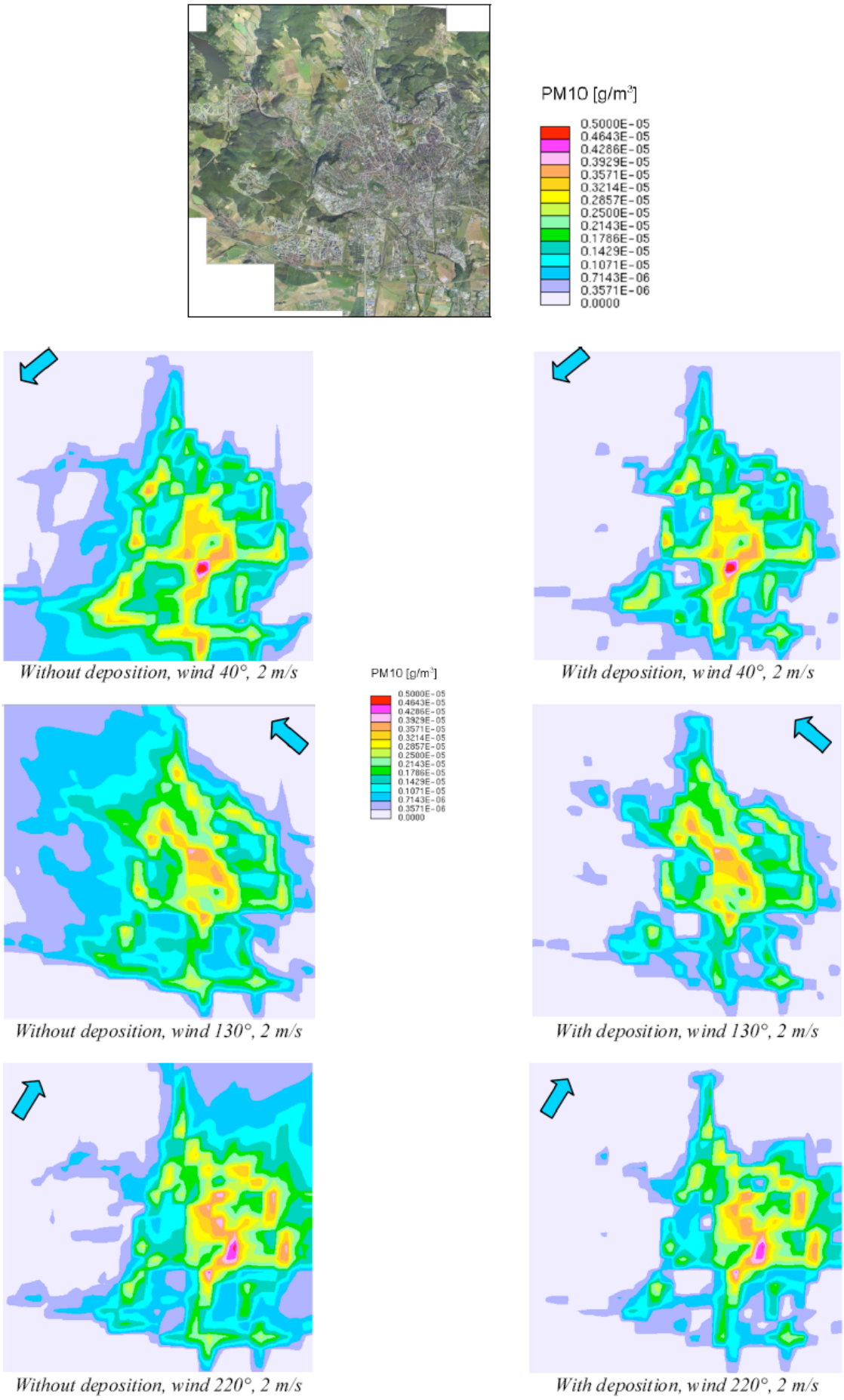

Figure 3: *Predicted PM10 concentration fields 3m above ground surface.*

ticles. This part of the city serves as residential areas without industry. The total predicted PM10 concentration is calculated as the sum of the predicted concentration and the regional background concentration. The result of this calculation is 23.5g/m3 at the position of the measurement located in central part of the city. From measurement, we obtained the PM10 concentration value 45g/m3.

6 Conclusion

The presented study shows a possible inclusion of deposition and re-suspension of PM10 particles in a regional scale dispersion model solved by CFD technique. The CFD modeling represents convenient tool for detail PM dispersion modeling in urban areas. But the accuracy of these predictions is still limited due to high uncertainty of PM source description and limited possibilities for correct description all physical processes.

The predicted PM10 concentration field with inclusion of deposition and re-suspension process represents 52.2% of the PM10 concentration value obtained from measurements in the central area of the city of Brno. The result shows that the predicted concentration values significantly underestimate the measured concentration values. The difference is probably caused by an intensive re-suspension of soil particles. This process is not taken into account in the numerical models due to difficult description of its source term.

Acknowledgements

The Czech Ministry of Transport under the grant 1F54H/098/520 financially supported this work.

References

[1]Flemming, J. 2003: Immisionsfelder aus Beobachtung, Modellirung und deren Kombinationen, Dissertation zur Erlangung des Doktoratgrades, Freie Universität Berlin.

[2]Kukkonen, J. a kol. 2001: A semi-empirical model for urban PM10 concentrations, and its evaluation against data from an urban measurement network. Atmospheric Environment 35, 4433-4442.

[3]Jícha M., Pospisil J., Katolicky J. 2000: Dispersion of pollution in street canyon under traffic induced flow and turbulence, Environmental monitoring and assessment, 65, 343-351.

[4]Csanady G.T. 1973: Turbulent Diffusion in the Environment, Reidel, Dordrecht, Holland.

[5]Simpson D., Fagerli H., Jonson J. E., Tsyro S. and Wind P. 2003: Unified EMEP Model Description - EMEP Status Report 1/2003, Norwegian Meteorological Institute.

[6]Moussiopoulos N. et al. 2003: Air Quality in Cities, Final Report of project SATURN: Subproject EURO-TRAC-2, ISBN 3-540-00842-x, Springer, Germany.

[7]Punjrath J.S. and Heldman D. R., 1972: Mechanisms of small particle re-entrainment from flat surface, Aerosol Science, 3, 429-440.

[8]Tegen, I. and Fung, I. 1994: Modelling of mineral dust in the atmosphere: Sources, transport, and optical thickness, Geophys. Res. Lett. 99, 22897-22914.

[9]Claiborn, C.S., Lamb, B., Miller, A., Beseda, J., Clode, B., Vaughan, J., Kang, L., and Newvine, C. 1998: Regional measurements and modelling of windblown agricultural dust: The Columbia Plateau PM10 Program, J. Geophys. Res. 103, 19753-19768.

[10]Cornelis W. M., Gabriels D and Hartmann R. 2004: A Parameterisation for the Threshold Shear Velocity to Initiate Deflation of Dry and Wet Sediments, Geomorphology 59, 43-51.

[11]Saho Y and Lu H 2003: A simple expression for wind erosion treshold friction velocity, Journal of Geophysical Research 1005 (D17), 22,437-22,443.

3D-2D Transition in Inhomogeneous Rotating Turbulent Flow

B. Lüthi[1], M. Kinzel[2], A. Liberzon[3], M. Holzner[1], C. Tropea[2], W. Kinzelbach[1], A. Tsinober[3,4]

[1] *Institute of Environmental Engineering IFU, ETHZ, Switzerland.*
[2] *Department of Fluid Mechanics and Aerodynamics SLA, Technische Universität Darmstadt, Germany.*
[3] *School of Mechanical Engineering, Tel Aviv University, Israel.*
[4] *Marie Curie Chair in Fundamental and Conceptual Aspects of Turbulent Flows, Imperial College, United Kingdom.*
luethi@ifu.baug.ethz.ch

Abstract

A particle tracking velocimetry (PTV) experiment of an inhomogeneous turbulent flow in a rotating tank is presented. Oscillating grid forcing at the top of a tank produces turbulence, which propagates away from the grid and becomes quasi two-dimensional (2D) after some distance and time. Our emphasis is on the 3D-2D transition. We find that the transition to 2D occurs at a distance y^* corresponding to a local Rossby number $Ro(y^*) \sim 0.3$. After a few Ω^{-1} turnover times the region below y^* becomes quasi 2D with regard to velocity.

1 Introduction

The rotating fluid system under investigation is closely related to applications in geophysics, e.g. [1]. As an example, large-scale atmospheric and oceanic flows are known to be quasi two-dimensional (2D), but with distinct features of three-dimensional turbulence on smaller scales [2]. Traditionally, most of the attention was dedicated to flows that develop into an undisturbed infinite environment. However, most real flows do not develop freely, for example they can be bounded (by walls, stratification, etc.) so that there is an upper limit for the integral length scale (e.g. stratified layers in the ocean) or they can be subject to rotation (e.g. geophysical flows). The understanding of these effects is up to now incomplete, see for example the recent review [3].

From previous experiments (e.g. [4]) it is known that when the Rossby number is low enough, i.e. $Ro(y) = u(y)/(2\Omega L(y)) \sim 0.2$ the flow seizes to be 3D but instead the formation of so called Taylor columns can be observed. They are parallel to the axis of rotation and their axial extension is of the order of the entire domain depth. The number of such Taylor columns increases with increasing Reynolds number and increasing rotation rate Ω of the reference system. Their formation has been associated with inertial waves, see for example [4].

Experiments with identical forcing conditions, but with the flow seeded with Kalliroscopic markers, revealed how very quickly tube-like structures start to form at the edge of the turbulent layer at y^* (see figure 1). These 2D structures, also known as Taylor columns (e.g. [4]), propagate towards the bottom of the tank at constant speed, while the 3D turbulence remains confined within a small region close to the grid.

In a slightly different experiment, when the grid starts to oscillate in the rotating tank, the turbulent flow (generated by the oscillating grid) propagates downwards with $H(t) \propto f(t)$ ($f(t)$ has being a target of our previous study [5] to validate the propagation law of $exp(-t)$, predicted by [6]). The question arises whether the time t^* for the turbulent front to reach the location y^* is longer or shorter than the time scale t_{2D} needed for the 3D-2D transition.

In this work we intend to study the nature of the 3D-2D transition. Additional questions involved are: Do the horizontal vorticity components vanish in the region of transition? How sharp is the transition? How are the Taylor columns related to the 3D turbulent region? In this note we report results for the field of velocity and acceleration. In a following study we will investigate the behavior of the velocity gradient tensor.

2 Method

An oscillating grid setup (see Ref. [7] for more details) is located on a rotating table as it is shown in Fig. 1. We use a fractal grid following [8]. We have rectangular bars with three fractal iterations and a bar length of 4 mm. The bar thickness varies from 1 to 2 mm. The grid is installed near the upper edge of a water filled glass tank with dimensions 200 x 200 x 300 mm^3 and oscillates vertically at 9 Hz with a stroke of $\pm$4 mm. The individual jets and wakes created by the motion of the grid bars interact and at sufficient distance from the grid, the flow becomes turbulent as it propagates away from the grid. The turbulence is considered nearly isotropic and homogeneous in planes parallel to the driving grid.

The 3D-PTV experiments were conducted by using a high-speed camera (Photron Ultima APX, 1,024 $\times$ 1,024 pixels) at a frame rate of 125 Hz. The maximum recording time at this frame rate is 49 s. The camera is triggered by the onset of grid motion. We use mirrors to split the view into four separate images that allow to perform PTV with a single camera only, which on a rotating table with confined space is of great advantage. The beam of a continuous 25 Watt Ar-Ion laser is expanded through two cylindrical lenses to form a laser sheet of 30 mm thickness which passes through the midplane of the tank. The camera records the light scattered by neutrally buoyant polystyrene tracer particles with a diameter of 100 μm. In order to reach rigid body rotation as initial condition, a long spin-up time of 30 minutes was necessary. This required that the density of the fluid was precisely matched to the density of the flow markers. Accurate density matching was reached at 1.048 g cm^{-3} by adding NaCl to the fluid in a 1 : 12 mixing ratio.

Here we compare the results of two experiments: a) the case when the grid starts oscillating in a rotationg fluid at $\Omega = 0.75$ rad s^{-1} and b) a steady state case in

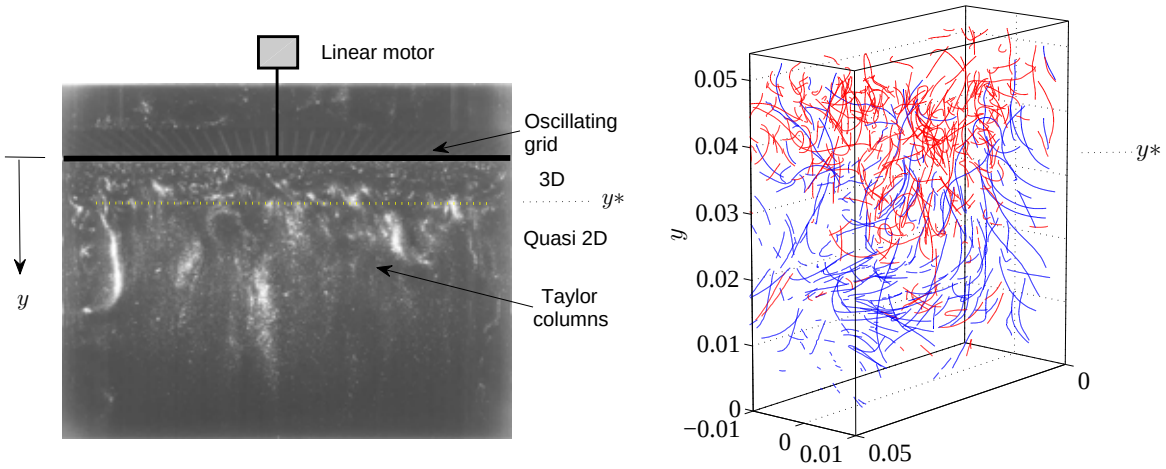

Figure 1: *Left - Flow visualization using Kalleroscopic markers and a schematic view of the setup. Right - Trajectories over 3 seconds of recording. Color (online) is defined by an acceleration threshold.*

which grid oscillation was started 10 min before recording, at $\Omega = 1.0$ rad s^{-1}. Each experiment produced 6100 frames per run that where processed using the method described in [9]. For a field of view of roughly $60 \times 60 \times 30$ mm^3 the final particle position accuracy is estimated at ± 5 μm.

3 Results

As a first result we show in figure 1b particle trajectories over 3 seconds of flow visualization. An acceleration threshold is used to render the 3D-2D transition. From an inspection of such plots a clear 3D-2D transition can be seen at about $y^* \approx 35$ mm distance from the lowest grid position for $\Omega = 0.75$ rad s^{-1} and at $y^* \approx 23mm$ for the slightly faster rotation of $\Omega = 1.0$ rad s^{-1}.

In a more quantitative approach, we measure the two-point correlation of the horizontal velocity components, with horizontal separation vectors for different distances from the grid ($\langle u(x) \cdot u(x+r) \rangle_y / \langle u(x)^2 \rangle_y$ where subscript y means averaging over horizontal planes). In figure 2 correlations for the situation 30 s after grid initiation are plotted. We note that the curves start to collapse at distance $y > 35$ mm away from the grid, indicating that the scale L, measured from these two-point correlations, does not grow anymore.

Similarly, in figure 3 a collapse of correlation curves occurs for $y > 23$ mm. Note that here the curves are not normalized with $\langle u(x)^2 \rangle_y$, and the velocity variance (i.e. $\langle u(x) \cdot u(x+r) \rangle_y \sim 6 \cdot 10^{-5}$ m^{2}s^{-2} for $r = 0$) is almost independent of y. It seems that for both runs we have identified a position y^* where the flow changes from 3D to 2D (figure 1) and we have constant $L^* \approx 13$ mm (L^* is defined using the area under the curve measured from $r = 0$ to the zero intersection). From figure 3 we can estimate the corresponding Rossby number $Ro(y^*) \approx 0.3$.

It is known ([10, 11]) that in non-rotating case, the root-mean-square of the turbulent velocity decays as $u_{\rm rms} \propto y^{-1}$, which was confirmed in our setup using 2D PIV [7].Interesting enough, at early times of the evolving case ($\Omega = 0.75$ rad s^{-1}), we find the same relation of $u_{\rm rms} \propto y^{-1}$ as it is shown in figure 4. As time progresses ($t > 30$ s) at some distance $y \sim 30$ mm from the grid u_{rms} starts to deviate from this law and becomes almost constant. This is consistent with the result on correlation curves mentioned above. For the stationary run ($\Omega = 1.0$ rad s^{-1}) the same phenomenon occurs closer to the grid, at $y \sim 20$ mm. We can therefore conclude that at a critical distance y^* the scale L, u_{rms} and also $Ro(y)$ (defined using the horizontal components) assume constant values and that y^* coincides with the visual observation of the flow becoming 2D. In the following we attempt to quantify the transition to the 2D flow.

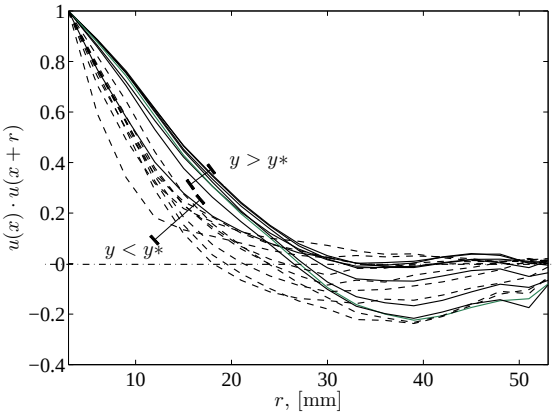

Figure 2: *Two-point velocity correlations for different distances from the grid, $\Omega = 0.75$ rad s^{-1}.*

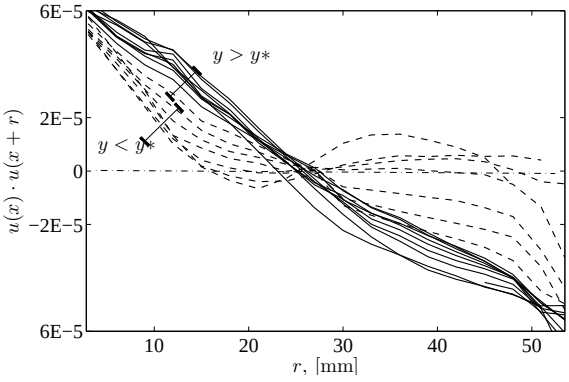

Figure 3: *Two-point velocity covariance for different distances from the grid, $\Omega = 1$ rad s^{-1}.*

In figure 5 we plot the ratio of horizontal to vertical acceleration components, again for early and later stages of the evolving and stationary experiments. We note that in the proximity of y^* the horizontal components start to dominate over the vertical ones and that

the ratio grows for $y > y^*$. It is interesting that there is no significant difference between the early, late and stationary curves, which possibly indicates that acceleration is being affected by the Coriolis force from the very beginning.

In figure 6 we show the cosine of the angle between velocity vector $\mathbf{u}$ and the vertical direction, conditioned on the distance y. Before the transition at $y < y^*$ the cosine is very close to a random distribution, as it appears in 3D isotropic turbulent flow. For $y > y^*$ however, we observe that for the evolving run, velocity becomes more horizontal and departs from the early curve somewhere at $y \approx 30$ mm. In the stationary run we observe the horizontal velocity orientation closer to the grid.

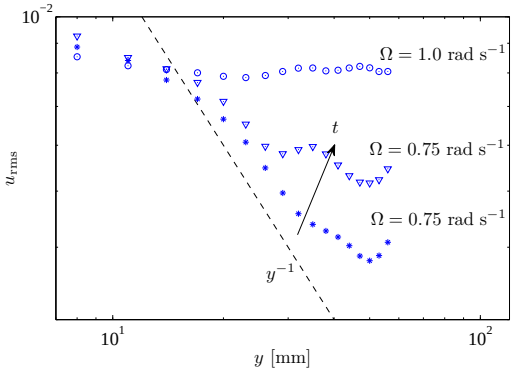

Figure 4: *Evolution of the root-mean-square of the horizontal velocity* $u_{\rm rms}$.

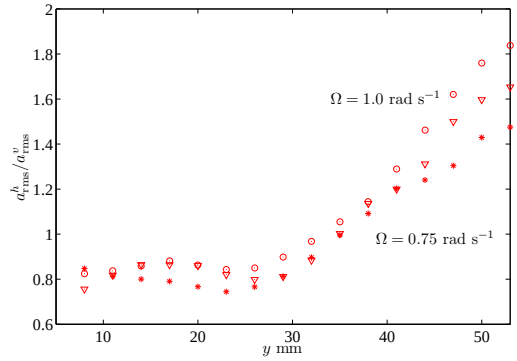

Figure 5: *Ratio of* $a^h_{\rm rms}$ *over* $a^v_{\rm rms}$ *for early, transient and stationary cases.*

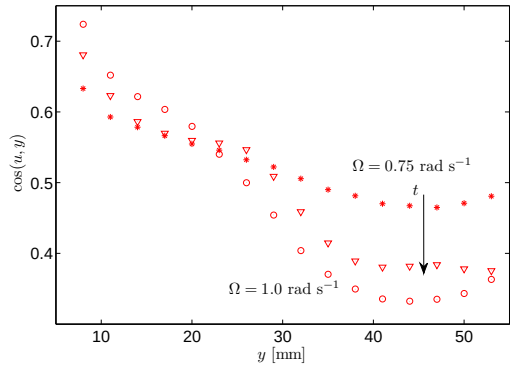

Figure 6: *Cosine of the angle between velocity and the vertical direction* y *for early, transient and stationary cases.*

In order to quantify the level of anisotropy we use the tensor of anisotropy introduced by [12] which is the deviator of the fluctuating velocity tensor, defined as $B_{ij} = \langle u_i u_j \rangle / \langle u^2 \rangle - 1/3\delta_{ij}$, where u^2 is the turbulent kinetic energy, and δ_{ij} is the Kronecker delta tensor. The anisotropy tensor is dimensionless, has zero trace, and vanishes identically if the turbulence is isotropic. This tensor has only two invariants, namely II and III, which are defined as $II = b_{ij}b_{ij}$ and $III = b_{ij}b_{jk}b_{ki}$. We present the distribution of the velocity fluctuations above and below y^* in figure 7. It is evident that for $y > y^*$ the flow becomes anisotropic and that it approaches the axisymmetric border of the invariant envelope.

4 Conclusions

Transition of turbulence from 3D to quasi 2D in inhomogeneous rotating turbulent flow was investigated by means of 3D-PTV. An oscillating grid drives the turbulence in a rectangular rotating tank. We find that the 3D turbulent flow remains confined to distances $y < y^*$ and becomes 2D for larger distances. We estimate the corresponding Rossby number to be $Ro(y^*) \approx 0.3$. The results for acceleration indicate an immediate effect of rotation in the very proximity of the grid. However, for velocity, we observe that the transition occurs only after a few Ω^{-1} turnover times.

It the next phase of this experiment we will zoom in on the region of transition in order to resolve also velocity gradients and to study their evolution in time, for example of the vortex stretching term $\omega_i\omega_j s_{ij}$ and the strain production term $-s_{ij}s_{jk}s_{ki}$. It is of interest whether the spatial gradients behave similar to acceleration (becoming 2D from the beginning) or if they have the time scale of the development of the velocity field, or if there is yet another alternative.

Acknowledgments

Alex Liberzon and Arkady Tsinober gratefully acknowledge the support of the ERCOFTAC and ETH visitor programs. Matthias Kinzel's research is performed under the support of DFG.

References

[1] J. Pedlosky. *Geophysical Fluid Dynamics.* Springer-Verlag, 2nd edition, 1987.

[2] H. Greenspan. *The Theory of Rotating Fluids.* Cambridge University Press, Cambridge, 1968.

[3] J. Westerweel J. C. R. Hunt, I. Eames. Mechanics of inhomogeneous turbulence and interfacial layers. *J. Fluid Mech.*, 554:449–519, 2006.

[4] E. J. Hopfinger, F. K. Browand, and Y. Gagne. Turbulence and waves in a rotating tank. *J. Fluid Mech.*, 125:505–534, 1982.

[5] M. Kinzel, M. Holzner, B. Lüthi, C. Tropea, W. Kinzelbach, and M. Oberlack. Scaling laws of turbulent diffusion - an experimental validation. Lisbon, Portugal, 2008. 14th Int Symp on Applications of Laser Techniques to Fluid Mechanics.

[6] M. Oberlack and S. Guenther. Shear-free turbulent diffusion, classical and new scaling laws. *Fluid Dynamics Research*, 33:453–476, 2003.

[7] M. Holzner, A. Liberzon, M. Guala, A. Tsinober, and W. Kinzelbach. Generalized detection of a turbulent front generated by an oscillation grid. *Exp. Fluids*, 41(5):711–719, 2006.

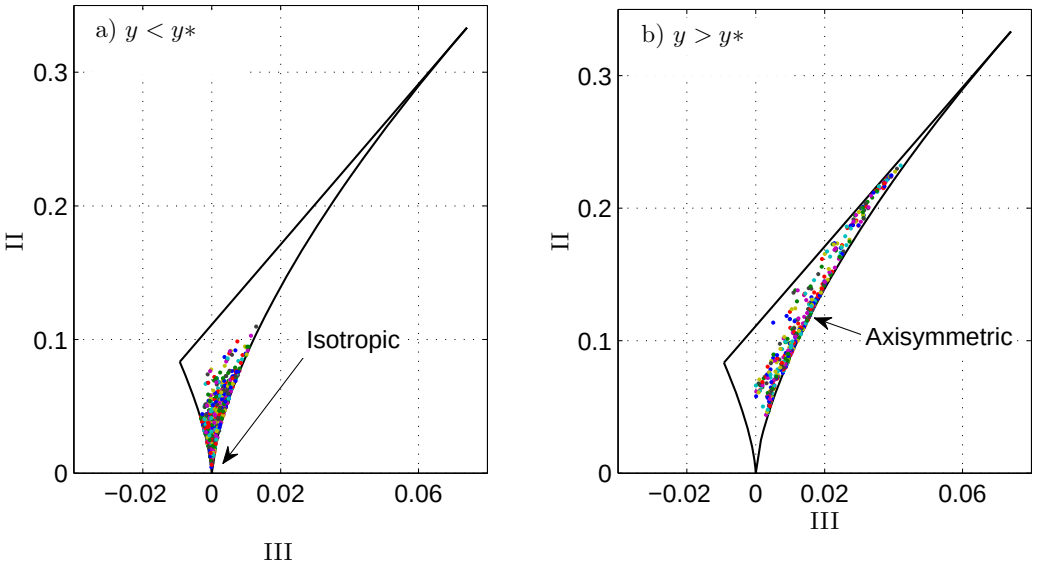

Figure 7: *Anisotropy invariant map of turbulent velocity in a region of (a) $y < y^*$ and (b) $y > y^*$, [12].*

[8] D. Hurst and J. C. Vassilicos. Scaling and decay of fractal-generated turbulence. *Physics of Fluids*, 19:035103, 2007.

[9] Beat Lüthi, Søren Ott, Jacob Berg, and Jakob Mann. Lagrangian multi-particle statistics. *J. of Turbulence*, 8(45):1–17, 2007.

[10] Robert R. Long. Theory of turbulence in a homogeneous fluid induced by an oscillating grid. *Physics of Fluids*, 21(10):1887–1888, October 1978.

[11] S.C. Dickinson and R.R. Long. Laboratory study of the growth of a turbulent layer of fluid. *Physics of Fluids*, 21(10):1698Ű1701, 1978.

[12] John L. Lumley and Gary R. Newman. The return to isotropy of homogeneous turbulence. *J. Fluid Mech.*, 82(1):161–178, 1977.

DNS and LEIS of Air-Sea Exchange Mechanisms

Djamel Lakehal

ASCOMP GmbH and ETHZ, Switzerland.
lakehal@ascomp.ch; www.ascomp.ch

1 Introduction

A recent report on the meeting's conclusions from the UNESCO-organized open symposium on The Ocean in a High-CO_2 World [1] points out that the ocean is one of the EarthŠs largest natural reservoirs of carbon and each year absorbs approximately one third of the CO_2 emitted by human activities. According to research from the National Oceanographic and Atmospheric Administration in the US (NOAA, an IOC Member State Agency), the ocean has taken up approximately 120 billion metric tons of carbon generated by human activities since 1800. The IOC reports that 20-25 million tons of CO_2 are added to the oceans each day. The salinity of oceans has thus tremendously increased over the last decades. Without bothering with the details, an increased salinity of the oceans will certainly impact the natural circulation of the streams. That these numbers are plausible or not should not prevent from 'ringing catastrophe bells', even if the uncertainty in the correlations used to estimate CO_2 uptake ranges today reaches 300% [2]. Clearly, there are considerable incentives to improve our understanding of scalar exchange phenomena and reduce such uncertainties, which have major impacts on policy related issues, for example, to the utilization of fossil fuels. Gas exchange problems also occur in numerous other environmental settings, such as desorption of dissolved substances, like PCBs, from inland and coastal water bodies, that can be of significant air quality concern.

Turbulence plays understandably a major role in controlling air-sea exchange mechanisms. Most of the laboratory and field data used to develop transfer models relate indeed the scalar exchange coefficient to far-field and/or interfacial turbulence, under various conditions; e.g. free surface flows, sheared or unsheared surfaces, etc. (see [3] for a comprehensive review of turbulence and scalar exchange). The same is true with the direct numerical simulations (DNS), although the studies known sofar including the data discussed in this paper were limited to low-to-mild shear Reynolds number flows ($Re_\tau < 200 - 300$). We will not only refer to DNS and experiments performed for the purpose of scalar transfer parametrization, but also evoke how far is now the research in terms of exploring the Large-Eddy Simulation (LES) alternative to cope with high Re air-sea flows, featuring more realistic wave breaking scenarios. The scalar transfer models to be discussed in this paper were indeed found to corroborate with both DNS and experiments, but at low Reynolds number flow conditions.

We will proceed as follows. First, we will briefly review two particular scalar exchange models, viz. the surface renewal ans surface divergence models. Second, we will consider the application of these models to recent DNS of coupled gas-liquid turbulence and scalar exchange across sheared deformable surfaces [4, 5, 6, 7]. The DNS studies referred to consider situations with a range of gas shear at the surface, with turbulence being generated at the interface itself, rather than elsewhere, e.g. at the bottom boundary of the flowing stream. We will finally review applications of the models to very recent laboratory data for scalar exchange across sheared gas-liquid interfaces [8]. The second part of the paper will present selected new LEIS results (Large Eddy Interface Simulation) of breaking waves, where large scales of turbulence and interface dynamics are resolved on the supergrid level.

2 Turbulent Interfacial Flows

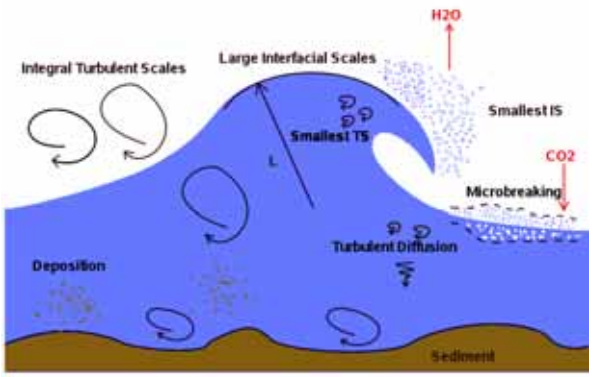

Figure 1: *An idealized wave representation.*

Interfacial flows refer to two-phase flow problems involving two or more immiscible fluids separated by sharp interfaces which evolve in time. Typically, when the fluid on one side of the interface is a gas that exerts shear (tangential) stress upon the interface, the latter is referred to as a free surface. What differs mixed or bubbly flows from the interfacial and/or dispersed flow is the rate of variation in space of the interface topology, defined here as interfacial scales (IS), with a spectrum ranging from sea wave amplitude to bubble or droplet diameter. Turbulence is rather specific to each phase, although its creation or dissipation is partly due to the way IS interact with each other. But this is another more complicated facet of the problem beyond the scope of work here.

To set the stage for what follows and pose the development of numerical and modelling techniques on solid grounds we first need to clarify the notion of segregation of scales in multiphase flow. We proceed by analyzing the canonical wave breaking problem depicted in Figure 1, which involves a hierarchy of length scales. Further, we need to look at the flow as a combination of turbulence scales (TS) acting in tandem with the interfacial scales defined previously. As to the flow dynamics, the wave develops by the action of pressure and wind-shear by extracting kinetic energy from the mean flow; it ultimately breaks into small scales and dissipates its energy. The whitecap or a micro-breaking layer, where the flu-

ids are hardly distinguishable, forms subsequent to wave plunging across depth. Turbulence is generated in some specific flow portions, i.e. on both sides of the sheared surface, at the sea bottom created by friction, and subsequent to jet plunging. The spectrum of turbulence varies drastically depending on the imposed wind conditions and sea depth: very large or integral scales are formed on top by the actions of air entrainment with the waves, whereas smaller ones evolve at the crest of the wave, near breaking, and mostly within the whitecap layer. The core liquid is also turbulent, featuring upwelling motions from below. Sea-spray droplets created by wave plunging disperse and deposit in response to the air-side turbulence. The picture is complete; it needs now to be translated in terms of modeling principles.

3 Air-Sea Mass Transfer Modelling

Estimates of the rate of interfacial mass transfer for gas-liquid processes have mainly been based on measurements and semi-empirical analysis [10, 11, 12, 13]. Scale-up was costly and often unreliable. The advent of powerful and affordable computational resources has helped clarify new fundamental issues, but the extremely fine resolution necessary to directly resolve interfacial transfer forces the modeler to resort to empirical parameterizations, as discussed next.

3.1 Surface Renewal Models

Early work on gas-liquid transfer modelling by [14] and [15] proposed that transport expressed in terms mass or heat transfer coefficients, β (sometimes denoted by K in the literature, and also sometimes in this article) is proportional to the liquid diffusivity, D, raised to some power, i.e., $\beta \propto D^n$. The theory speculates that turbulence brought fluid from the bulk to the interface, where unsteady absorption occurred into an essentially laminar fluid for some period, τ, after which the surface element was replenished. Subsequently, [15] allowed for a random distribution of surface ages for the renewed elements, which was more typical of what might be expected from a turbulent fluid, giving on the liquid side, thus translating τ as the mean time between surface renewals. The various subsequent models differed in the way the exponent "n" and the time between renewals τ should be specified. A number of researchers proposed various models for τ in the 1960s, notably the "large-eddy model" of [16] and the "small-eddy model" of [17], denoted hereinafter by LE and SE models, respectively. The LE model gave $\tau \approx \Lambda/u$ leading to a mass transfer coefficient

$$\beta\ Sc^{1/2} = u\ Re_t^{-1/2} \tag{1}$$

where Λ is the turbulence integral length scale and u is the integral velocity scale, and $Re_t = u\Lambda/\nu$ is the turbulent Reynolds number. On the other hand, the small-eddy (SE) model of [17] gave $\tau \approx (v/\varepsilon)^{1/2}$, where ε is the turbulent energy dissipation rate close to the interface, which can be either measured or calculated, e.g. $\varepsilon \approx u^3/\Lambda$, and thus

$$\beta\ Sc^{1/2} = u\ Re_t^{-1/4} \tag{2}$$

There is some ambiguity in how to define the turbulent Reynolds numbers in (1) and (2). Strictly speaking, ε is the dissipation rate near the interface, and it is better to use estimates of ε directly. Both models agreed with limited sets of data, but gave very different results when it came to predictions of transfer rate under the same conditions. Theofanous [18] resolved this discrepancy by showing that the large- and small-eddy models gave the asymptotic behavior of the transfer coefficient at small and large turbulent Reynolds numbers Re_t, respectively. For environmental systems, as Reynolds numbers in the field are variable, but often quite high, the SE model and the surface divergence (SD) model (see the next subsection) are appropriate, and many experiments are directed towards finding the near surface energy dissipation rate, ε.

3.2 Surface Divergence Models

The expression of [19] for the mass transfer coefficient for the case where there is no gas shear at the interface and the far-field turbulence is homogeneous and isotropic was based on the blocking theory of [20]. Using a result from [21], Banerjee [19] showed that for unsheared interfaces at which high Sc gas transfer occurs, the mass transfer rate β scales with the surface divergence field, or the divergence of the 2D velocity vector tangential to the interface, due to the fluctuating motions: $(\nabla\cdot\mathbf{u}'_{tang})_{int}$, where the subscript "$int$" denotes the interface. Physically, this is the signature of surface convergence/divergence and renewal caused by turbulence events that bring bulk fluid to the interface, known as "sweeps".

In our recent contribution to this subject [7], we have unexpectedly found the SD model to also apply for the scalar transport parametrization at sheared interfaces, although it was primarily thought for isotropic, homogeneous turbulence conditions and non-sheared interfaces. In the modified form of the SD model (where we have included an extra source term reflecting the surface curvature $\nabla\cdot\mathbf{n}$), the interfacial mass transfer reads [7]:

$$\frac{\beta\ Sc^{1/2}}{U_\infty\ Re_t^{-1/2}} = C\ \left[\left(\nabla\cdot\mathbf{u}'_{tang} - 2\ w'\ \nabla\cdot\mathbf{n}\right)^2\right]_{int}^{1/4} \tag{3}$$

where C is a model constant of the order of unity, and the quantity between square brackets is the square of the surface divergence field tangential to the interface (known as the dilation term). The RHS term is normalized using the integral velocity and length scales of the far field turbulence. The above form requires a closure for the RHS term. This has been intuitively made based on the Hunt-Graham blocking theory [19], and validated against the DNS data [7], as shown in Figure 2:

$$\frac{\beta\ Sc^{1/2}}{U_\infty\ Re_t^{-1/2}} = C\ \left[0.3\left(2.83Re_t^{3/4} - 2.14Re_t^{2/3}\right)\right]^{1/4} \tag{4}$$

Note in particular that in estimating the integral velocity scale Λ appearing in the definition of the turbulence Reynolds number, use was made of expression $\varepsilon \approx u^3/\Lambda$, where ε is the turbulent energy dissipation rate in the bulk flow. The comparison between the DNS and the blocking-theory based model shows very good agreement between the two quantities.

A free interface, however, is mobile and can deform in response to motions on the liquid side. The surface divergence with a deformable interface may be expected to be less, suggesting that the proportionality constant may be less than unity.

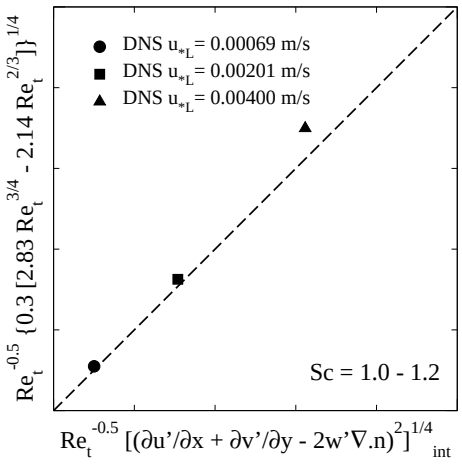

Figure 2: *Comparison of the surface divergence term with the Hunt-Graham blocking theory.*

These models were compared with the DNS data of [4], [6], and [7], showing overall an excellent agreement, with the SD model in particular. To complete the validation of the SD model, the UCSB group [8] has recently compared it with experimental data for higher interfacial shear values. The agreement was also found good. Altogether the SD model appears now to be a well established and reliable theory for mass transfer across unsheared and sheared gas-liquid interfaces.

4 DNS of Sheared Air-Sea Surface

Briefly, the flow which has been extensively studied by the UCSB group [4, 9] then the ETH Zurich group [5, 6, 7] involves turbulent air and water streams flowing in opposite directions at the same shear Reynolds number, $Re_\star = u_\star 2h/\nu = 171$. The flow quantities normalized by the inner variables, namely the shear velocity $u_\star = \sqrt{\tau_{int}/\rho}$, where τ_{int} represents the shear stress at the interface, the half-depth of each computational domain h, and the kinematic viscosity ν. The flow in each sub-domain is driven by a constant pressure gradient Π, such that $u_\star = \sqrt{2h\Pi/\rho}$. The sheared interface is allowed to deform in space and time by solving a convection equation for the surface elevation. When the interface is flat the interfacial shear balances the imposed mean pressure gradient. As the interfacial waves start to develop, part of the energy is transferred into form drag leading to a reduction of the interfacial shear. In these references the waves fall within the gravity-capillary range, with waveslopes $ak = 0.01 - 0.12$ (wave amplitude a times wavenumber k).

As these simulations proved useful in clarifying aspects of turbulence structure near deformable (nonbreaking) air–water interfaces, they have been extended to studies of scalar exchange by [4] for high Sc numbers up to Sc=200, and recently by [6] for low-to-moderate Schmidt numbers up to Sc=10. The results presented in this section are extracted from this last investigation and, when indicated, from [4].

5 Scalar Exchange Parameterizations

5.1 Surface Renewal model comparisons

For situations in which waves deform and break infrequently the modifications to the mass transfer scaling require clarification. In such cases the main near-interfacial turbulence structures are found to scale with the frictional drag D_f at the interface [4]. The appropriate velocity scale is then $u^*_{frict} \sim (D_f/\rho)^{1/2}$, where ρ is the fluid density. Both the surface divergence and the time between renewals, τ, are expected to scale with u^*_{frict} and ν. Looking at the liquid side, if the time between sweeps is taken as the time between renewals, then the DNS of [4] and [6] indicate that this scales as $\tau \sim 30-90\,(\nu/u^{*2}_{frict})$, which by virtue of the Danckwerts theory for mobile interfaces leads to, with subscript 'L' denoting the liquid side,

$$\beta_L\, Sc_L^{0.5}/u^*_{frict,L} \;\sim\; 0.108 - 0.158 \qquad (5)$$

Banerjee [19] showed that expression (5) agrees with the lab-scale data available at that time and de Angelis [4] found agreement with wind-wave tank data taken subsequently. It is of interest to see how Eq. (5) compares with the simulations. The Prandtl or Schmidt number dependencies in Eq. (5) are compared with simulation results for different Schmidt numbers in Figure (3). The data presented in this figure were obtained by Lakehal et al. [6] for $1 < Sc < 10$; they were found to corroborate with the earlier data of [4] for Schmidt numbers up to 200.

It is clear that the Schmidt number dependence is correctly predicted at high Schmidt numbers, but there is some deviation at low Schmidt numbers. Also, the numerical value of the RHS of the equations is roughly correct, but for $Sc > 5$ only; for values < 5, the Figure shows its value to be actually smaller (0.083), for different shear velocities - the smallest value corresponds to the case where the interface is almost flat. Equation (5) has also been compared with gas-wave tank data for SF6 and CO_2 transfer rates from Wanninkhof and Blivens by [7, 4]. The agreement was quite good, though the prediction always lies somewhat below the data. This could be due to a small effect related to turbulence from the channel bottom reaching the interface, which enhances the local turbulence.

Turning now to the gas side which perceives the liquid much like a solid surface, as discussed earlier, and in more detail by [5]. So, the surface renewal theory has to be modified somewhat for such applications, as in Eq. (5). This also leads to a different dependence on the Schmidt number. For a solid (as is essentially the case for the gas-side) surface, the form of the parameterization changes as turbulence is more strongly damped with $w' \sim z^2$ (where z is the distance from the surface). The DNS of de Angelis at high Sc revealed the scaling below

$$\beta_G\, Sc_G^{2/3}/u^*_{frict,G} \;\sim\; 0.07 \qquad (6)$$

where the subscript 'G' denotes the gas side. At low Sc, however, the data of [6] shown in Figure (3) suggest that the scalar transfer coefficient scales rather with $Sc^{-5/3}$, lying somewhat between the $Sc^{-1/2}$ dependence for free surfaces, and with $Sc^{-2/3}$ for immobile surfaces and much higher Sc numbers,

$$\beta_G\, Sc_G^{5/3}/u^*_{frict,G} \;\sim\; 0.058 \qquad (7)$$

Note that u^*_{frict} is based on the frictional drag component, which is the total drag only if the surface is level. With interfacial roughness due to waves, the total or effective drag includes form drag.

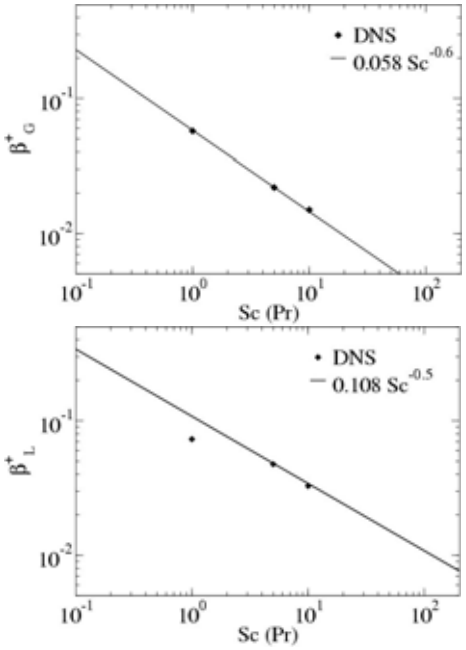

Figure 3: *The scaling of the gas- and liquid-side mass transfer velocities versus Sc using the SR model, Eqs. 5 (a) and 7 (b), for $u_{\star_L}$=0.001 m/s.*

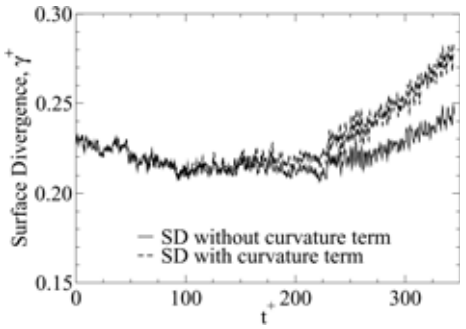

Figure 4: *Time evolution of the dilation term γ, with and without curvature.*

5.2 Surface Divergence Model Comparisons

Before comparing the results of the new simulations with the surface divergence models, we first examine the surface divergence term γ^+ (the RHS term in brackets in Eq. 3) with and without curvature contribution for $u_{\star_L}$=0.002013 m/s. The time history of the dilation term γ^+ is plotted in Figure (4). The curvature-source term is clearly shown to play an important role in estimating γ^+, and should therefore be taken into account for sheared surfaces.

Turning now to the scalar exchange parameterization, we consider the case where gas stress is imposed on the liquid interface, which is the context of the DNS studies discussed here. In these circumstances, the parameterization of the scalar exchange should be first examined with reference to Eq. (4). The Schmidt number dependencies in Eq. (4) are compared with simulation results for different values of Sc and for $u_{\star_L}$=0.002013 m/s in Figure (5). The best fit to the DNS data is obtained with the proportionality constant $C \approx 0.45$. It is clear that the dependence is well predicted up to Sc=200, but there is some deviation at $Sc = 1$. In Figure (6) the DNS results of the liquid-side mass transfer coefficient are compared with the SD model (4) for $Sc = 1.0 - 1.2$. The value of the constant $C \approx 0.35$ fits the SD model to the DNS results for various shear velocities quite well. Here the surface divergence is calculated from the DNS directly. This result is in conformity with what has been speculated before: for $Sc \approx 1$ the proportionality coefficient C in Eq. (4) should be somewhat lower. A similar trend has already been observed by [4] (and confirmed by the present DNS simulations) in their parametrization of the scalar transfer by reference to the SE model, i.e. $\beta^+ \approx 0.108 Sc^{-1/2}$, as also shown in Figure (5). It is evident now that in sheared interface situations, both the SE and SD models (using inner-variables scalings) predict the gas transfer rate less accurately for $Sc \approx 1$ than for higher Sc.

The model was also found to work well employing the far-field turbulent Reynolds number for prediction, albeit the turbulence is actually generated in the near-interface region. The Schmidt number dependencies in both equations were compared with simulation results for Schmidt numbers up to 10, and the agreement was as good as with employing the inner variables as scaling parameters for prediction. The Sc dependence of the dimensional liquid-side mass transfer coefficient can be well predicted using far-field turbulence by both equations only with the proportionality coefficient set equal to $C = 0.35$.

It is understandable that from an engineering point of view, the surface divergence term γ^+ cannot be easily determined; the alternative approximation to it is expression (4) using the far-field turbulence quantities, i.e. Re_t.

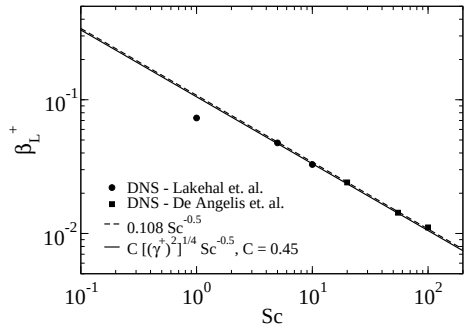

Figure 5: *The scaling of the liquid-side mass transfer velocity (normalized by inner variables) with Sc using the SE model ($\beta^+ \approx 0.108 Sc^{-0.5}$) and SD model with $C = 0.45$, for $u_{\star_L}$=0.002013 m/s.*

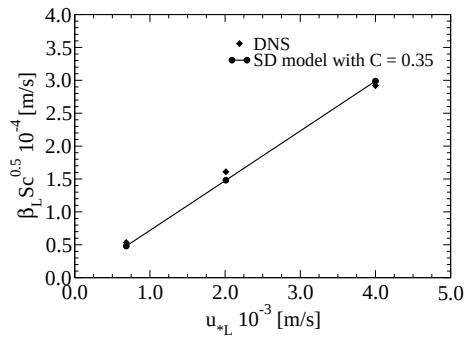

Figure 6: *Dimensional mass transfer velocity versus frictional velocity for $Sc = 1.0-1.2$. The SD model is clearly seen to fit the DNS data with $C = 0.35$.*

6 The Large-Eddy & Interface Simulation Concept: LEIS

For higher Reynolds number flows, the resort to LES is understandably necessary. The combination of LES with the one-fluid formulations for interface tracking should help predict large-scale physics in the fluids down to the grid-resolved level of wave problems. The combination is termed LEIS, short for Large Eddy & Interface Simulation. The idea consists of grid-filtering each phase separately; the resulting sub-grid scale (SGS) stresses are modelled as if they were isolated. Special treatment may be necessary at the interface though, taking advantage of the fact that the lighter phase perceives the interfaces like deformable walls [5]. In LES, the grid size is related to the smallest resolvable eddy length scale (TS) on each side of the interface. In ITM the smallest IS that can be captured on a given grid is of the order of the grid cell; slightly larger with the Level Set than with VOF for instance. The combination of the two brings a notable difference, that is: besides delivering the time-dependent interfacial kinematics (and provided the method could achieve sufficient resolution for the boundary layers at the interfaces), the need to model the interfacial exchange terms in the two-fluid phase conservation equations is eliminated. For the time being this is limited to interfacial flows defined above, and will remain not feasible for dispersed gas-liquid flows; the effort needed to track all interfaces and compute accurately the gradients at the interfaces in, say, bubbly flow would have been prohibitive.

The grid-scale description of immiscible Newtonian two-fluid flow is also based on filtering the subgrid-scale motions (f') out of the true flow field (f) using a convolution product. Specifically for Volume-of-Fluid methods, the phase indicator function $C(\mathbf{x},\mathbf{t})$ is equal to unity if point $\mathbf{x}$ is occupied by phase k=G and zero otherwise; once filtered, this quantity yields the resolved volume fraction:

$$\overline{C}(x,t) \equiv \int_D G(\mathbf{x}-\mathbf{x}')C(\mathbf{x}',t)d\mathbf{x}' \ , \qquad (8)$$

The derivation of the filtered one-fluid equations is based on the use of the component-weighted volume averaging (CWVA) procedure [24] employed for the LES of turbulent bubbly flows. In the context of the interface tracking-based single-fluid formalism, CWVA reduces to Favre averaging, i.e. $\widetilde{f}(\mathbf{x},t) = \overline{\rho\, f(\mathbf{x},t)}/\overline{\rho}$, where $\overline{\rho} \equiv \sum_k \overline{C^k(\mathbf{x},t)\rho^k}$. Detailed derivation of the filtered single-fluid conservation equations is provided in [22, 23]. The filtered LEIS equations are very similar to the filtered compressible flow LES equations, but do include a resolved surface tension term $F_s = \overline{\sigma\kappa\,\hat{n}_i\delta_s}$ to account for interface momentum jump conditions, where σ is the surface tension coefficient, κ is the interfacial curvature, $\hat{n}_i$ is the unit interface normal, and δ_s is the surface delta function. The local (phase-specific) subgrid-scale tensor is defined as

$$\tau_{ij} \equiv \overline{\rho}\,(\widetilde{u_i u_j} - \widetilde{u}_i\widetilde{u}_j) \qquad (9)$$

Liovic and Lakehal [23] used *a-priori* evaluation of the important SGS terms in the filtered one-fluid equations and showed that for flows consisting of immiscible fluids of length scales larger than the grid size, the SGS stress term is at least $O(10^2)$ larger than the unresolved surface tension. Consequently, the LEIS approach only features explicit closure of the SGS stress term, using for example:

$$\nu_t \equiv f_{\mu\mathsf{int}}\,(C_s\,\overline{\Delta})^2\sqrt{2\widetilde{S}_{ij}\widetilde{S}_{ij}} \qquad (10)$$

with the model coefficient set equal to $C_S = 0.1$ in the core flow, which is the average value obtained using the Dynamics model of Germano [24] for a two-phase flow shear-layer.

In the presence of shear – either near the wall or in the vicinity of deformable surfaces where the viscous sublayer is well resolved – eddy viscosity models generally need to incorporate a damping function (f_μ) in order to accommodate the near-wall/interface limiting behavior in low-Re number flow conditions. Similar 'corrections' need to be introduced when eddy viscosity models are employed for interfacial two-phase flows, where the lighter phase perceives the surface like a rigid wall [5]. A systematic LES study of the [5] flow performed by [25] has shown that without such modification, the Smagorinski model alone becomes excessively dissipative, just as it tends to be for wall-bounded flows. For low to moderate interface deformations the DNS database of [5] provided an exponential dependence of $f_{\mu\mathsf{int}}$ on the distance to the interface y^+_{int} from the gas side:

$$f_{\mu\mathsf{int}} = 1 - \exp\left(a\,y^+_{\mathsf{int}} + b\,(y^+_{\mathsf{Int}})^2 + c\,(y^+_{\mathsf{Int}})^3\right) \ , \qquad (11)$$

where a, b and c are model coefficients.

Analogous to the concept of a "wall units" length scale (y^+), damping of eddy viscosity in SGS modelling at sheared interfaces requires the introduction of its own length scale measure, denoted here by the "interface turbulence units" y^+_{int}. In [23] the authors introduced and validated the algorithm for extracting the elements necessary for estimating y^+_{int} from the flow field, namely the interfacial friction velocity $U_{\tau\mathsf{Int}}$, and the reconstructed distance function (RDF) ϕ^{RDF} defined by:

$$y^+_{\mathsf{Int}} = U^\tau_{\mathsf{Int}}\phi^{\mathsf{RDF}}/\nu; \qquad U^\tau_{\mathsf{Int}} = \sqrt{\tau_{\mathsf{Int}}/\rho}\ . \qquad (12)$$

7 LEIS of Steep Water Waves

7.1 Problem set-up and simulation strategy

Work on this topic is detailed in [26, 27]. In this problem a constant bed slope $\alpha = 4.8^0$ is assumed, in which case simulation using a Cartesian mesh and off-vertical gravity contributions is ideal. In this study, the streamwise breadth of $X = 8.0m$ is resolved by 240 cells, the spanwise breadth of $Z = 0.6m$ is resolved by 80 cells, and the crossflow breadth of $Y = 0.3m$ is resolved by 40 cells. A preliminary coarse-grid resolution of $140\times40\times20$ was not sufficient to resolve the interface viscous sublayers, such that the details of the interface wrinkling were smoothed out. The fine grid resolution helped resolve both the wall (channel bed) and air-side interface viscous sublayers down to $y^+_{\mathsf{Wall}} \approx y^+_{\mathsf{Int}} \approx 0.1$.

The fifth-order Stokes theory of Fenton [28] is the basis of the free surface initialization and boundary conditions used here. The low is initially at rest, developing subsequently under gravity and the loading imposed by the wave generator. Once the potential energy of the liquid is transformed into kinetic energy, the actual Reynolds number should, over time, adapt accordingly. The fluctuating turbulent field initially imposed was generated using a Gaussian distribution with zero mean and a standard deviation of $\sigma_u = \sqrt{g\,d\,sin(\alpha)}$. After solutions representative of the fully-developed flow were obtained, the shear Reynolds number was found to converge in both phases towards $Re^\tau_{Int} \approx 400$, where U^τ_{Int} is the friction velocity (equally applicable from both sides of the interface).

The offshore boundary is prescribed as a fixed flow condition, with velocities determined as partial derivatives of the field potential based on the prescription of Fenton [28] The velocity distribution of air entering the solution domain at the offshore boundary is initialized to share the velocity of the water at the free surface level, thus minimizing shear at the interface/offshore-boundary junction. This initialization presumes the water-sided wave generator to be responsible for near-surface currents on the air side of the free surface. Imposing wind to modify the wave breaking phenomena is avoided. The onshore boundary is treated as an open boundary condition to ensure global mass conservation. The bed is represented using no-slip boundary conditions. The higher resolution has indeed resulted in low-Re number resolution sufficient to avoid resorting to wall functions. Periodicity condition was applied to the boundaries normal to the longshore direction.

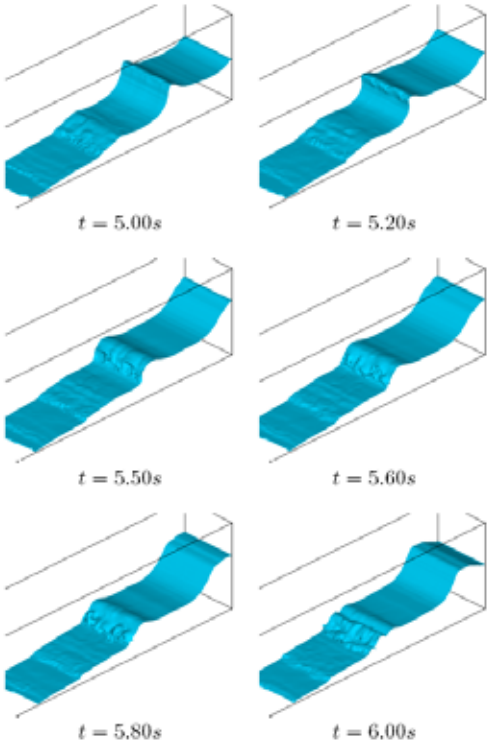

Figure 7: *Wave breaking events.*

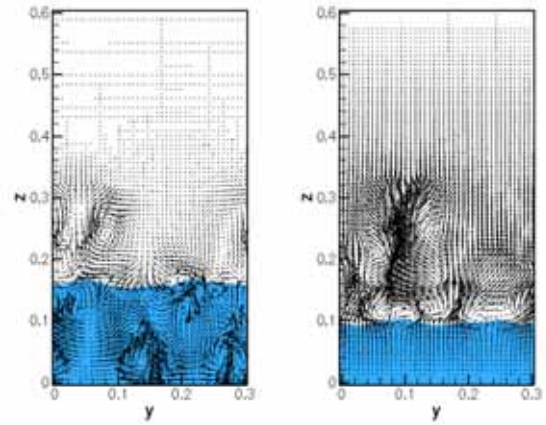

Figure 8: *Cross-flow secondary velocity field and surface deformations.*

7.2 Wave breaking events and flow structure

Snapshots during breaking events show characteristics of both spilling and plunging breakers, and in general is still best described as "weak plunging". During start-up, the front face of the wave becomes vertical and the top of the wave turns over, indicative of plunging events. However, the jet thrown forward from the top of the front face doesn't feature significant momentum; the jet collapses to resemble spilling of a crest down the front of a wave, and no significant pipeline is formed. Later on in the fully-developed flow (as shown in the sequence of snapshots in Figure 7), there is a clear large-scale turning over of the wave, a more noticeable pipeline, and entrainment of air below the free surface – all features of plunging rather than spilling. The plunging event is weak, in that: (i) the jet is not thrown forward far enough to form a pipeline of substantial radius; (ii) splash-up forward of the impact point does not rise to a substantial fraction of the wave height.

The flow field structure generated by the simulation is analyzed of Figure 8, illustrating the secondary velocity field at various y-z cross sections through the flow. The velocity field is superimposed on the free surface marker, which is seen to respond to vortical structures. The formation of longitudinal vortices at the channel bed and on both sides of the interface is visible in the left panel, corresponding to a pre-breaking scenario. Turbulence is fully developed along the channel, but it is most intense in this first cross flow location. Typical scales of the generated eddies compare with depth d of half the bath , and are about 1/4 to 1/5 the width of the domain. The figure reveals vigorous downwelling and upwelling patterns developing with the breaker. The impact of these flow events on the surface can be observed as well. Prior to breaking, turbulence was found to obey the -3 decay law, afterwards it changed to a -5/3 slope in the inner and outer surfs.

7.3 Mean flow results

We proceed in this section by extracting information about the transport in the mean flow, including the exchange of energy between the waves and the mean flow, and vice-versa. The flow is decomposed into mean flow and unstable wave modes. Data generated after this threshold ($\widetilde{\varphi}$) were first averaged spatially in the spanwise lateral direction (denoted by the symbol $<\varphi>$), then over time to yield $\overline{<\varphi>}$. Note that for simplicity we will omit the tilde symbol from the notations below. The difference between the spanwise average and the time average of the spanwise average velocity $u_i" \equiv \overline{<u_i>} - <u_i>$ is designed to estimate the wave velocity, containing both the unstable modal velocity and small-scale fluctuations superposed on it; i.e. $u_i" = u_i^m + u'$. The stresses discussed next relate to the wave-induced motion. To distinguish between modal- and turbulence-induced energies, use should be made of ensemble averaging over distinct realization: this is possible in experimental studies, but rather elusive with LES and DNS.

Figure 9 presents the distribution of the averaged phase velocities and modal energy stresses. Time averages were generated over four wave periods, which is probably short for the purpose of generating ergodic flow statistics, but these were neither intended for the purpose of detailed comparison nor for the validation of the numerical method; details of this are provided in the accompanying paper [23].

The averaged cross-flow velocities are one order of magnitude weaker than in the streamwise direction, but

indicate that the entrained airflow is dominated by vortical structures along the spanwise extension. In this breaking zone the wave flow field is clearly dominated by streamwise stresses, with the intensity of the distribution clearly shown to feature a dependence on interface proximity. The intensity of vertical and spanwise stresses marks the location of the core of the jet region is. But again, cross-flow stresses are shown to dominate over the spanwise components and to contribute as much as 50% to the unstable wave field. In the shoaling and breaking zones the water-sided fluctuations in the spanwise velocity component, $\sqrt{\overline{v"v"}}$, are smaller further away from shore. The source of wave induced fluctuations in the air is shown to be located closer to shore, suggesting that the transition from wave steepening to wave breaking is the precursor feature for wave-induced fluctuations generation in the airflow.

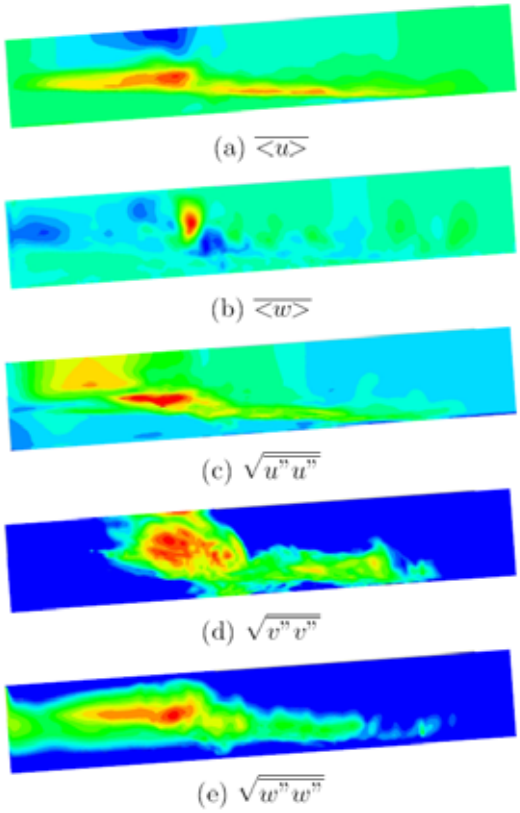

Figure 9: *Mean and RMS axial velocity distributions.*

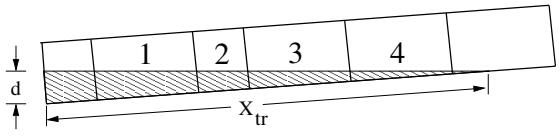

Figure 10: *Flow decomposition: Zone 1= Shoaling; 2 = Breaking; 3 = Outer surf; 4 = Inner surf.*

7.4 Zonal conditional analysis

Visual assessment of the breaking events suggests a natural delineation of the flow into regions featuring different flow characteristics. Figure 10 shows the delineation of zones adopted in the current study (scaled relative to the quiescent free surface representation). Each zone features specific transport processes taking place repeatedly at specific instants, while the nature of the transport processes may differ significantly between zones. Indeed, unlike in most single-phase flows amenable to LES, the present context requires the identification of specific events, not necessarily periodic or homogeneous as would be required, for example, in triple flow decomposition for flows dominated by coherent structures.

Zone 1 is the shoaling/deformation zone furthest offshore, located at $8.9 \geq \eta \geq 12.0$ from the quiescent shoreline location, where η is defined by $\eta = (X_{tr} - x)/d_0$, where $X_{tr} = 4.35m$ is the shore location of the sea under quiescent conditions relative to the origin (offshore boundary) of the computational flow domain, and x is the streamwise coordinate relative to the origin. The zone is characterized by low wave slope and high Froude number. Zone 2 is the main breaking zone lying in the interval $7.3 \geq \eta \geq 8.9$ from the shoreline and is characterized by high wave slope and maximal wave crest height. The Froude number here is slightly smaller than in Zone 1. Zone 3 is the outer surf zone located in the region $4.2 \geq \eta \geq 7.3$ from the shoreline and is characterized by the post-breaking aftermath. Zone 4 is the inner surf zone located at $1.1 \geq \eta \geq 4.2$ from the shoreline and is adjacent to the swash zone (which includes the shoreline). This latter flow area is characterized by a low Froude number, too. The analysis focuss here on each of these zones separately. The analysis presented next deals with the most pertinent flow features associated with breaking and micro-breaking, which are essential for mass transfer modelling, since this is directly related to interfacial area evolution.

7.5 Interfacial area and microbreaking

A notable feature of the breaking events shown in Figure 7 is the formation of small-scale surface deformations perpendicular to the spanwise direction. This process may be referred to as surface "micro-breaking" if it is accentuated and uncorrelated with the dominant 2D wave propagation and wave breaking. Micro-breaking is the first visible evidence of three-dimensionality in flows driven by nominally two-dimensional waves. Jaggedness of the wave crest and curvature in the longshore direction of the flow are ubiquitous features of breaking waves. Flow models featuring simplistic representations of the interface kinematics of wave breaking cannot capture micro breaking. The causes of micro-breaking, and more particularly its implication for turbulent processes in the flow are treated in [27].

Identifying surface wrinkling as a precursor that may lead to micro-breaking, a modified version of the measure introduced by Geurts [29] is used here to quantify surface wrinkling in a nondimensional manner:

$$W = \frac{L_0 + 2H_0}{L_0 H_0} \frac{\int_S |\kappa| dS}{\int_{Sflat} dS}. \qquad (13)$$

In this expression $\int_{Sflat} dS$ is the interfacial area of a smooth free surface parallel to the sea bed (denoted by A_0) and is introduced to make the wrinkling measure independent of quadrant size. The parameter $(L_0 + 2H_0)/(L_0 H_0)$ is introduced to scale the wrinkling measure with the curvature of the underlying 2D wave; it was set equal to ≈ 9.24 at the initialization of the wave. Two measures of wrinkling are generated: (i) W^{3D}, based on the free surface of the fully 3D flow; (ii) W^{2D}, based on the free surface locus of the spanwise-averaged flow field. If W^{2D} is interpreted as the wrinkling associated with the underlying 2D wave-form, then

the difference between W^{3D} and W^{2D} emphasizes the existence of surface deformations that may "subjectively" be classified as micro-breaking. Finally, the interfacial area A scaled with A_0 has also been determined for comparison with W:

$$A = \frac{\int_S dS}{\int_{Sflat} dS}. \tag{14}$$

While wrinkling measures W^{3D} and W^{2D} are specifically dedicated to measuring grid-scale interface deformations, the interfacial area A contains both small- and large-scale surface deformations, and as such it does not delineate three-dimensional free surface micro-breaking from the wave deformation in two dimensions. Surface deformations may be classified as micro-breaking if the normalized interfacial area A/A_0 is somewhat larger than unity, but this is not clear yet. Figure 11, illustrating the time evolution of W and A/A_0, helps distinguish nearshore from offshore flow zones. The periodicity is clearly seen to take place in Zone 1 only, the area populated by the low-frequency wave-wave interaction.

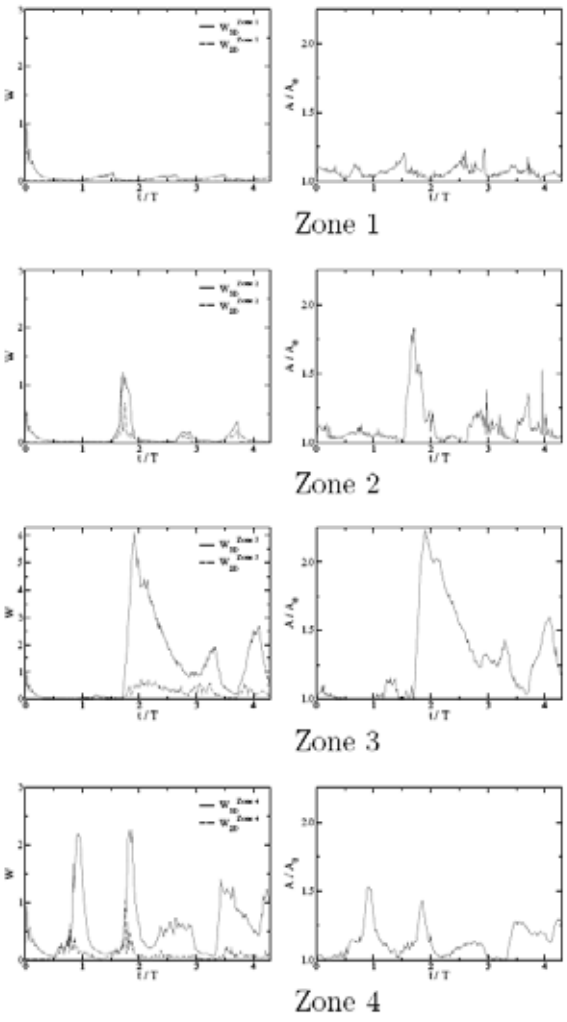

Figure 11: *Surface wrinkling (2D and 3D) and interfacial area evolution in each flow zone.*

The left panels of Figure 11 comparing two- and three-dimensional wrinkling show that the free surface in zone 1 generally features low curvature, with occasional crests in the wrinkling signal coinciding with wave crest steepening as zone 2 is approached. There is little difference between the 2D and 3D wrinkling signals. [The appearance of micro-breaking wrinkles at the start is due to the white-noise perturbation imposed on the initial flow field, rather than a result of the mean flow evolution.]

Negligible wrinkling generally prevails in zone 2, with the exception of the breaking event during which surface deformations are systematically accompanied by three-dimensional micro breaking. The occasional surface deformations observed in this zone coincide with the immediate pre-breaking event, where the wave saturates before plunging. Peak values in the wrinkling measure for zone 2 in Figure 11 correspond to the type of free surface configuration shown in the first panel of Zone 2 (c.f. Figure 10). According to the signals taken in this zone, 2D wrinkling dominates the overall surface deformations and is associated with the jet being thrown forward of the crest during wave breaking, when air bubbles are trapped underneath the jet and entrained underneath the free surface. The micro-breaking contribution during wave plunging in this zone is seen to take the form of a longshore instability in the jet.

Following start-up, the Zone 3 panel of Figure 11 shows sustained and significant high frequency topology deformations. The event resulting in the most concentrated interface wrinkling coincides with the collision of backwash water from the inner surf Zone 4 with the jet and splash water thrown towards shore from the aftermath of plunger breaking. The time signal shows W^{2D} at maximum wrinkling to be relatively insignificant, suggesting the wrinkling to be dominated by micro-breaking. Subsequent troughs in the W^{3D} signal show that interface smoothness in zone 3 is periodically regained between periods of significant wrinkling, as shown in the zone 3 snapshots of Figure 10.

Surface deformations in zone 4 are also shown to be dominated by micro-breaking. The backwash of water can again be seen to contribute significantly to micro breaking. Wrinkles also propagate into zone 4 from the outer surf Zone 3. Beyond a superficial description of wrinkling in the wave-breaking flow, W^{3D}, W^{2D} and A at this stage do not answer the important open questions regarding interface wrinkling. These questions include the manner in which micro-breaking occurs in surf zones featuring wave breaking and backwash, and the relative importance of wrinkle dissipation and propagation in re-establishing smoothness in wrinkled nearshore zones.

8 Concluding Remarks

The contribution highlights the progress achieved in simulating turbulent air-sea flows using DNS and LES, with support from experiments. State-of-the-art prediction methods were not introduced in the detail. Emphasis was rather placed on flow-physics prediction based on direct and large eddy & interface simulations. The DNS and experiments have permitted to establish the SD model as a reliable theory for mass transfer across sheared and unsheared interfaces. The LEIS is shown to be a possible route for exploring more plausible wave deformation scenarios under high Reynolds number flow conditions. In particular, the method was capable to delineate flow zones featuring the most vigourous surface wrinkling and microbreaking. More detailed results including kinetic energy production, dissipation, turbulence transport and enstrophy can be expected for the near future.

Acknowledgements

The collaboration with the UCSB group (Prof. S. Banerjee) on the first part of this work is acknowledged. Marco Fulgosi and Sylvain Reboux from the ETH group performed and analyzed the most recent DNS data of the sheared deformable interface. Petar Liovic (now at the University of Melbourne) has performed the LEIS simulations of wave breaking.

References

[1] http://ioc.unesco.org/iocweb/CO_2panel/

[2] Donelan M.A, Wanninkhof R.H, Gas Transfer at Water Surfaces - Concepts and Issues, *Gas Transfer at Water Surfaces, Geophisycal Monograph.* Donelan MA, Drennan WM, Saltzman ES, Wanninkhof RH (Eds.), Washington D.C.: American Geophysical Union; 2002.

[3] Banerjee S., MacIntyre S., The air–water interface: turbulence and scalar exchange. *Advances in Coastal Engineering*, 9, Grue J, Liu PF, Pedersen GK (Eds.), Word Scientific, 2004. Banerjee S, MacIntyre S.

[4] De Angelis V., Lombardi, P., Andreussi, P., Banerjee, S. Microphysiscs of scalar transfer at air–water interfaces. in Proc. *Wind-Over-Wave Couplings: Perspectives and Prospects*, S. G. Sajjadi, N. H. Thomas, and J. C. R. Hunt (Eds.), Oxford University Press, 257, 1999.

[5] Fulgosi, M., Lakehal, D., Banerjee, S., De Angelis, V., Direct numerical simulation of turbulence in a sheared air–water flow with deformable interface. *J. Fluid Mech.*, vol. 482, pp. 310-332, 2003.

[6] Lakehal D., Fulgosi M., Yadigaroglu G., Banerjee S., Direct numerical simulation of turbulent heat transfer across a mobile, sheared gas-liquid interface. *J. Heat Transfer*, vol. 125, pp. 1129-1142, 2003.

[7] Banerjee S., Lakehal D., Fulgosi M.: Surface divergence models for scalar exchange between turbulent streams, *J. Multiphase Flow*, vol. 30(8), pp. 965–979, 2004.

[8] Turney D.E, Banerjee S., Transport phenomena at interfaces between turbulent fluids, *AIChE Journal*, vol. 54 (2), pp. 344-349, 2008

[9] Lombardi P., V. DeAngelis and S. Banerjee, Direct numerical simulation of near-interface turbulence in coupled gas-liquid flow, *Phys. Fluids*, vol. 8, 1643, 1996.

[10] Chu, C. R., Jirka, G. H., Turbulent gas flux measurements below the air–water interface of a grid-stirred tank. Int. J. Heat and Mass Transfer, vol. 35, pp. 1957-1973, 1992.

[11] Brumley, B. H., Jirka, G. H., Near surface turbulence in a grid-stirred tank. J. Fluid Mech., vol. 183, pp. 235-252, 1987.

[12] Komori, S., Murakami, Y., Ueda, H., The relationship between surface renewal and bursting motions in an open channel flow. *J. Fluid Mech.*, vol. 203, pp. 103-120, 1989.

[13] Kumar, S., Gupta, R., Banerjee, S., 1998. An experimental investigation of the characteristics of free–surface turbulence in channel flow. *Phys. Fluids*, vol. 10(2), 437, 1998.

[14] Higbie, R., The rate of absorption of a pure gas into a still liquid during short time periods of exposure. *Trans. A.I.Ch.E.*, vol. 31, pp. 365-372, 1935.

[15] Danckwerts P. V., Significance of liquid–film coefficients in gas absorption. *Ind. Engng. Chem.*, 43, pp. 1460-1473, 1951.

[16] Fortescue G. E., Pearson J. R. A., On gas absorption into a turbulent liquid. *Chem. Engng. Sci.*, vol. 22, pp. 1163-1178, 1967.

[17] Banerjee S., Rhodes E., Scott D. S., Mass transfer to falling wavy liquid films in turbulent flow. *Ind. Engng. Chem. Fundam.*, vol. 7, pp. 22-30, 1968.

[18] Theofanous, T. G., Conceptual models for gas exchange. in *Gas Transfer at Water Surfaces*, pp. 271–281, W. Brutsaert and G. H. Jirka (Eds.), 1984.

[19] Banerjee S., Turbulence structure and transport mechanisms at interfaces. 9^{th} *Int. Heat Transfer Conference*, Jerusalem, 395, 1990.

[20] Hunt, J. C. R., Graham, J. M. R., Free stream turbulence near plane boundaries. *J. Fluid Mech.*, vol. 84, pp. 209-220, 1978.

[21] McCready, M. J., Vassilliadou, E., Hanratty, T. J., Computer simulation of turbulent mass transfer at a mobile interface. *AIChE Journal*, vol. 32, pp. 1108-1120, 1986.

[22] Liovic P., Lakehal D.: Interface-turbulence interactions in large–scale bubbling processes, *Int. J. Heat & Fluid Flow*, vol. 28, pp. 127Ű-144, 2007.

[23] Liovic P., Lakehal D.: Multi–physics treatment in the vicinity of arbitrarily deformable gasŰ-liquid interfaces, *J. Comp. Physics*, vol. 222, pp. 504-Ű535, 2007.

[24] Lakehal D., Smith B.L., Milelli M., Large-eddy simulation of bubbly turbulent shear flows. *Journal of Turbulence*, vol. 3(25), pp. 1–21, 2002.

[25] Reboux S., Sagaut P., Lakehal D., Large-Eddy Simulation of Sheared Interfacial Flow, *Phys. Fluids*, vol. 18(10), 105105-1-15, 2006.

[26] Lakehal D. and Liovic P., LES of Steep Water Waves. *In IUTAM Computational Approaches to Multiphase Flows*, A. Prosperetti and S. Balachandar (Eds.), Springer, Fluid Mechanics and its Applications, pp. 331-340, 2006.

[27] Lakehal D., Liovic P., Free surface dynamics in steep breaking waves, *J. Fluid Mech.*, (in review), 2008.

[28] Fenton J. D., A fifth-order Stokes theory for steady waves, *J. Waterw. Port Coastal Ocean Eng.*, vol. 111, pp. 216-234, 1985.

[29] Geurts B.J., Buoyant turbulent mixing in shear layers, in *Proc. 9th European Turbulence Conference*, I.P. Castro and P.E. Hancock (Eds.), CIMNE, Barcelona, 2002.

Large Eddy Simulations of Environmental Shallow Water Coastal Flows

Vincenzo Armenio and Federico Roman

Dipartimento di Ingegneria Civile e Ambientale, Universitá di Trieste, Italy.
armenio@dica.units.it

Abstract

In the present paper we discuss a LES methodology for large-scale, environmental problems. Specifically we discuss peculiar features of the model LES-COAST, developed by IE-*Fluids*, University of Trieste, for the Italian Agency of Environmental Protection (APAT). The model is suited for marine, complex-geometry, anisotropic problems, typically occuring in coastal engineering. Examples of application of the model are also discussed. Specifically we show some results of the simulation of the Tevere river runoff in the Tyrrhenian sea and of the three-dimensional transport and mixing in the Muggia Bay (Gulf of Trieste) under breeze forcing. The numerical model is presently used for research as well for consultant activity for the prediction of dispersion phenomena in shallow-water near-shore areas.

1 Introduction

A branch of fluid mechanics of growing interest is that devoted to the study of environmental problems. To be more precise, for environmental fluid mechanics (EFM) it is intended the study of fluid flows in surface water, ground water, the atmosphere, and engineered systems (e.g. wastewater treatment plants). The most fascinating and, at the same time, complex aspect of EFM is that knowledge of many disciplines is required; typically an EFM problem requires knowledge of classical fluid mechanics, civil engineering, large scale dynamics, meteorology, geophysical fluid mechanics, limnology, environmental engineering.

The main difference between the classical (industrial) fluid mechanics and EFM is the length scale over which the phenomenon develops. Typical EFM problems evolves over scales of 10^3 meters along the horizontal direction and 10^2, 10^3 meters along the vertical direction, respectively for water basin and atmospheric problems. Typical velocity scales U are of the order of 0.05 m/s for water dynamics (tides, currents) and of the order of 5 m/s for the low atmosphere. For a mid-latitude water basin we obtain a value of the Rossby number $Ro = U/fL$ of the order of 1, where $f = 2\Omega_H sin\theta$ is the Coriolis parameter Ω_H is the earth rotation frequency and θ the latitude. Conversely for the low atmosphere $Ro \sim 10^2$, much larger than the previous one. It is well known from literature that values of Ro much larger than one, make the effects of rotation negligible when compared to the inertial ones. On the other hand, when $Ro \sim 1$ the rotation may play a role in turbulent mixing within the water column (see among the others [5], [15] and [9]). Specifically it has been shown that the three components of rotation may re-distribute energy from the mean field to the fluctuating one, thus acting as production/destruction terms of the turbulent kinetic energy. The analysis of the typical velocity-scales and length-scales hence shows that rotation effect may be relevant in water basins analysis whereas it may be less relevant for the study of pollution dispersion in the low atmosphere.

A main difference between EFM and classical fluid mechanics is density stratification. As discussed before, in EFM the vertical length scale is always of the order of at least ten meters and vertical variation of temperature is likely to occur. In water basins, salinity (the concentration of dissolved salt in water) may also play a role and it may interact with temperature to produce thermo-halin effects in the fluid column. Humidity plays a similar role in the low atmosphere. Since the variation of density due to temperature and concentration is small, compared to the bulk density of the fluid columns, the governing equations can be simplified and the flow field can be assumed incompressible. The presence of stratification appears as a body force term (gravitational term) in the vertical component of the momentum equation. This is known in literature as Boussinesq approximation of the Navier-Stokes equations (for a detailed discussion see [8]). From a physical point of view, the buoyancy effects due to the change of density are retained, whereas the change of volume of the fluid due to the variation of concentration/temperature is neglected. At least three additional equations must be added to the system: two of them are the advection-diffusion equations of temperature and concentration; the third one is the state equation $\rho = \rho(T, C)$ which relates density to temperature and concentration (salinity in water and humidity in the atmosphere). Additional advection-diffusion equations must be also included in the system if one is interested to the analysis of the concentration of a dispersed phase in the flow field.

Numerical models are in use in practical engineering for the prediction of dispersion of, among the others, thermal/fresh water plumes in sea basins or lakes, plumes from smokestacks in the low atmosphere. Most of available models are based on very restrictive hypotheses and give a rough estimation of the characteristics of dispersion of the polluting agents. Since these models must be used by technicians with little fluid mechanics knowledge, the most important characteristics are the simplicity of use and the ability to supply an estimation of some relevant quantities (i.e. the concentration of some chemical agents) using a wide range of forcing parameters in a reasonable time.

For coastal applications, often two-dimensional models are used under the assumption of shallow water conditions. Obviously such models are not able to predict very important dynamics related to the effects of vertical stratification. Three dimensional models have been recently developed, solving the governing equations un-

der a very wide range of parameters and flow conditions. These softwares, designed to solve a wide class of problems, are composed of different modules and are designed to run on desktop stations. Most of these solvers are based on the solution of the Reynolds averaged Navier-Stokes equations, with turbulence models derived from the industrial experience. However it is not clear how models developed for well defined and controlled flows can be extended to a field where additional physical processes are present (rotation and stratification effects, strongly three-dimensional flows without any mean prevalent flow, ect.). For an overview on basic modeling in coastal ocean turbulence and mixing see Burchard et al., (2008).

On the other hand, over the last decades fundamental research has successfully analyzed problems archetypal of applicative processes, with the aim to understand physical mechanisms occurring in environmental flows. Such studies have been limited to problems characterized by simple geometry and boundary conditions (see, among the others, the study of internal waves induced by a bump in a stratified flow, [4] and [17]). Both direct numerical simulations and resolved large eddy simulations have been used for the analysis of fundamental problems, thus limiting the range of values of Reynolds number afforded.

As a consequence a gap exists between archetypal, high quality numerical simulations of environmental flows and simulations of real-life problems. The former usually require a large amount of CPU-time and noticeable pre and post-processing time. Due to these characteristics only few significant simulations can be carried out. The latter incorporate many physical/chemical processes, including chemical reactions, bacteria dynamics etc.. They do not require large cpu-time and allow the analysis of a wide range of physical conditions. The drawback of these practical engineering tools is that it is still not clear how to perform reliable validation tests based on comparison with available experimental data. Obviously due to the different topics of the two families of simulations, they are not in competition with each other, and the experience gained with the high quality models may be useful to upgrade and make more reliable numerical models for practical environmental fluid mechanics predictions.

The scope of the present note is to show an example of such strategy, carried out by IE-*Fluids*, (Industrial and Environmental Fluid Dynamics research group of the University of Trieste). Specifically over the last few years the resolved-LES numerical model used for fundamental studies of wall bounded turbulence [1] has been modified and adapted to the study of applicative problems of EFM. Specifically the model LES-COAST has been developed for coastal studies, and the model LES-AIR is being developing for studies of emission from chimneys in the low atmosphere. In the following section we briefly describe LES-COAST and some applications to real-life, coastal-hydrodynamics problems.

2 LES-COAST: a LES model for prediction of mixing in coastal areas

LES-COAST is a Large Eddy simulation solver properly suited for coastal applications. It has been recently developed for the Dept. of Protection of Internal and Marine Waters, of APAT, and it is currently in use for the analysis of applicative problems. The model solves the Boussinesq curvilinear-coordinates formulation of the filtered three-dimensional Navier-Stokes equations. The Boussinesq approximation applies for flow fields characterized by small variations of density $\Delta\rho/\rho_0 \sim O(10^{-2})$ (with ρ the density and ρ_0 a reference bulk density) and hence, density variations affect momentum transport and are negligible as regards volume variations. The model is able to treat density variations related both to the thermal field and to the salinity field.

A number of elements concur to determine mixing in coastal areas. Buoyancy phenomena occur in coastal problems, related to temperature and salinity differences between a river stream or in general an incoming jet and the water within the basin. Additionally, typical forcing terms are the wind breeze, tides and long-shore currents. Besides, usually coastal regions are characterized by geometry complexity, due to combination of the coast-line, the bathymetry and marine structures. The overall result is a fully three-dimensional flow field. Typical shallow water solvers, often used to predict mixing in coastal areas, cannot face most of the effects mentioned above. In particular they are not able to reproduce buoyancy driven currents typically occurring in coastal areas. Three-dimensionality is part of the problem although the vertical scales of motion are much smaller than the horizontal ones.

LES-COAST has been designed to face the mentioned effects. Complex geometry is treated as a combination of curvilinear structured grids (see [18]) and *Immersed Boundary Method* (IBM) as described in [13]. The curvilinear-coordinate IBM allows to merge the ability of IBM to treat complex immersed geometry with the flexibility of the curvilinear coordinates to follow the curvilinear boundaries of a physical domain.

In the implementation of the model for coastal problems we have faced interesting problems, never met in previous small scale studies. Namely, coastal applications are characterized by a very strong anisotropy, due to the fact that transport processes are significant over horizontal scales of the order of $10Km$, whereas the vertical length scales are limited by the depth of the water basin, typically of the order of $50m$. As a consequence, the ratio between the horizontal and vertical length scales is $L_H/L_V \sim O(10^2)$.

Here a brief description of the subgrid scale model is supplied. We use a mixed model composed of a scale similar part and of a eddy-viscosity one. Literature studies have shown that the well established dynamic model is not suited for large-scale flows (see [2]). This is attributed to lacking of scale invariance between the subgrid-scale stress (SGS) and the subtest-scale stress in applicative large scale flows. Moreover, the explicit filtering operation required by the dynamic evaluation of the constant can be problematic when working with immersed boundaries. An alternative choice is to move back to the Smagorinsky model, which works well in conjunction with wall-layer models and immersed boundaries. The SGS stress is expressed as the sum of an eddy viscosity part and a scale similar one as follows:

$$\tau_{SGS,ij} = -2\nu_T \overline{S}_{ij} + \overline{\overline{u}_i \overline{u}}_j - \overline{\overline{u}}_i \overline{\overline{u}}_j \qquad (1)$$

where

$$\overline{S}_{ij} = \frac{1}{2}\left(\frac{\partial \overline{u}_i}{\partial x_j} + \frac{\partial \overline{u}_j}{\partial x_i}\right) \qquad (2)$$

is the strain rate tensor. Here the symbol $\bar{\cdot}$ denotes the filtering operation, x_i is the spatial coordinate in i- direction ($i = 1, 3$ denote horizontal directions and $i = 2$ indicates the vertical direction), u_i is the velocity component, ν_T is the eddy viscosity. The scale similar part in Eq. 1 accounts for local backscatter and

anisotropy, whereas the Smagorinsky part of the model supplies most of SGS dissipation. Although the original model is isotropic, based on the assumption that the small scales tend to isotropy, this is not true in large scale environmental flows, where the SGS part of the spectrum contains a wide range of anisotropic structures. This is particularly true in coastal applications due to the anisotropy discussed above. The computational domain presents pancake-like anisotropic cells, with an aspect ratio between the horizontal and the vertical direction of about 20 : 1. The consequence is anisotropic filtering which may have a relevant impact on the first- and second-order statistics [6]. The eddy viscosity is evaluated as the product of a length scale $C\Delta$ times a velocity scale $C\Delta|\overline{S}|$, where C is a constant Δ is a length proportional to the filter width, *i.e.* the grid size. A typical value is the Deardorff length scale $\Delta = (\Delta x \Delta y \Delta z)^{1/3}$ for rectangular cells. For highly anisotropic problems, as those here discussed, such a choice would lead to an improper evaluation of the length scale and, hence, the use of an unique characteristic length is no longer pertinent [14].

A choice can be done to overcome this problem. Specifically we consider different eddy viscosities, for the vertical direction and for the horizontal ones. This approach is not new, since this is a standard technique used in large-scale ocean models, however as far as we know, this technique has never been applied in the LES contest. A common practice in geophysical fluid dynamic (Pedlosky, 1987) is to use two eddy viscosities $\nu_{T,h}$ and $\nu_{T,v}$, where the indexes h and v respectively denote the horizontal and vertical direction. Thus, the diffusive terms of the Navier-Stokes equations in the three directions can be written as:

$$F_x = \rho\nu_{t,h}\frac{\partial^2\bar{u}}{\partial x^2} + \rho\nu_{t,h}\frac{\partial^2\bar{u}}{\partial y^2} + \rho\nu_{t,v}\frac{\partial^2\bar{u}}{\partial z^2} \tag{3}$$

$$F_y = \rho\nu_{t,h}\frac{\partial^2\bar{v}}{\partial x^2} + \rho\nu_{t,h}\frac{\partial^2\bar{v}}{\partial y^2} + \rho\nu_{t,v}\frac{\partial^2\bar{v}}{\partial z^2} \tag{4}$$

$$F_z = \rho\nu_{t,h}\frac{\partial^2\bar{w}}{\partial x^2} + \rho\nu_{t,h}\frac{\partial^2\bar{w}}{\partial y^2} + \rho\nu_{t,v}\frac{\partial^2\bar{w}}{\partial z^2} \tag{5}$$

Directions x, z are on the horizontal plane; y is the vertical direction. The corresponding velocity components are u, w and v.

Although widely used, this formulation is not mathematically consistent. It takes into account just deformation and not rotation to represent the stress. But this can be done only assuming a linear proportionality with the term $\bar{S}_{ij}$, that is not true if we introduce directional eddy viscosities. A correct tensorial analysis brings to three coefficients for the eddy viscosity ([7], [10]) $\nu_{11} = \nu_{13} = \nu_{33}$, $\nu_{12} = \nu_{23}$ and ν_{22} with $\nu_{ij} = \nu_{ji}$. Using a Smagorinsky model, these terms can be expressed as:

$$\nu_{11} = L_h^2|\overline{S}_h| \tag{6}$$

$$\nu_{23} = L_v^2|\overline{S}_v| \tag{7}$$

$$\nu_{22} = L_v^2|\overline{S}_r| \tag{8}$$

with L_h and L_v proper length scales for the horizontal and vertical direction respectively, while the strain rate tensor is decomposed as follows:

$$|\overline{S}_h| = \sqrt{2(\overline{S}_{11}^2 + \overline{S}_{33}^2 + 2\overline{S}_{13}^2)} \tag{9}$$

$$|\overline{S}_v| = \sqrt{2(2\overline{S}_{12}^2 + 2\overline{S}_{23}^2)} \tag{10}$$

$$|\overline{S}_r| = \sqrt{2\overline{S}_{22}^2} \tag{11}$$

Now if we consider $\nu_{11} = \nu_{T,h}$ and $\nu_{12} = \nu_{T,v}$ the diffusive terms for the horizontal plane can be written as in Eqs. 3 and 5. For the vertical direction we have:

$$F_y = \rho\nu_{T,v}\frac{\partial^2\bar{v}}{\partial x^2} + \rho\nu_{T,v}\frac{\partial^2\bar{v}}{\partial y^2} + \rho\nu_{T,r}\frac{\partial^2\bar{v}}{\partial z^2} \tag{12}$$

where $\nu_{T,r} = \nu_{11} - 2\nu_{12} + 2\nu_{22}$. A dimensional analysis shows that $\nu_{T,r}$ is of the same order of $\nu_{T,h}$. The coefficients of the model need calibration. This is a still open issue since it is difficult to have proper test cases for calibration of this kind of model.

In coastal sea areas the upper and lower boundaries are respectively the sea surface and sea bottom. The presence of the surface mixing layer as well as of the bottom boundary layer must be properly considered because of their own importance in coastal flows. The first is due to wind-sea interaction and to the presence of surface waves that supply most of the turbulent kinetic energy to the system through shear production. The surface layer is also strongly affected by surface heat fluxes between the sea and the atmosphere. The bottom boundary layer is generated by mean and tidal currents. In shallow water problems these two layers tend to merge and to interact with each other. The computational effort to resolve these layers would be very expensive. Hence these layers are not resolved directly, but they are modeled using a wall-layer approach or directly imposing the stress at the surface. Note that this approach is fully justified by the fact that the direct resolution of the the wall layer does not make sense from a conceptual point of view in practical real-scale problems where wall and free-surface roughness play an important role.

The numerical model integrates the equations using the curvilinear-grid, fractional-step method of [18]. The source, advective and diffusive off-diagonal terms are treated explicitly through second-order Adams-Bashforth technique, the diagonal diffusive terms are treated implicitly. Spatial derivative are treated using central differences but the advective terms which are discretized using the 3rd-order accurate QUICK scheme. The pressure equation is solved using a line-SOR with line solution in the vertical direction and point iteration in the horizontal ones in conjunction with a Multigrid technique to speed up the convergence. The line-SOR procedure allows to deal efficiently with grid anisotropy when compared to the point SOR-Multigrid technique. Specifically the convergence rate has been found to increase by more than one order of magnitude when using line SOR instead of point SOR on very anisotropic grids.

The model also contains a treatment of free surface effects: specifically the effects of wave breaking and Langmuir circulations are modeled as discussed in [11].

3 Results

Two cases are here discussed, an estuarine flow and the dynamics inside a bay. The first case considers fresh water runoff from Tevere river in the Thyrrenian sea. The second case concerns with the mixing phenomena in a narrow Bay (Muggia bay) nested in the harbour area within the Gulf of Trieste. In Fig. 1 satellite images of the area investigated are shown together with the bathymetric lines for the estuarine flow. Fig. 2 shows a satellite image of the Muggia bay, while in Fig. 3 a sketch

of the boundaries for this case is depicted. Both cases cover an area of some kilometers in the horizontal plane, while in the vertical direction the maximum water depth is about 30 meters for the estuarine case and about 20 meters in the Muggia bay case.

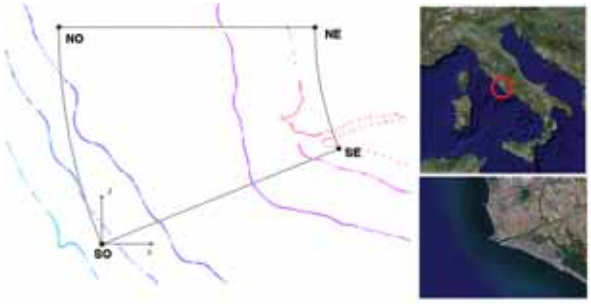

Figure 1: *Estuarine flow. Physical domain for Tevere river area. Bathymetric lines and satellite images of the area investigated.*

Figure 2: *Flow within the Muggia bay. Satellite image of the Muggia bay. The red dot indicates a point where emission of deep cold water is expected from an industrial plant.*

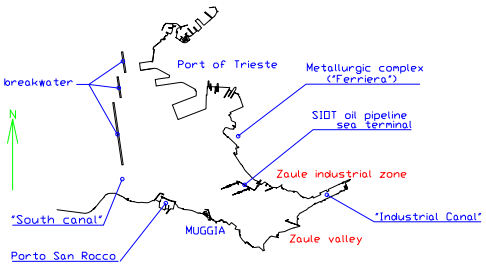

Figure 3: *Flow within the Muggia bay. Physical boundaries for Muggia bay.*

The two cases herein discussed are representative of a broad class of typical coastal problems. The geometrical complexity is present in both cases. The figures show that geometric complexity comes from the sea bottom shape, the coast line and the presence of marine structures like breakwaters and jetties. Due to the geometry and to the forcing acting on the domain the physics that can develop on this area can be very complex with fully three dimensional phenomena. In particular in these two situations we focused on the mixing effects due to density anomaly. For the river case, the most important phenomenon considered is the incoming fresh (light) water in a salt (heavy) water environment. In the second case the cold water emission is due to the hypothetical settlement of an industrial plant within the bay.

The first step to approach these problems is to move from the physical domain to the computational one. Our strategy is to use curvilinear structured grids in conjunctions with an immersed boundary method. This mixed approach allows to treat a very broad class of geometrical complexity. For example the curvilinear grid can properly describe the sea bottom and the smooth part of the coast line, while immersed bodies reproduce bluff structures or sharp contours into the domain, like the jetties in Fig. 2. The immersed boundaries can also be used to discretize the very shallow region close to the shoreline, without excessively increasing the grid anisotropy where the water depth decreases.

To build the grid it is necessary to start with bathymetric data. These data are generally sparse and they do not coincide with grid points. A scheme to interpolate the values on grid points is required. We use biharmonic spline functions as in [16]. This interpolation technique is commonly used also in commercial software.

The immersed boundary method described in [13] is used to model part of the domain. In Fig. 4 a three-dimensional view is given of the body used in Muggia bay to simulate the coast line and partially also the sea bottom surface. The figure is stretched in the vertical direction to better visualize the configuration.

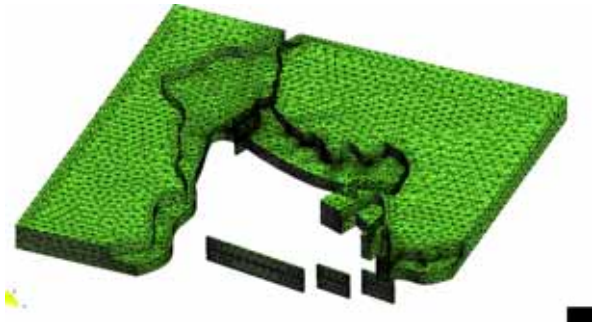

Figure 4: *Flow within the Muggia bay. 3D skecth of the immersed bodies.*

In the next sections results of the two numerical simulations are discussed.

3.1 The estuarine flow

The first study is concerned with an estuarine flow. We are interested to mixing related to the incoming flow from Tevere river in the Thyrrenian sea. This type of simulation can be useful to better understand the dynamics of the near-shore circulation. A sketch of the area is in Fig. 1.

Two main forcing terms are considered for this case: a long-shore sea current coming from south-east and the river inflow. We don't consider tidal effects or wind stress. The scales of the problem are such to make non negligible the effect of the Coriolis force over the dynamics of the river jet. In consideration of the presence of the sea current and of the Coriolis force (which deviates the jet in the northern direction), the most important area to analyze is located in the north with respect to the river's mouth. Density stratification comes from the merging of

light river water into a salt, heavier environment. Density is treated as an active scalar in the momentum equation, hence we expect upwelling of the incoming jet and consequent spreading of fresh water over the horizontal, surface, planes. We consider a typical winter condition, which gives a nearly unstratified water column. Under these conditions Reynolds analogy holds and thus the rate of turbulent diffusion of the scalar is equal to that of momentum. In other words in the advection-diffusion equation for salinity concentration we can consider a turbulent Schmidt number $Sc_T = 1$ (where $Sc_T = \nu_T/k_T$, with k_T the eddy diffusivity).

The domain considered for the numerical simulation covers an area of $5km$ x $6km$ in the horizontal plane and it is discretized with 385 grid points both along the x-direction and z-direction, while 33 points are taken in the vertical direction y. This determines cells of about ten meters in the horizontal plane and of 0.4 meters in the vertical direction close to the coastline. A sketch of a horizontal plane of the grid is in Fig. 5.

The computational grid is built starting from the bathymetry depicted in Fig. 1. In Fig. 6 a view of the bottom surface obtained through interpolation of the bathymetric data is illustrated. The sea depth reaches a maximum of 30 meters at the SO corner (see Fig. 1). Then the bottom smoothly reaches the coast line with a depth of about one meters. To avoid an excessive stretching for the grid cells in the vertical direction, part of the sea bottom up to the coast is modeled using the IBM. So at a certain level the bottom of the grid maintains a constant depth.

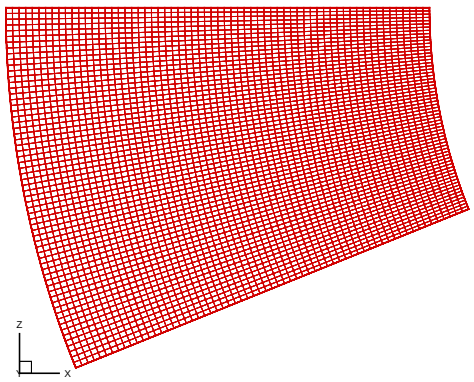

Figure 5: *Estuarine flow. Horizontal plane of a computational grid in the case of Thyrrenian simulation. For clarity a coarse resolution is shown.*

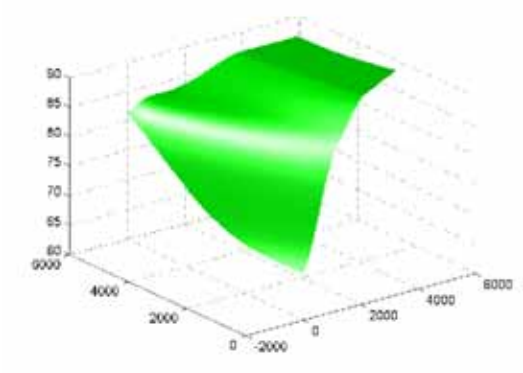

Figure 6: *Estuarine flow. Sea bottom for Thyrrenian sea in front of Tevere mouth. The grid points are interpolated from bathymetric data with a biharmonic spline.*

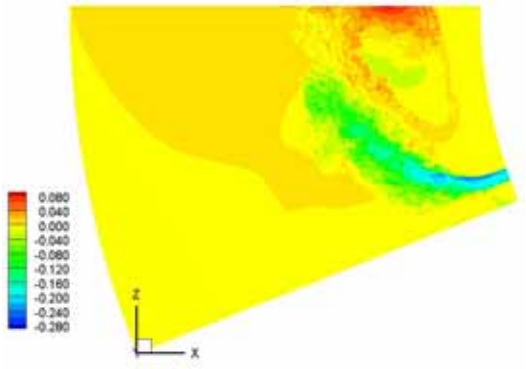

Figure 7: *Estuarine flow. Contour of u velocity (x component) one meter below the surface.*

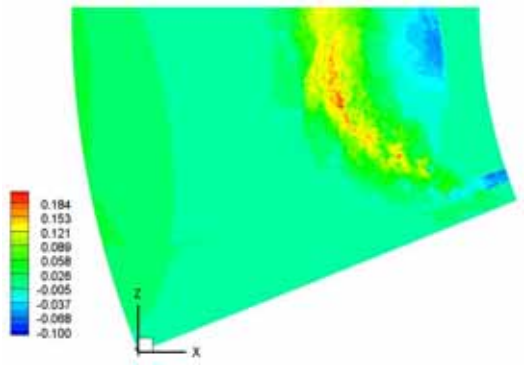

Figure 8: *Estuarine flow. Contour of w velocity (z component) one meter below the surface.*

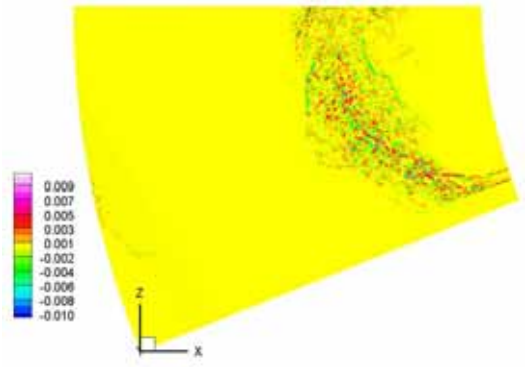

Figure 9: *Estuarine flow. Contour of v velocity (y component) one meter below the surface.*

The boundary conditions are chosen in the following way. At the solid walls (i.e. the immersed body surfaces and bottom surface) a wall-layer model is used. In the vertical boundary surface SE-SO a constant sea current of 0.02 m/s, parallel to the coast, is imposed. Few data are available for the region considered, however the general dynamics of Thyrrenian sea exhibits a near coast current going toward the north. On the boundary surface, NE-SE in correspondence to the Tevere river we consider an inflow condition. This inflow comes from a pre-simulation of a turbulent channel flow with the geometry and mass transport of the river section. The average velocity of the river is about 0.3 m/s while the flow rate is of about 300 m^3/s. This is a typical winter time value for Tevere river. The channel flow is simulated considering the Coriolis effect, and consequently the velocity profile is not symmetric with respect to the longitudinal mid-plane. A series of vertical planes of this

simulation has been stored and later on given as a turbulent inflow condition for the estuarine flow. At the sea surface we consider a shear-free condition, while at the open boundaries a radiative condition is applied.

Figure 7 shows a contouring of the west-east velocity component u. Once the river water merges into the sea river, it tends to deviate to the north due to the presence of the meridional sea current and because of the Coriolis force. The main stream remains far from the coastline and a large recirculation area is trapped between the main flow and the coast. Figure 7 also shows the asymmetric profile of the river inflow due to the Coriolis effect, namely higher velocity is observed close to the northern bank. This is because the pre-simulation of the channel flow already considers the Coriolis force. Large-scale vorticity is observed in the south-west part of the river jet, associated to the Kelvin-Helmholtz billows developing where the river water merges with the sea water.

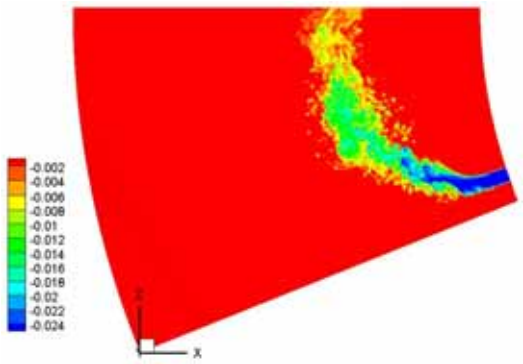

Figure 10: *Estuarine flow. Contour plot of ρ'/ρ_0 5 meters below the sea surface.*

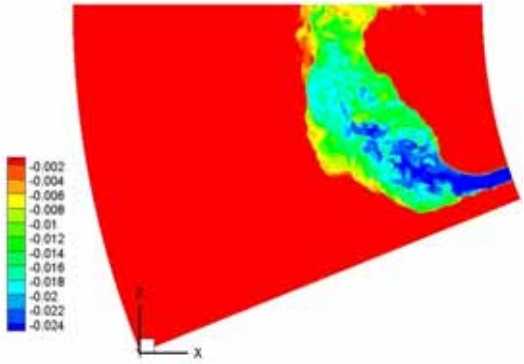

Figure 11: *Estuarine flow. Contour plot of ρ'/ρ_0 at the sea surface.*

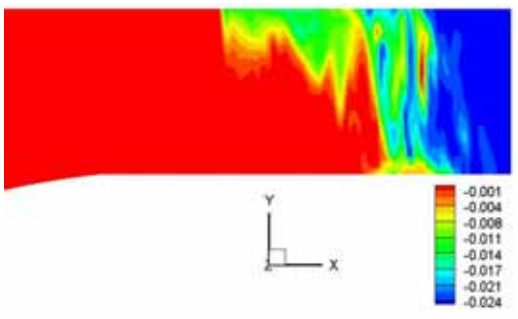

Figure 12: *Estuarine flow. Contour plot of ρ'/ρ_0 at a vertical plane along the river channel.*

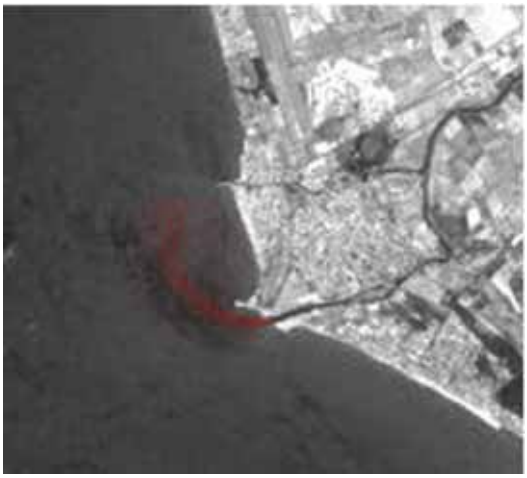

Figure 13: *Estuarine flow. Instantaneous horizontal vector field (red) obtained in our numerical simulation together with a satellite image showing the fresh water flow.*

Figure 8 shows the contouring of the south-north velocity component. The large circulation region developing between the river jet and the coast line is well evidenced.

Figure 9 shows the contouring of the vertical velocity component. Note (watch at the legend of the Figure) that the vertical velocity component is one order of magnitude smaller than the horizontal ones, and this is consistent with the order-of-magnitude analysis of the physical problem. In other words, the difference in the horizontal and vertical length scales must reflect into a similar difference in the velocity scales. Large vertical velocities are present in the central part of the river jet, where density differences are larger. These velocities are thus associated to buoyancy effects that tend to move upward the incoming fresh water.

Figures 7-9 refer to an horizontal plane one meter below the sea surface. Similar behavior is observed at other vertical stations.

The contouring of the density anomaly shows interesting features. Figures 10 and 11 show density contour plots at two different depths. The light water coming from the river, because of buoyancy tends to move upward over the salt water and to spread in the horizontal directions. The fresh water is then transported by the mean current and thus moves toward the north far from the river's mouth without reaching the coast. Figure 12 shows a typical effect, namely the salt water which move upstream toward the river mouth along its bed causing the formation of a salt-wedge.

As discussed it is very difficult to make direct comparisons with field data. In Fig. 13 a qualitative comparison between the numerical results and a satellite image of the area is presented. The results are in a pretty good qualitative agreement; however it has to be pointed out that since we are not aware of the velocity of the southern current relative to the satellite image, the comparison has the only scope to show that the simulation is able to reproduce the main features of the river jet.

3.2 Mixing in the Muggia bay

The second case considers mixing in the Muggia bay, an area near Trieste city. Here the flow is confined in a close harbour. Three breakwaters located in the western part of the bay largely reduce the water exchange with the open sea (Fig. 2). The figure also shows a red point which indicates the location of a cold water discharge

(temperature gap equal to 5 degrees with respect to the sea temperature), as designed for a future settlement of an industrial plant. We investigate the dispersion and mixing of the cold water within the bay under some typical forcing conditions. A simulation of this type can be very useful to understand the impact of an industrial discharge on the dynamics of a semi-closed sea basin.

The analysis of the main forcing terms in this area has shown that the tide does not significantly contribute to water mixing and that the primary source of mixing comes from the wind stress. For this reason we consider the wind stress acting on sea surface and the Coriolis force. In particular we consider a wind coming from south-west direction with a mean velocity $U_{10} = 4\ m/s$ measured ten meters above the sea surface. The domain covers an area of 5 kilometers in direction west-east and 4 kilometers in the direction south-north. In the present simulation we are not considering tidal effects and heat fluxes at sea surface.

As in the case of estuarine flow we do not consider background stratification and thus buoyancy effects come from the described cold water emission. Again we use Reynolds analogy and we set the turbulent Prandtl number to one ($Pr_T = \nu_T/k_T = 1$).

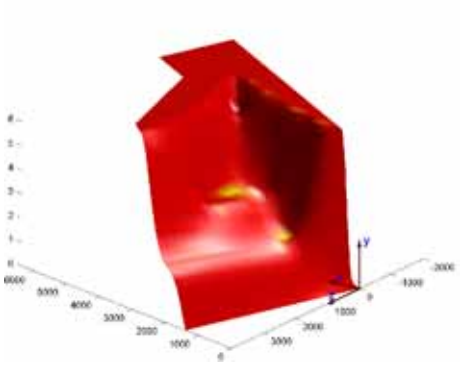

Figure 14: *Flow within the Muggia bay: Bottom surface as interpolated from bathymetric data with biharmonic splines.*

The domain is discretized with 385 points in x direction and 257 points in z direction. Finally we consider 25 points in the vertical direction y. In Fig. 14 the bottom of the grid for Muggia bay is shown. This is built from bathymetric data as done for the previous case. Boundary conditions are set similarly to the previous case.

In Fig. 15 the contour of the velocity component u two meters below the surface is shown. The water flow induced by the wind stress is blocked by the breakwaves; most of the flow entering the bay comes through the south canal and recirculate within the bay, on the rigth with respect to the Siot oil pipeline terminal (see Fig. 3); another, smaller circulation region induced by the wind stress is in the very eastern part of the bay. Near the eastern boundary the flow goes toward north-east direction then by continuity it turns west near the Siot jetties. This is the area, denoted as Zaule in Fig. 3, where the cold water emission is located. Fig. 16 contains the contouring of the other horizontal velocity component w one meter below the sea surface. The image confirms the analysis of the main circulation area described above. Besides near the coastline and in particular outside the breakwaves the velocity component w is negative. The flow is thus moving south-east that is orthogonal to the wind direction. This is a result of a downwelling phenomenon due to the combination of wind forcing and Coriolis force.

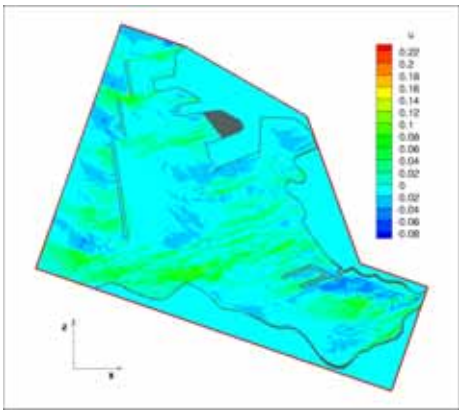

Figure 15: *Flow within the Muggia bay. Contouring of the velocity component u 2 meters below the surface.*

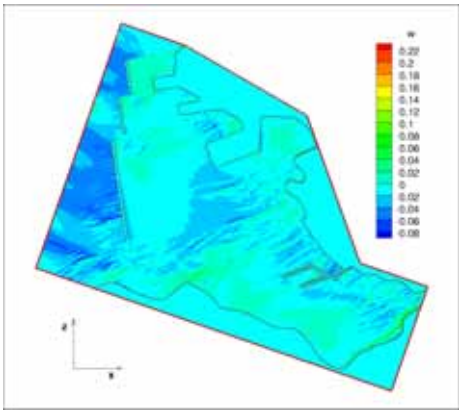

Figure 16: *Flow within the Muggia bay. Contouring of the velocity component w 1 meter below the surface.*

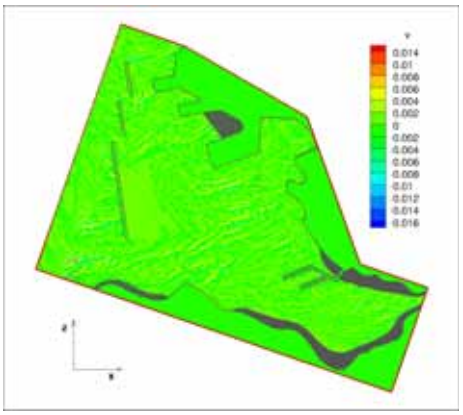

Figure 17: *Flow within the Muggia bay. Contouring of the v velocity component 7 meters below the surface.*

In Fig. 17 a contour of the vertical velocity is shown. The image refers to an horizontal plane located 7 meters below the sea surface. Turbulent structures aligned with the direction of the mean flow can be detected in the central part of the bay. As expected, the vertical velocity magnitude, is one order of magnitude smaller than the horizontal components.

Figure 18 shows the density contouring in the zone of cold water discharge. The plume follows the direction of the main flow (see Fig. 15) and it splashes against the Siot jetties. Besides, since the plume is heavier than the ambient water, it tends to move downward by gravity following the bottom slope. This can be better seen in Fig. 19 where the density contouring is reported at the level

below the discharge. The figures also show that part of the plume of cold water goes west, and this is consistent with the main circulation dynamics of the area (Fig. 16). Finally, some meters beyond the discharge location the temperature difference with respect to the reference state is small, and consequently the buoyancy effects are small and the plume is mostly advected by the mean flow.

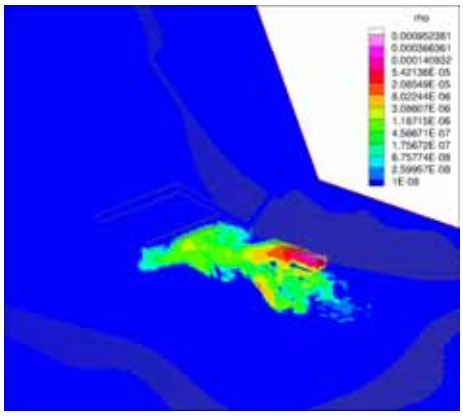

Figure 18: *Flow in the Muggia bay. Contour plot of* ρ'/ρ_0 *at the discharge level.*

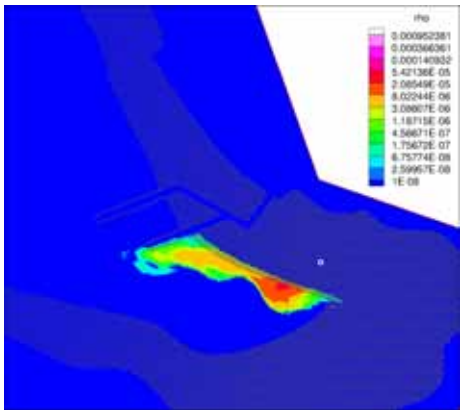

Figure 19: *Flow in the Muggia bay. Contour plot of* ρ'/ρ_0 *11 meters below the surface.*

4 Conclusions

The present note shows an application of LES methodology to large-scale marine, environmental flows. To this aim a research numerical tool, first developed for studying fundamental problems of wall-bounded turbulence, has been adapted and substantially modified. The intrinsic anisotropy arising in coastal processes, has required the modification of the SGS model, together with more sophisticated approach to treat complex geometry and the integration of the Navier-Stokes equations. The new model, LES-COAST is able to deal with very anisotropic problems, typical of coastal hydrodynamics and is able to represent the main forcing terms present in coastal environments.

We showed two applications, one relative to the Tevere river runoff in the Thyrrenian sea, and the second relative to mixing in a closed bay. The results of simulations show that the numerical model is able to reproduce very complex three-dimensional dynamics otherwise not affordable with classical two-dimensional and three dimensional RANS-like models. The model is able to give reliable estimations of plume dispersion and near-shore water circulation. Improvements are still required: for example the constant turbulent Prandtl number assumption may lead to overestimation of buoyancy fluxes in strongly stably stratified environments. Moreover lack of field measurements of turbulent quantities limits the validation of the model and thus makes difficult the proper choice of the constants of the model. Finally nesting with large-scale circulation models may be useful for setting proper boundary conditions in the LES model.

Acknowledgments

We thank Eng. G. Stipcich, who ran the simulations for the Muggia bay case. APAT is acknowledged for the financial support to the research.

References

[1] Armenio V., Piomelli U.: A Lagrangian mixed subgrid-scale model in generalized coordinates. *Flow Turbulence and Combustion*, vol. 65, 2000.

[2] Bou-Zeid E., Meneveau C., Parlange M.B.: A scale-dependent Lagrangian dynamic model for large eddy simulation of complex turbulent flows. *Physics of Fluids*, vol. 17, 2005.

[3] Burchard H., Craig P.D., Gemmrich J.R., Haren V., Mathieu P., Markus Meier H.E., Nimmo Smith A.M., Prandke H., Rippeth T.P., Skyllingstad E.D., Smyth W.D., Welsh D.J.S., Wijesekera H.W.: Observational and numerical modeling methods for quantifying coastal ocean turbulence and mixing. *Progress in oceanography*, vol. 76, pp. 399–442, 2008.

[4] Calhoun R.J., Street R. L., Koseff J.: Turbulent flow over wavy surface: stratified case. *Journal of geophysical research*, vol. 106, pp. 9295–9310, 2001.

[5] Coleman G.N., Ferziger J.H., Spalart P.R.: A numerical study of the turbulent Ekman Layer. *J. Fluid Mech.*, vol. 213, pp 313–348, 1990.

[6] Kaltenbach, H.J.: Cell aspect ratio dependence of anisotropy measures for resolved and subgrid scale stresses. *J. Comput. Phys.* , vol. 136, 399–410, 1997.

[7] Kamenkovich, V. M.: Fundamentals of ocean dynamics. *Elsevier*, 1977.

[8] Kundu P., Cohen I.: Fluid Mechanics. *Elsevier*, 2004.

[9] Lupieri G., Salon S., Armenio V.: Lagrangian dispersion in coastal applications, in Geurts, B.J.; Clercx, H.; Uijttewaal, W. (Eds.), Particle-Laden Flow -From Geophysical to Kolmogorov Scales, ERCOFTAC Series , Vol.11, Springer, The Netherlands, 2007.

[10] Mills, J.: On transversely isotropic eddy viscosity. *Journal of Physical Oceanography* , vol. 24, pp 1077–1079, 1994.

[11] Noh Y., Min H.S., Raasch S.: Large eddy simulation of the ocean mixed layer: the effects of weave breaking and Langmuir circulation.. *Int. J. Physical Oceanography*, vol. 34, pp. 720–735, 2004.

[12] Pedlosky, J.: Geophysical fluid dynamics. *Springer*, 1987.

[13] Roman F.,Napoli E., Milici B., Armenio V.: An improved Immersed Boundary Method for Curvilinear grids. Submitted 2008.

[14] Sagaut, P.: Large Eddy Simulations for incompressible flows, an introduction. *Springer Verlag*, 1998.

[15] Salon S., Armenio V., Crise A.: Large -Eddy simulation of an oscillating-rotating turbulent flow. *Proceedings, Fourth international symposium on turbulence and shear flow phenomena - TSFP4*, vol. 2, pp. 383–388, 2005.

[16] Sandwell D.T.: Biharmonic spline interpolation of GEOS-3 and SEASAT altimeter data. *Geophysical Research Letters*, 14,2, pp 139–142, 1987.

[17] Skyllingstad E. D. and Wijesekera E. D., Large-Eddy Simulation of flow over two-dimensional obstacles: high drag states and mixing. *Journal of Physical Oceanography*, vol. 34, pp 94–112, 2004.

[18] Zang Y., Street R.L., Koseff J., A non-staggered grid fractional step method for time-dependent incompressible Navier-Stokes equations in curvilinear coordinates. *J. Comput. Phys.*, vol. 114, pp 18–33, 1994.

Coherent Flow Structures in Shallow Mixing Layers

W.S.J. Uijttewaal

Delft University of Technology, The Netherlands.
w.s.j.uijttewaal@tudelft.nl

Abstract

Shallow shear flows play an important role in the transverse transport of mass and momentum in rivers. In order to understand structure of the flow and the mechanism resulting in the particular turbulence properties, three types of shallow mixing layers are investigated each with a different cause for the velocity difference: inflow conditions, bed level and bed roughness. It is shown that mixing layer properties are highly affected by the 3D turbulence generated in the bottom boundary layer. This implies that effects of subtle geometric properties like roughness variation and bed level changes should be incorporated in predictive models.

1 Introduction

Predicting the flow in rivers accurately is important for flood control, river engineering and measures that are taken for safeguarding or increasing the discharge for a given maximum water level. As rivers are rather variable regarding discharge, as well as bathymetry the flow is continuously adapting to its boundary conditions. The associated velocity gradients lead to the production of large eddies that can contribute substantially to transverse exchange of mass and momentum. It is therefore important to understand the generation mechanisms of coherent structures as well as their development. As current computational resources do not allow solving for the flow in river reaches with a resolution high enough to resolve the large eddy structures, these phenomena have to be accounted for in a simplified and parameterised model. A proper understanding of the phenomena helps in formulating these parameterisations.

Many environmental flows such as rivers are bounded in the vertical by a free surface and a bed. The vertical confinement puts constraints to the length scale by which momentum is exchanged between the bed and the water column. The properties of the bed are therefore of paramount importance for the overall flow pattern. Due to the space available, mixing lengths in the horizontal directions can however be much bigger thus allowing for more effective mixing and momentum exchange. For these large mixing lengths to develop in the presence of high dissipation the shear layer should be hydrodynamically unstable giving rise to the accumulation of kinetic energy in large eddy structures. The shallowness causes the motion of these structures to lie pre-dominantly in the horizontal plane resulting in quasi two-dimensional features.

This paper addresses the various mechanisms that govern the horizontal exchange of mass and momentum in shallow mixing layers. From the classical examples of mixing layers, wakes and jets the first one has our main interest. This is mainly because the mixing layer is found in many applications like river confluences, compound channels, groyne fields and harbour entrances, Figure 1. It is also the archetype of a simple unstable shear flow which is well studied for a large variety of conditions.

Figure 1: *View on a shallow low-land river with groyne fields and floodplains.*

2 Shallow mixing layers

The shallow mixing layers in this paper are defined as open channel flows with a transverse velocity gradient. It is shallow because the mixing layer width is generally larger than the water depth. The lateral velocity difference giving rise to the shear layer in the mean flow can have various causes depending on the specific boundary conditions:

a) *Differences in inflow velocities as it is found with river confluences, lateral expansions and side cavities*

Two regions with different streamwise velocities form a mixing layer at the interface between them [1]. With a uniform horizontal bed and a transversely uniform free-surface slope the velocity difference is disappearing gradually with downstream distance because the high-velocity side is decelerated by bed friction whereas the low velocity side is accelerated [2]. The eventual transversely uniform flow is established through friction and gravity rather than through a horizontal momentum exchange. Nevertheless, the instabilities in the shear layer develop into eddy structures that give rise to an increase in the horizontal mixing length and consequently a growth of the mixing layer width. Figure 2 shows that the mixing layer width can grow to more than 10 times the water depth over a distance of approximately 100 times the water depth.

b) *Lateral variation in water depth as it is found with compound channels with shallow floodplains and a deep main channel.*

A schematised version of a river with a high water stage, a so called compound channel flow, is depicted in figure 3. In the main channel and the flood plain two parallel streams are formed with different velocities in accor-

dance with the depth. The flow in the shallower part experiences higher friction resulting in a lower mean velocity. The interfacial shear layer leads to the formation of eddy structures that contribute to the momentum transfer from the main channel to the floodplain. Although this mixing layer looks very similar to the previous configuration the effect of the transverse depth variation is that the transverse velocity difference will not disappear with downstream distance. Furthermore, any transverse motion in the mixing layer will sense the variation in depth [4].

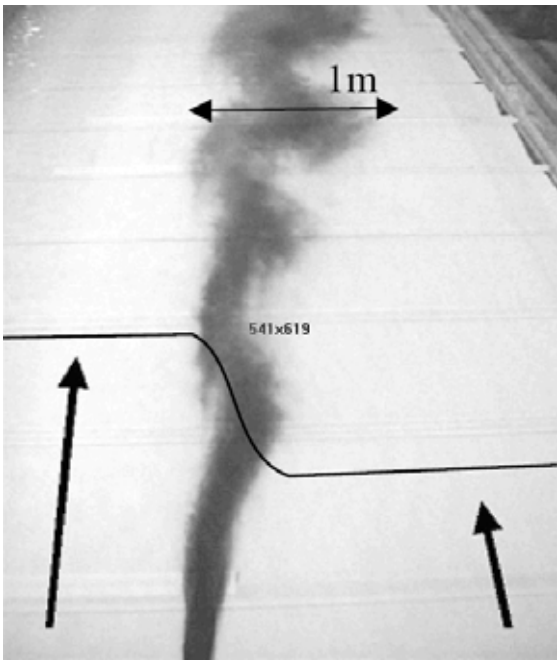

Figure 2: *Perspective view on the visualisation of a shallow mixing layer in a horizontal laboratory flume, 3m wide, 67mm deep, showing large eddies up to 1m diameter as well as the small-scale diffusive bottom turbulence [3]. The arrows indicate the mean streamwise velocities determined by inflow conditions.*

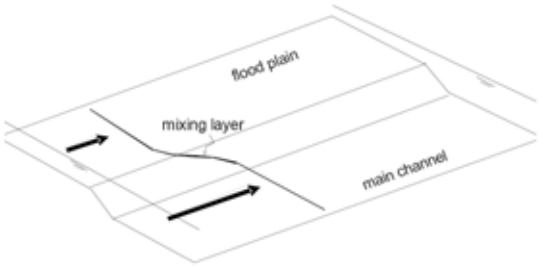

Figure 3: *Sketch of a mixing layer generated by a transverse change in water depth.*

c) *Lateral variation in bed friction due to variation in bed material, bed forms or vegetation*

In natural systems the bed is seldom smooth and roughness distributions can be heterogeneous on various scales. In order to study what happens at the transitions from hydraulically smooth to rough beds in streamwise and transverse directions a geometry was arranged as depicted in figure 4, since in comparison with a smooth bed the flow above a rough bed attains a lower mean velocity. Above the transition between the smooth and the rough bed a mixing layer develops. As with the compound channel case, at a certain downstream distance an equilibrium situation establishes for the transverse distribution of the streamwise velocity. For the case shown it is of the order of 50 times the depth. In contrast with the mixing layer of figure 2, the width of the mixing layer remains of the order of the water depth indicating that another mechanism is governing the mixing [5].

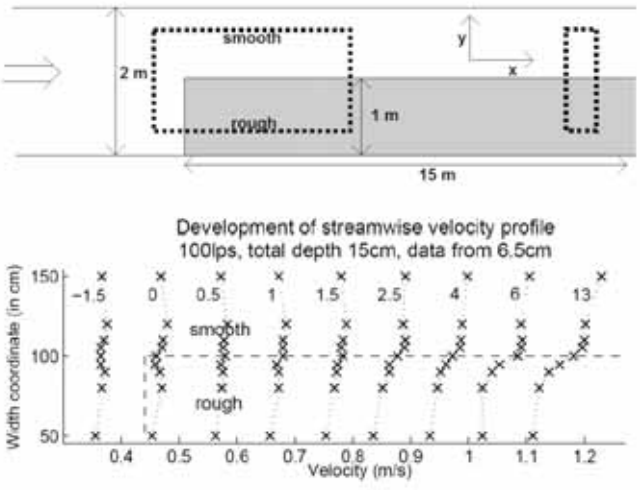

Figure 4: *Sketch of an experiment on mixing layer formation due to roughness variation. Top view of the experimental configuration (upper panel). Measured transverse profiles of streamwise velocity are labelled with downstream distance (m) and the velocity scale is shifted 0.1m/s for each curve (lower panel) [5].*

The three examples as addressed here all lead to the formation of a shallow shear layer. The development of the shear layer and the coherent structures therein will be different for each case, despite the fact that the profiles of mean velocity can look very similar.

Another complicating factor is that in natural systems of-ten a combination of the three causes is found. For ex-ample, the shallow flood plains are usually covered with vegetation whereas the deeper main channel is not. Moreover, with movable beds the roughness in the form of ripples and dunes can develop in mutual interaction with the flow thereby affecting the flow resistance.

3 Flow structures

The turbulence in the shear layer is characterised by three types of flow structures: large-scale quasi-2D eddies with vertical vorticity, small-scale 3D turbulence, and secondary circulation with streamwise vorticity. The dominance of one over the other with respect to the transfer of momentum will depend on the specific flow configuration and the turbulence generation mechanism.

3.1 Quasi-2D turbulence

Considering the shallow mixing layer of geometry 1, in its depth averaged form, the shear induced Kelvin-Helmholz instabilities result in vortex structures with vertical axes of rotation. From a linear stability analysis that includes bed shear stress and the effective eddy viscosity due to small scale 3D turbulence, a range of wave lengths can

be identified that have a positive growth rate. A structure that is advected downstream will grow in accordance with is size and the local mean velocity profile. The energy density distribution for a certain downstream position can be obtained by calculating the accumulated growth along the mixing layer for each wave length. An example of such an analysis is given in figure 5 together with experimental data [3]. It shows that the spectral distribution for the large scale motion is reasonably well predicted and that the energy level from which the structures start to grow is that of the background turbulence (indicated by the horizontal line). The latter conclusion indicates the importance of a correct representation of the disturbances that form the seedlings of the eddy structures. It was demonstrated by Van Prooijen and Uijttewaal (2008) that for a depth averaged simulation of a mixing layer the technique of kinematic simulation is an effective tool

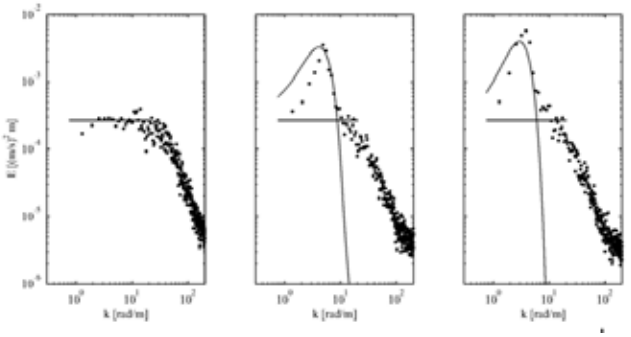

Figure 5: *Energy density spectra of a shallow mixing layer (depth=7 cm) obtained at 0, 4.5 and 10m downstream of the splitter plate. Accumulated growth rates of the stability analysis of the large scales are compared with experimental data [3].*

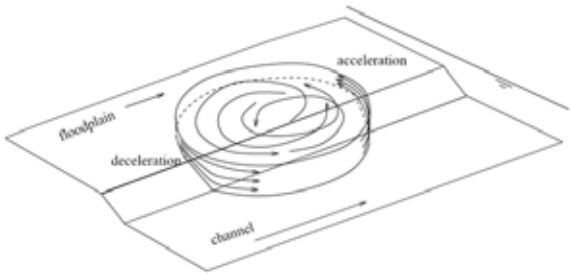

Figure 6: *A large eddy moving along the interface of a lateral depth variation [4].*

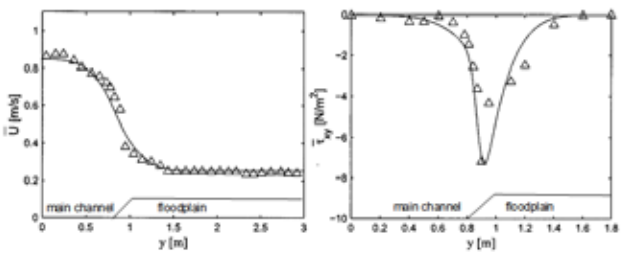

Figure 7: *Comparison of data from compound channel experiments [7] with a model that accounts for transvers depth variation [4]. Transverse profile of mean streamwise velocity (left). Profile of interfacial shear stress (right).*

3.2 Effects of transverse depth variation

As the mixing layer is found above the transition from the main channel to the flood plane any transverse motion in that area will be affected by the change in depth (Fig. 6). The vertical compression will accelerate the flow towards the flood plain and decelerate the reverse flow leading to a deformation of the eddy structures. This effect is supposed to enhance mixing proportional to the relative change in water depth [4].

Implementing this idea in a simple momentum balance produces good agreement with experimental data. Figure 7 shows that the mixing layer shape and stress distribution is well captured by the model. It should be noted that the good agreement is only an indirect justification of the model assumptions. There are no direct observations of the eddy structures in those experiments.

3.3 Heterogeneous roughness

With the two previous cases in mind one would think to find similar observations for the mixing layer caused by roughness variation. Surprisingly, no large eddy structures are found in this case. This explains why the mixing layer in figure 4 remains narrow despite the large downstream distance. Apparently the water depth determines the dominant length scale of mixing. For this configuration the transverse roughness change gives rise to a circulation cell in the plane perpendicular to the main stream. Though the magnitude of the transverse velocity is small, it is large enough to prevent mixing layer eddies to be formed.

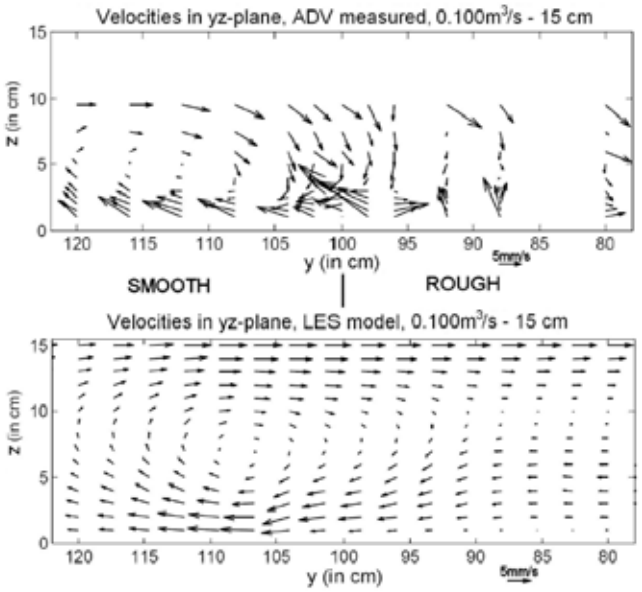

Figure 8: *Time averaged velocities in a cross-sectional plane in a developed flow over parallel lanes that differ in roughness. Top panel: ADV measurements. Lower panel: LES computations (with data interpolated to a coarse grid) [5].*

In figure 8 experimental data are compared with a Large Eddy Simulation of the flow. As the transverse velocities have a magnitude of only a few percent of the stream-wise velocities, the experimental data are a bit noisy. Furthermore the acoustical device did not allow to measure velocities in the upper 5cm of the water column. It is clear from figure 8 that near the bed at the transition the flow is pushed away from the rough towards the

smooth side. The formation of streamwise vorticity is known to occur where the anisotropy in the turbulence is strong [8]. The corner eddies in a straight open channel are examples of the same phenomenon. The strength of the cell is influenced by the abruptness of the lateral change in bed roughness. The large eddy simulation results were obtained on a domain with streamwise periodic boundary conditions and a stress-free rigid lid surface whereas the roughness was imposed in the bottom boundary conditions. As the circulation cell is bounded by the vertical dimensions of the flow the mixing layer with is also restricted to this size. Any large-scale structure that would develop in the mixing layer is advected and deformed by the circulation cell before it can attain a significant amplitude.

It is important to notice that for all cases mentioned boundary layer turbulence is present with an essentially 3D nature and a length scale typically much smaller than the water depth. This 'background' 3D-turbulence is found throughout the whole flow domain and is not restricted to the mixing layer. However it has an effect on the generation of eddy structures because it acts as a disturbance on the main flow. At the same time its dissipative character drains energy from the large eddies.

4 Conclusions

The examples of shallow mixing layers provided in this paper reveal that they can be formed under various conditions. Despite the fact that the mean streamwise velocity distribution is simple and can generally be considers as two-dimensional (i.e. uniform over the depth), subtle 3D features affect the horizontal mixing substantially. These are mainly related to the properties of the bed and the small-scale turbulence generated in the boundary layer. In order to properly predict the horizontal mixing the effects of bottom boundary layer should be represented in the modelling approach. This requires either a (large eddy) simulation with a resolution sufficiently high so that the energy containing part of the 3D turbulence spectrum is resolved, or a proper parameterisation of its effects on the large-scale flow. The former has become feasible for schematised laboratory experiments at moderate Reynolds numbers. The latter will still be necessary during the coming decades when it concerns the simulation of high Reynolds-number river flows on a prototype scale.

References

[1] Uijttewaal, W.S.J. & R. Booij Effects of shallowness on the development of free-surface mixing layers. Physics of Fluids, 12(2) 392-402, 2000

[2] Talstra, H , Uijttewaal, W.S.J. & Stelling, G.S. Emergence of large-scale coherent structures in a shallow separating flow. In RML Ferreira & ECTL Alves (Eds.), River flow 2006 (pp. 261-269). London: Taylor&Francis 2006

[3] Prooijen, B.C. van & W.S.J. Uijttewaal, A linearized model for the evolution of large-scale turbulence structures in shallow mixing layers Physics of Fluids, 14 (12), 4105-4114, 2002

[4] Prooijen, B.C. van, J.A. Battjes & W.S.J. Uijttewaal Momentum exchange in uniform compound channel flow. J. Hydraulic Engineering Vol 131(3) pp. 175-183, 2005

[5] Vermaas, D.A. Uijttewaal, W.S.J. & Hoitink, A.J.F. Effect of heterogeneous bed roughness on the mo-mentum exchange in floodplains. Proc. Int. Conf. on Fluvial Hydraulics A3.3, Cesme, Turkey, 2008

[6] Prooijen, B.C. van & W.S.J. Uijttewaal, The relevance of a back-scatter model for depth-Averaged flow simulation, Flow Turbulence and Combustion (in press), 2008

[7] Knight, D. W. & Shiono, K. Turbulence measurements in a shear layer region of a compound channel. J. Hydraul. Res., 28(2) 175-196, 1990

[8] Perkins, H.J., The formation of streamwise vorticity in turbulent flow. J. Fluid Mech. 44(4), 721-740, 1970

On the Flow of Natural Clay Suspensions over Smooth and Rough Beds

J.H. Baas[1] & J.L. Best[2]

[1] *School of Ocean Sciences, Bangor University, United Kingdom.*
[2] *Departments of Geology and Geography, University of Illinois, USA.*
j.baas@bangor.ac.uk; jimbest@illinois.edu

Abstract

The present paper describes physical experiments designed to examine the flow of natural clay-rich fluids over a smooth and rough (7mm gravel) surface. Kaolin was used as the clay in volumetric concentrations up to 15% and at a range of mean flow velocities. Results show that the presence of gravel provides an additional source of turbulence, as compared to smooth-wall flows, and that this modifies the sequence of flows transitional between turbulent and laminar, produced as clay concentration is raised. In particular, a turbulence-enhanced transitional flow, which is formed once a certain amount of clay has been added to a turbulent flow moving over a smooth bed, is absent over rough surfaces. Additionally, at a given clay concentration and the mean flow velocity of $\sim$1ms^{-1} used herein, turbulence-attenuated transitional flows are formed at a lower applied fluid shear over the smooth than the rough bed. This feature is attributed to the greater role of grain roughness in creating additional near-bed turbulence and fluid mixing over the gravel surface.

1 Introduction

Many flows within a wide range of natural environments transport sediment in suspension, and thus constitute an important class of two-phase flows. For instance, turbid flows may reach up to 60% volumetric sediment concentration in rivers such as the Huang He, China [1], whilst flows of sediment-laden water across the continental margins, as turbidity currents, provide one of the principal mechanisms for redistributing sediment into the deep ocean [2]. As such, sediment-laden flows abound in many environments, and yet much of our knowledge of the fluid mechanics, and sediment transport processes in such environments, has revolved around study of essentially 'clearwater' conditions without considering the feedbacks that exist between fluid and sediment. The assumption that clearwater flows may act as suitable surrogates for sediment-laden fluids has become increasingly tenuous in the light of recent work that has shown the considerable interaction between sediment and fluid in two-phase flows, where turbulence modulation by the sediment phase may lead to both an attenuation and enhancement of turbulence [3,4,5]. The factors that determine the presence, direction and magnitude of this turbulence modulation involve parameters such as the sediment concentration, sediment type (where clays may behave very differently to non-cohesive sediment), sediment size in relation to the scales of turbulence, and the applied fluid shear. In relation to the influence of clays, many types of clay suspended in water have cohesive properties, because electrostatic forces cause the particles to attract each other [6]. The degree of cohesion is dependent on the distribution of electrical charges at the particle surface, the distance between the particles and the fluid medium (e.g. fresh or saline water), with the surface charge being governed by chemical composition, and hence the type of clay. After two clay particles collide, they may form a larger particle, or floc [7,8,9,10]. As flocculation continues, and the flocs grow in size, the number of particles thus reduces and the probability of particles colliding with each other becomes negligible. Floc size also tends to increase with increasing bulk suspended clay concentration until a 'gelling' point may be reached, where the flocs form a pervasive, volume-filling network of particle bonds within the liquid. These particle bonds within gels can make a flow viscous and be strong enough to cause the total suppression of turbulence in flowing clay suspensions. Alternatively, the sediment-fluid mixture may undergo deflocculation if the bonds between the clay particles in flocs and gels can be broken by turbulence within the flow [10]. Hence, the viscosity and dynamic structure of natural clay-rich flows rely on the interplay between turbulent and cohesive forces.

Past work detailing the flow of kaolin-rich fluids over a smooth bed has revealed a distinct series of changes as clay concentration is increased [11,12,13,14,15] (Figure 1). Two end members exist. First, at low clay concentrations, a normal turbulent flow is present (TF; sketch (a), Figure 1) with logarithmic velocity profile and turbulence intensities reaching a maximum near the bed. At the other extreme, at high clay concentrations (the exact concentration depending on applied fluid shear and clay type), a more viscous fluid is formed as the clay particles have formed a pervasive gel. This quasi-laminar plug flow (QLPF; sketch (e), Figure 1) consists of a rigid, non-deforming plug flow that has no turbulence, which overlies and rides upon a basal shear layer. Between these two extremes lie a variety of 'transitional flows' that have very different characteristics. At low clay concentrations, a flow with enhanced turbulence near the bed has been found [12,14,15] and termed a 'turbulence-enhanced transitional flow' (TETF; sketch (b), Figure 1). The origin of this turbulence enhancement was reasoned to lie in formation of an internal shear layer just above the bed, which separated a lower, thickened viscous sublayer, from the overriding flow [14]. Along this boundary, vorticity, in the form of Kelvin-Helmholtz instabilities, creates additional turbulence that is able to penetrate a limited distance upwards in the flow before it dissipates. As clay concentration increases further, the flow becomes able to form a network of cohesive bonds that begin to form a plug flow region, with this zone initially forming in the region of lowest shear (i.e. at the flow surface; sketch (c), Figure 1). This flow was termed

a lower transitional plug flow (LTPF) by Baas et al. [15], as it contains a plug flow region near the water surface in which turbulence is virtually absent and there is no vertical gradient in streamwise velocity. However, turbulence enhancement, by the same process as outlined for the TETF above, may still be causing higher turbulence near the bed, and is accompanied by a further increase in the height of the internal shear layer above the bed. Distinct saw-tooth like time series are characteristic here (Figure 1c), and represent the formation, and advection, of vorticity generated along this shear layer. Lastly, as clay concentration further increases, the plug flow zone extends downwards as the cohesive strength of the fluid begins to dominate the bed-generated turbulence. This upper transitional plug flow (UTPF; sketch (d), Figure 1), possesses a larger plug flow region and decreased turbulence intensities throughout the entire flow depth, with the principal source of turbulence lying in shear along the basal shear layer, although this has become weaker than within the LTPF regime. Further increases in clay concentration lead to formation of a true quasi-laminar plug flow.

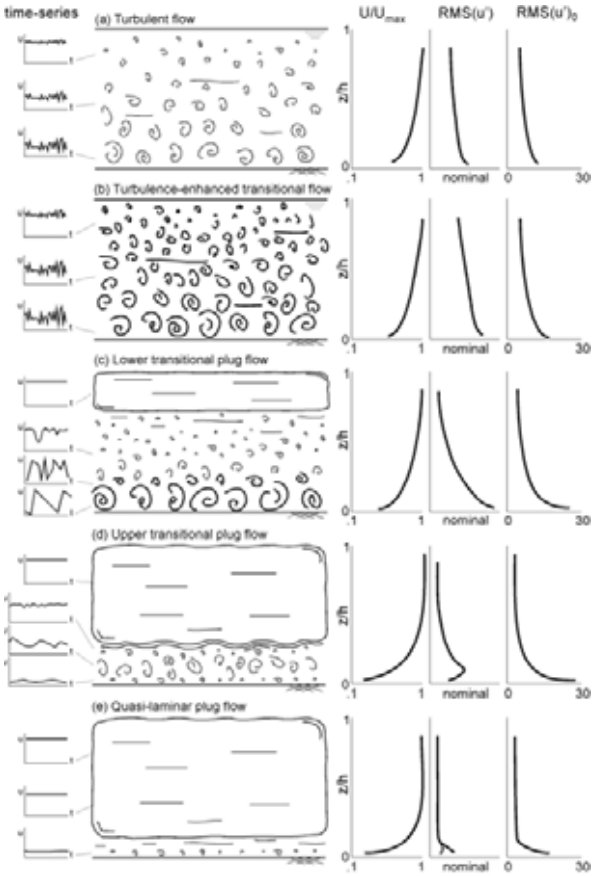

Figure 1: *Schematic vertical profiles of horizontal velocity (U/U_{max}), turbulence intensity RMS (u'), and dimensionless turbulence intensity RMS $(u')_o$, together with representative time series at different heights within the flow (left), for kaolin-flows over a smooth bed with increasing clay concentrations [a-e; from [15]; see text for explanation].*

This model of changing clay flow properties has been derived for flows moving over a completely smooth surface. However, most natural flows involve some degree of either grain or form roughness that may complicate this situation. The aim of the present study was thus to investigate the effect of gravel-scale roughness upon the development of the different flow types as progressively more clay is added to a water flow, over a range of flow velocities and flow Reynolds numbers.

2 Experimental Methodology

The laboratory methods used in the present study were similar to those used by Baas and Best [14,16] and Baas et al. [15], to which the reader is referred for fuller details, but with several modifications. The experiments were conducted in a recirculating water channel, 8.75m long, 0.30m wide and 0.30m deep, and in the current experiments the flow depth, h, was kept constant at 0.15m. The clay-rich flows were recirculated using a variable-discharge slurry pump with a non-destructive centrifugal screw mechanism. Kaolin (median particle size: 0.009mm) was used as the fine suspended sediment, with volumetric clay concentrations, C, ranging between 0.1% and 14.95% (0.4-389gL^{-1} respectively). All clay was finely dispersed within the flow and at-a-point sampling showed that no vertical gradient in sediment concentration was present within the flows [14,15].

Two beds were investigated in the present study. Firstly, clay-rich flows of different volumetric clay concentration and mean flow velocity were measured over a smooth Perspex surface, with the flow discharge being varied whilst keeping the flow depth constant [15]. Secondly, the same range of flows was studied, but the flows moved over a fixed, natural rough gravel surface. In the test section, the gravel had a mean particle size, D, of 7mm and a maximum clast size of 16mm. These flows thus have an effective roughness (h/D) of $\sim$ 21, although such values can be far lower in natural flows, for instance in natural gravel-bed rivers where values of 5-10 are common.

The instantaneous component of horizontal flow velocity was measured using ultrasonic Doppler current profiling (UDVP; see [14,15,16,17] for details). UDVP operates using the Doppler shift in ultrasound frequency as small particles pass through a measurement volume, and are particularly well-suited for measuring velocities in opaque clay-rich suspensions, if it is assumed that small clay particles follow the fluid velocity. In this study, both 2MHz and 4MHz ultrasonic Doppler velocity profilers with a diameter of 8mm were employed. Each UDVP acquired simultaneous velocity data along a profile of up to 128 points along the axis of the ultrasound beam, which in the present experiments extended up to 0.105m from the probe head. No velocities were recorded in the proximal 0.012m, where stagnation of flow by the UDVP was found to be unacceptably large. Sampling rates varied between 63 and 143Hz, and the probes were also employed in racks of up to four probes, with at least nine points being measured in each vertical profile. At each point, velocities were measured for at least 70 seconds (and in some cases up to 170 seconds) and were used to compute both the temporal horizontal mean flow velocity, $\bar{U}$, and its standard deviation, RMS(u') (RMS is the root-mean-square and u' is a fluctuation in horizontal velocity, equal to $u - \bar{U}$):

$$\bar{U} = \frac{1}{n}\sum_{i=1}^{n} u_i, \qquad \mathrm{RMS}(u') = \sqrt{\frac{1}{n}\sum_{i=1}^{n}(u_i - \bar{U})^2}$$

where n is the number of velocity measurements. The dimensionless turbulence intensity is then defined as:

$$\mathrm{RMS}(u')_0 = \frac{\mathrm{RMS}(u')}{\bar{U}} \cdot 100$$

Two hundred and fifty experiments were conducted covering mean flow velocities of between 0.13 and 1.47ms^{-1} (smooth bed) and 0.28 and 1.20ms^{-1} (gravel bed).

3 Results

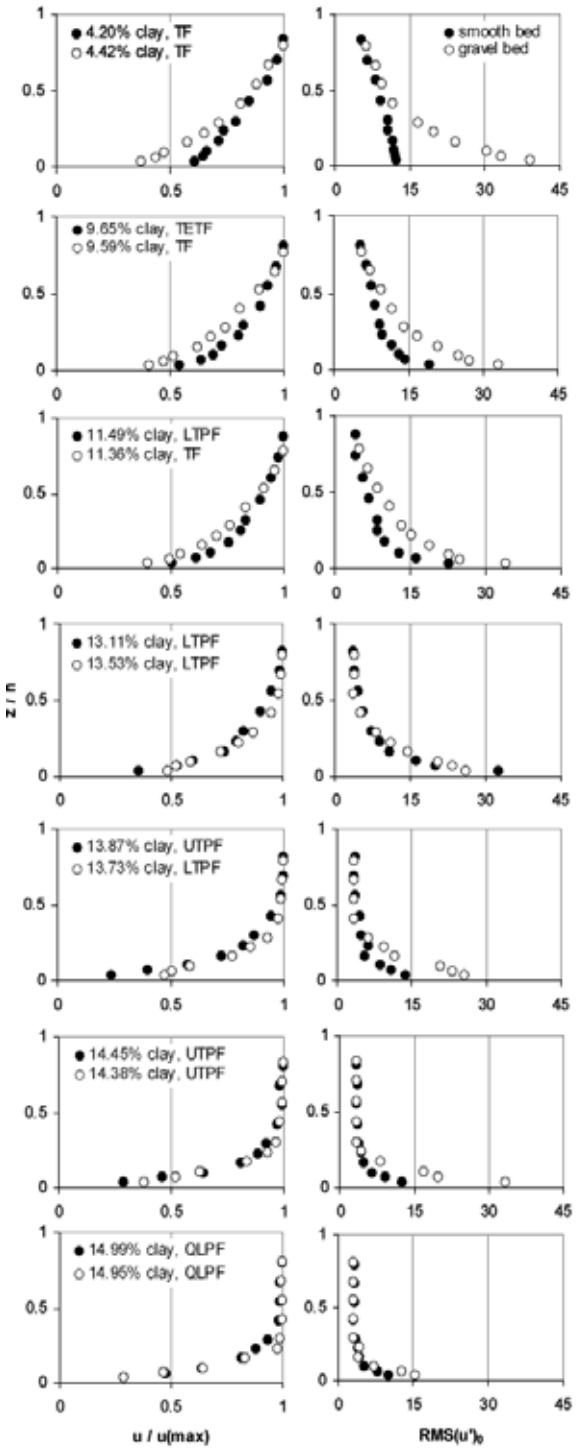

Figure 2: *Vertical profiles of downstream velocity (left) and their dimensionless turbulence intensity values (right) as a function of changing suspended clay concentration at a mean velocity of* $\sim 1ms^{-1}$.

Vertical profiles of downstream velocity (made dimensionless through division by the maximum velocity in the profile) and turbulence intensity are shown for flows with ∼1ms^{-1} at different clay concentrations in Figure 2. At C∼4%, both flows over smooth and gravel surfaces show profiles typical of a fully turbulent flow, with logarithmic velocity profiles, shear throughout the flow depth (here sampled from $0.033z/h$ to $0.83z/h$, where z is height in the flow) and with the maximum turbulence intensities near the bed. As expected, the reduction in velocity near the bed is greater over the rough surface than over a smooth wall, and also the turbulence intensity is greater than over the smooth bed. Time series of velocities collected at 5mm above the bed ($0.033z/h$; Figure 3) for both beds show a fluctuating signal with the absolute magnitude of the fluctuations being larger over the gravel bed. At C∼9.6%, although the gravel-bed profile is largely unchanged, flows over the smooth bed show a decrease in the near-wall velocities but an in-crease in the near-bed turbulence intensity as compared to C∼4% at this mean flow velocity (Figures 2 and 3). This behaviour shows the development of a turbulence-enhanced transitional flow, as previously described [14,15]. Further addition of clay to C∼11.4% again witnesses little change to the profile collected over the gravel bed, but shows the beginnings of development of a plug flow region in the upper part of the flow over the smooth bed. This is shown by the lower vertical gradient in horizontal velocity as well as by the reduced turbulence intensities at z/h>0.57. It is evident at clay concentrations up to *c.* 11.4% and at this mean flow velocity (∼1ms^{-1}) that, although turbulence modulation has occurred over the smooth bed and a plug flow is starting to develop, turbulent flow still persists over the gravel bed.

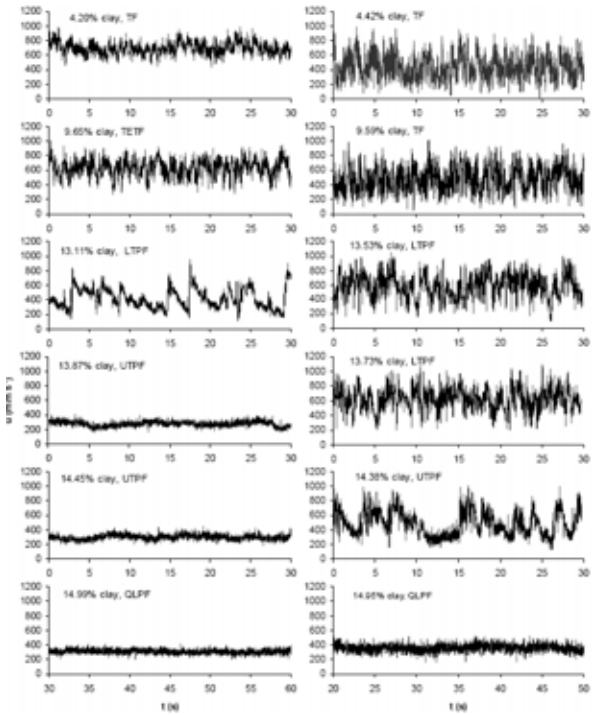

Figure 3: *Time series of horizontal velocity as 0.033z/h (5mm) for smooth (left) and gravel (right) beds for flows with a mean velocity of* $\sim 1ms^{-1}$*, and at a range of clay concentrations.*

At C ∼13.3%, the plug flow has continued to expand downwards in the flow over the smooth bed, as shown by the profiles of both velocity and turbulence intensity, which now display a region of low turbulence above $\sim 0.43z/h$. It is also noticeable that at $0.033z/h$ over the smooth bed, the time series has developed a distinct asymmetrical sawtooth pattern (Figure 3) which has been documented in past studies of both LTPFs and

UTPFs [15]. Flow over the gravel surface begins to show development of a plug flow region at this clay concentration, also with reduced turbulence intensities above $z/h \sim 0.43$. It is evident that flow over the gravel bed has passed from a turbulent flow to a transitional lower plug flow without passing through a state of turbulence enhancement as displayed over the smooth bed.

Turbulence intensities near the gravel bed are at a maximum at lower clay concentrations than near the smooth bed. Indeed, turbulence enhancement over a smooth bed in the LTPF regime may result in the turbulence intensities being higher than over a gravel bed, which lacks near-bed turbulence enhancement in the LTPF field (e.g. at C $\sim$ 13.3% in Figure 2). Addition of more clay to flows over both surfaces (C $\sim$13.8, 14.4 and 14.9%; Figures 2 and 3) continues development of the upper plug flow, with the smooth-bed flow reaching development of an upper transitional plug flow before the gravel bed. At $0.033z/h$, the smooth-bed flow possesses virtually no fluctuations at C=13.8%, but there are still marked fluctuations present above the gravel surface (Figure 3). At this concentration, the smooth-bed flow is seen to have a very flat velocity profile in the upper flow. Both flows, however, develop characteristics of an upper transitional plug flow at C $\sim$ 14.4% and have developed into a quasi-laminar plug flow by C $\sim$ 14.9%, when very few fluctuations exist in either time series at $z/h = 0.033$. It is noticeable that over the gravel bed for C $\sim$ 14.4% at $z/h = 0.033$, the time series becomes rather spiked in its appearance and that some of these large-scale fluctuations are asymmetric in form. The turbulence intensity here has risen slightly compared to C $\sim$ 13.8%, but is still below the values recorded at lower clay concentrations when the flow possessed a fully turbulent velocity profile. This time series may represent a shear layer now formed near the top of the gravel roughness, but addition of clay to C $\sim$ 14.9% subsequently dampens out this turbulence, and both flows become laminar with distinct plug flow zones with no vertical gradient in velocity and very low turbulence intensities (Figures 2 and 3).

4 The influence of bed roughness on the turbulent structure of clay-laden flows

These experiments demonstrate that the addition of clay to a turbulent flow moving over both a smooth and rough (gravel) surface causes turbulence modification and eventually development into a quasi-laminar plug flow that moves over a thin, basal shear layer. These results corroborate past work that flow over a smooth surface undergoes a series of distinct changes that show at first turbulence enhancement, possibly linked to growth of a thickened viscous sublayer and its upper shear layer [15], and then turbulence attenuation linked to growth of a region of undeforming plug flow that develops from the flow surface downwards. Flow over a rougher gravel surface develops similar flow regimes with the addition of progressively more kaolin, except that over a gravel surface: i) no regime of turbulence enhancement is found, and ii) the changes to regimes of progressive turbulence modulation are found at higher clay concentrations, for the same mean flow velocity. Previous work over smooth beds [14,15] has shown that the regimes of transitional flow move to progressively higher clay concentrations as the mean flow velocity (e.g. applied fluid shear) is increased. This was reasoned to result from the balance of cohesive to turbulent forces within the fluid: as fluid shear increases, the fluid is able to break the clay-clay particle bonds so that a greater concentration of particles is required to form the same fluid dynamic behaviour. The presence of a gravel surface can be viewed as providing an additional source of turbulence, in the form of vorticity produced by eddy shedding around individual grains or groups of grains [18,19,20,21,22]. As such, the turbulence generated by grain roughness is reasoned to provide an additional source of shear within the lower part of the boundary layer, so that the formation of clay-clay particle interactions must occur at higher clay concentrations than over a smooth bed, in order to form the same transitional flow regime. Additionally, the absence of any TETF over the gravel surface points to the inability of flow over this bed to form an internal shear layer along which vorticity, and additional turbulence, may be generated [15]. It is conjectured that the absence of this TETF regime is linked to: i) the increased vertical mixing generated by the gravel which does not allow the internal shear layer to form. Eventually, as clay concentration rises, the flow reaches a stage where the plug flow in the outer region has developed before any formation of a lower shear layer, leading to turbulence intensities declining before any near-bed internal shear layer can form; and/or ii) the fact that the 7-16mm roughness may occupy the depth of the region in which a thickened viscous sublayer may form [12,15], and thus negate its development.

At the relative grain roughness investigated in this study ($h/D \sim 21$), the bed-generated turbulence dissipates before it reaches the flow surface, but it could be expected to be more influential in providing a source of turbulence and mixing within the outer flow, as relative roughness is increased (i.e. decreasing h/D). Thus, the relative roughness of the flow may also help determine the extent to which an outer plug flow is developed in flows of a given clay concentration within the transitional flow field. The present study has investigated the role of grain roughness and found this to destroy the formation of any TETF. However, previous research concerning clay-rich flows moving over a fixed current ripple [16], which represents a small scale of form roughness, did document the occurrence of a TETF before development of a LTPF regime. However, in this case the stoss (upstream) side of the ripple provided a smooth surface over which a TETF could develop before encountering the region of flow separation in the ripple leeside. As such, the fixed ripple, with a form index (stoss:leeside length) of 5, permitted development of a TETF, whereas the present gravel surface with a far more complex, and dense, arrangement of roughness elements with a form index of *c.* unity, does not show development of any TETF regime. Future work should thus investigate both the form and density of roughness elements and the effect these may have on the presence or absence of a TETF regime.

The stability space of these flows can be examined by plotting them on a diagram using the Froude and flow Reynolds numbers for the abscissa and ordinate axes, respectively [15]. The Froude number is given by:

$$Fr = \frac{\overline{\overline{U}}}{\sqrt{gh}}$$

where $\overline{\overline{U}}$ is the depth-averaged flow velocity, h is the flow depth, and g is the acceleration due to gravity. The flow Reynolds number was calculated from:

$$Re = \frac{\overline{\overline{U}} z_p \rho}{\eta}$$

where ρ is the flow density, η is the dynamic viscosity of the flow, and z_p is the thickness of the flow region below the base of the plug flow. In this form of the flow Reynolds number, z_p is used as the length scale instead of flow depth, because the largest length scales of turbulence within the transitional and laminar clay flows are limited by the distance between the bed and the base of the plug flow region. In order words, at a specific boundary shear and flow viscosity, the position of the base of the plug flow region is considered to be independent of the flow depth, as turbulent energy cannot extend to $z > z_p$. In turbulent flows and turbulence-enhanced transitional flows, from which any plug flow region is absent, the following length scale is used in the flow Reynolds number: $z_p = h$

This *Fr-Re* diagram (Figure 4) plots the symbols for the present gravel-bed flows and the boundaries between the different flow types (solid lines), and overlies these upon the stability field for the smooth-bed flows (dashed lines). The boundaries between the fields, at different Froude numbers, appear to lie in a fairly narrow range of Reynolds numbers for this constant flow depth, and gives confidence to the calculation of Reynolds number in this manner. Three features are apparent from this plot: i) the boundaries between the fields, for both bed roughnesses, appear independent of the flow Reynolds number; ii) the turbulence-enhanced transitional flow is absent for the gravel bed, and iii) the flow over a gravel surface appears to reach a given modulation field at similar Reynolds numbers as the smooth-bed flows. This study thus illustrates that an improved understanding of the effect of differing grain and form roughnesses, at a range of applied fluid shear velocities and clay types, is required to better delineate the 3 and 4 dimensional phase-space of turbulence modulation within natural clay-rich flows. A rheological approach that encompasses changing rheology as a function of clay type, sediment concentration and applied fluid shear, may offer the best route for collapsing these data into comparable datasets.

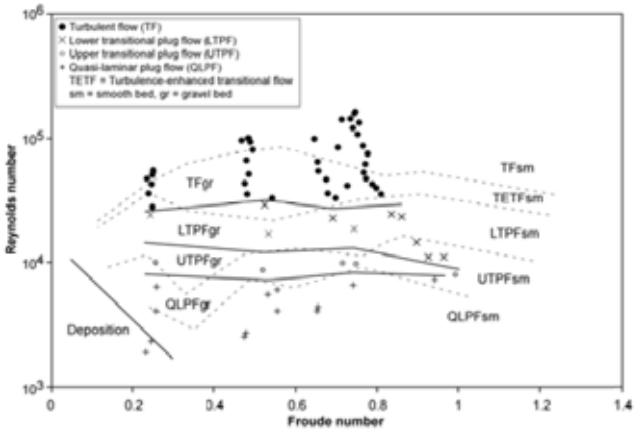

Figure 4: *Stability fields for turbulent, transitional and quasi-laminar plug flows moving over flat smooth and gravel surfaces. Phase boundaries for smooth-bed and gravel-bed flows are given by dashed and solid lines, respectively.*

5 Conclusions

This study has shown that clay-rich water flows become progressively modulated in their turbulence structure as a function of clay concentration and applied fluid shear over both smooth and rough beds. Grain roughness generates greater mixing in the near-bed flow than over a smooth bed and this appears to inhibit the formation of any turbulence-enhanced flow regime, possibly due to the inability of these rough-bed flows to generate a near-bed internal shear layer. Turbulent flows moving over rough surfaces in which the effective roughness is moderate (as here with $h/D \sim 21$) require greater clay concentrations, at the same mean flow velocity, for formation of a given regime of turbulence modulation. This characteristic is attributed to the greater clay concentrations needed to form particle-particle networks and eventually a volume-filling gel, that are required to transform a turbulent flow into a transitional plug flow and quasi-laminar plug flow. It is clear that prediction of natural, clay-laden suspensions must account for sediment concentration as well as the size, and type, of bed roughness present. Furthermore, the present experiments have only concerned fixed roughness, and the phase boundaries between the flows require investigation under fully mobile-bed conditions, where bed-suspended load interactions and possible infiltration of clay into the bed [23] may become important.

Acknowledgements

We are very grateful to the UK Natural Environment Research Council for grant NE/C514823/1 that enabled this research to be undertaken at the Sorby Environmental Fluid Dynamics Laboratory, whilst JHB and JLB were at the University of Leeds, UK. We would like to thank Bernard Geurts for the opportunity to contribute to this issue. A full table of experimental parameters for the experiments reported herein is available from the authors.

References

[1] Wan Z. and Wang, Z.Y., Hyperconcentrated flow. A.A. Balkema, Rotterdam, The Netherlands, 1994.

[2] Mulder, T. and Alexander, J., The physical character of subaqueous sedimentary density flows and their deposits. Sedimentology, 48, 269-299, 2001.

[3] Gore, R.A. and Crowe, C.T., Effect of particle size on modulating turbulent intensity. International Journal of Multiphase Flow, 15, 279-285, 1989.

[4] Elgobashi, S., On predicting particle-laden turbulent flows. Applied Scientific Research, 52, 309-329, 1994.

[5] Best, J.L., Bennett, S., Bridge, J. and Leeder, M., Turbulence modulation and particle velocities over flat sand beds at low transport rates. Journal of Hydraulic Engineering, 123, 1118-1129, 1997.

[6] Van Olphen, H., An introduction to clay colloid chemistry. 2nd Ed., John Wiley & Sons, London, 1977.

[7] Krone, R.B., A Study of Rheological Properties of Estuarine Sediments. Technical Report 638. Berkeley: Hydraulic and Sanitary Engineering Laboratory, University of California, 1963.

[8] Kranenburg, C., The fractal structure of cohesive sediment aggregates. Estuarine Coastal and Shelf Science, 39, 451-460, 1994.

[9] Merckelbach, L.M. and Kranenburg, C., Equations for effective stress and permeability of soft mud-sand mixtures. Géotechnique, 54, 235-243, 2004.

[10] Winterwerp, J.C. and Van Kesteren, W.G.M., Introduction to the physics of cohesive sediment in the marine environment. Developments in Sedimentology, 56, Elsevier UK, 2004.

[11] Wang, Z.Y. and Larsen, P., Turbulence structure of flows of water and clay suspensions with bedload. Journal of Hydraulic Engineering, 120, 577-600, 1994.

[12] Wang, Z. and Plate, E.J., A preliminary study on the turbulence structure of flows on non-Newtonian flu-id. Journal of Hydraulic Research, 34, 345-361, 1996.

[13] Wang, Z.Y., Larsen, P., Nestmann, F. and Dittrich, A., Resistance and drag reduction of flows of clay suspensions. Journal of Hydraulic Engineering, 124, 41-49, 1998.

[14] Baas, J.H. and Best, J.L., Turbulence modulation in clay-rich sediment-laden flows and some implica-tions for sediment deposition. Journal of Sedimen-tary Research, 72, 336-340, 2002.

[15] Baas, J.H., Best, J.L., Peakall, J. and Wang, M., A phase diagram for turbulent, transitional and laminar clay suspension flows, submitted to Journal of Sedimentary Research, (in review).

[16] Baas, J.H. and Best, J.L., The dynamics of turbulent, transitional and laminar clay-laden flow over a fixed current ripple. Sedimentology, 55, 635-666, 2008.

[17] Takeda, Y., Development of an ultrasound velocity profile monitor. Nuclear Engineering and Design, 126, 277-284, 1991.

[18] Buffin-Bélanger, T., and Roy, A.G., Effects of a pebble cluster on the turbulent structure of a depth-limited flow in a gravel-bed river, Geomorphology 25, 249-67, 1998.

[19] Best, J.L., Buffin-Bélanger, T., Kirkbride, A. and Reid, I., Visualisation of coherent flow structures associated with particle clusters, In: Gravel-Bed Rivers 2000 CD ROM, Special Publication of the New Zealand Hydrological Society, 2001.

[20] Hardy, R.J., Lane, S. N., Ferguson, R.I. and Parsons, D.R., Emergence of coherent flow structures over a gravel surface: A numerical experiment, Water Resources Research, 43, W03422, 2007.

[21] Papanicolaou, A.N., Diplas, P., Dancey, C.L. and Balakrishnan, M., Surface roughness effects in near-bed turbulence: implications to sediment entrainment, Journal of Hydraulic Engineering, 127, 211-218, 2001.

[22] Hardy R.J., Best, J.L., Lane, S.N. and Carbonneau P.E., Coherent flow structures in a depth-limited flow over a gravel surface: the role of near-bed turbulence and influence of Reynolds number, Journal of Geophysical Research (Earth Surface), (in press).

[23] Packman, A., Salehin, M. and Zaramella, M., Hyporheic exchange with gravel beds: basic hydrody-namic interactions and bedform-induced advective flows, Journal of Hydraulic Engineering, 130, 647-656, 2004.

ERCOFTAC Special Interest Groups

1. Large Eddy Simulation

Geurts, B.J.
University of Twente, Holland.
Tel: +31 53 489 4125
Fax: +
b.j.geurts@math.utwente.nl

4. Turbulence in Compressible Flows

Comte, P.
University of Poitiers, France.
Tel: +33 5 49 36 60 11
Fax: +33 5 49 36 60 01
Pierre.comte@tea.univ-poitiers.fr

5. Environmental CFD

Morvan, H.
University of Nottingham, England.
Tel: +44 115 846 6374
Fax: +44 115 951 3898
herve.morvan@nottingham.ac.uk

10. Transition Modelling

Dick, E.,
University of Gent, Belgium.
Tel: +32 9 264 3301
Fax: +32 9 264 3586
erik.dick@ugent.be

12. Dispersed Turbulent Two Phase Flows

Sommerfeld, M.
Martin-Luther University, Germany.
Tel: +49 3461 462 879
Fax: +49 3461 462 878
martin.sommerfeld@iw.uni-halle.de

14. Stably Stratified and Rotating Flows

Redondo, J.M.
UPC, Spain.
Tel: +34 93 401 7984
Fax: +34 93 401 6090
Redondo@fa.upc.es

15. Turbulence Modelling

Jakirlic, S.
Darmstadt University of Technology, Germany.
Tel: +49 6151 16 3554
Fax: +49 6151 16 4754
s.jakirlic@sla.tu-darmstadt.de

20. Drag Reduction and Flow Control

Choi, K-S.
University of Nottingham, England.
Tel: +44 115 9513 792
Fax: +44 115 9513 800
kwing-so-choi@nottingham.ac.uk

24. Variable Density Turbulent Flows

Anselmet, F.
IMST, France.
Tel: +33 4 91 505 439
Fax: +33 4 91 081 637
fabian.anselmet@irphe.univ-mrs.fr

28. Reactive Flows

Tomboulides, A.
Aristotle University of Thessaloniki, Greece.
Tel: +30 2310 991 306
Fax: +30 2310 991 304
ananiast@enman.auth.gr

32. Particle Image Velocimetry

Stanislas, M.
Ecole Centrale de Lille, France.
Tel: +33 3 20 337 170
Fax: +33 3 20 337 169
stanislas@ec-lille.fr

33. Transition Mechanisms, Prediction and Control

Hanifi, A.
FOI, Sweden.
Tel: +46 8 5550 4334
Fax: +46 8 5550 3481
ardeshir.hanifi@foi.se

34. Design Optimisation

Giannakoglou, K.
NTUA, Greece.
Tel: +30 210 772 1636
Fax: +30 210 772 3789
kgianna@central.ntua.gr

35. Multipoint Turbulence Structure and Modelling

Cambon, C.
ECL Ecully, France.
Tel: +33 4 72 186 161
Fax: +33 4 78 647 145
claude.cambon@ec-lyon.fr

36. Swirling Flows

Braza, M.
IMFT, France.
Tel: +33 5 61 285 839
Fax: +33 5 61 285 899
braza@imft.fr

37. Bio-Fluid Mechanics

Van Steenhoven, A.A.
Eindhoven University of Technology, Holland.
Tel: +31 40 2472 722
Fax: +31 40 2433 445
a.a.v.steenhoven@wtb.tue.nl

38. Microfluids and Micro Heat Transfer

Tardu, S.
Laboratoire des Ecoulements Géophysiques et Industriels, France.
sedat.tardu@hmg.inpg.fr

39. Aeroacoustics

Juvé, D.
Ecole Centrale de Lyon, France.
Tel: +33 4 72 186 429
Fax: +33 4 78 331 140
denyse.juve@ec-lyon.fr

40. Smoothed Particle Hydrodynamics

Violeau, D.
EDF, France.
Tel: +33 1 30 87 78 31
Fax:
damien.violeau@edf.fr

41. Fluid Structure Interaction

Longatte, E.
EDF, France.
Tel: +33 1 30 87 80 87
Fax: +33 1 30 87 77 27
elisabeth.longatte@edf.fr

42. Synthetic Models in Turbulence

Nicolleau, F.
University of Sheffield, England.
Tel: +44 114 22 27867
Fax: +44 114 22 27890
f.nicolleau@sheffield.ac.uk

43. Fibre Suspension Flows

Hämäläinen, J.
University of Kuopio, Finland.
Tel: +358 17 162279
Fax: +358 17 162585
jari.hamalainen@uku.fi

101. Quality and Trust in Industrial CFD

Hutton, A.G.
Airbus UK, England.
Tel: +44 117 936 7519
Fax:
anthony.hutton@airbus.com

102. ERCOFTAC Database Interests Group

Laurence, D.
UMIST, England.
Tel: +44 161 200 3704
Fax: +44 161 200 3723
dominique.laurence@manchester.ac.uk

ERCOFTAC Pilot Centres

Austria – Hungary – Slovenia

Kuhlmann, H.
Vienna University of Technology,
Inst. of Fluid Mech. & Heat Transfer,
Resslgasse 3/1/2,
A-1040 Vienna,
Austria.
Tel: +43 1 58801 32212
Fax: +43 1 58801 32298
h.kuhlmann@fluid.tuwien.ac.at

Belgium

Geuzaine, P.
Cenaero,
CFD Multi-physics Group,
Rue des Frères Wright 29,
B-6041 Gosselies,
Belgium.
Tel: +32 71 919 330
philippe.geuzaine@cenaero.be

Czech Republic

Bodnar, T.
Institute of Thermomechanics AS CR,
5 Dolejskova,
CZ-18200 Praha 8,
Czech Republic.

Tel: +420 224 357 548
Fax: +420 224 920 677
bodnar@marian.fsik.cvut.cz

France – Henri Bénard

Cambon, C.
Ecole Centrale de Lyon.
LMFA,
B.P. 163,
F-69131 Ecully Cedex,
France.
Tel: +33 4 72 18 6161
Fax: +33 4 78 64 7145
claude.cambon@ec-lyon.fr

France South

Braza, M.
IMF Toulouse,
CNRS UMR – 5502,
Allée du Prof. Camille Soula 1,
F-31400 Toulouse Cedex,
France.
Tel: +33 5 61 28 5839
Fax: +33 5 61 28 5899
marianna.braza@imft.fr

France West

Bonnet, J-P.
Université de Poitiers,
Centre d'Etudes Aérodyn. et Thermiques,
43 Route de l'Aérodrome,
F-86036 Poitiers Cedex,
France.
Tel: +33 5 49 36 60 31
Fax: +33 5 49 45 60 01
jean-paul.bonnet@univ-poitiers.fr

Germany North

Gauger, N.
German Aerospace Center – DLR,
Institute of Aerodynamics,
Lilienthalplatz 7,
D-38108 Braunschweig,
Germany.
Tel: +49 531 295 3339
Fax: +49 531 295 2914
nicolas.gauger@dlr.de

Germany South

Menter, F.
ANSYS Germany,
Staudenfeldweg 12,
D-83624 Otterfing,
Germany.

Tel: +49 8024 905 415
Fax: +49 8024 905 417
florian.menter@ansys.com

Germany West

Schröder, W.
RWTH – Aachen,
Institute of Aerodynamics,
D-52062 Aachen,
Germany.

Tel: +49 241 809 5410
Fax: +49 241 809 2257
ek@aia.rwth-aachen.de

Greece

Papailiou, K.D.
National Tech. University of Athens,
Laboratory of Thermal Turbomachines,
9 Iroon Polytechniou,
P.O. Box 64069,
Gr-15710 Athens, Greece.
Tel: +30 210 772 1634
Fax: +30 210 772 1658
kpapail@ltt.ntua.gr

Iberian East

Onate, E.
Universitat Politecnica de Catalunya,
Edificio C-1, Campus Norte,
Gran Capitan s/n,
E-08034 Barcelona,
Spain.
Tel: +34 93 401 6035
Fax: +34 93 401 6517
onate@cimne.upc.es

Iberian West

Theofilis, V.
Universidad Politécnica de Madrid,
Plaza Cardenal Cisneros 3,
E-28040 Madrid,
Spain.

Tel: +34 91 336 3291
Fax: +34 91 336 6371
vassilis@torroja.dmt.upm.es

Italy

Martelli, F.
University of Florence,
Department of Energy,
Via Santa Marta 3,
I-50139 Firenze,
Italy.
Tel: +39 055 479 6237
Fax: +39 055 479 6342
francesco.martelli@unifi.it

Nordic

Wallin, S.
Swedish Defence Research Agency FOI,
Computational Physics,
S-16490 Stockholm,
Sweden.

Tel: +46 8 5550 3184
Fax: +46 8 5550 3062
stefan.wallin@foi.se

Poland

Drobniak, S.
Technical University of Czestochowa,
Thermal Machinery Institute,
Al. A. Krajowej 21,
PL-42200 Czestochowa,
Poland.
Tel: +48 34 325 0507
Fax: +48 34 325 0555
drobniak@imc.pcz.czest.pl

Switzerland

Rudolf von Rohr, P.
ETH Zürich,
Institute of Process Engineering,
Sonneggstrasse 3, ML H 19,
CH-8092 Zürich,
Switzerland.
Tel: +41 44 632 2488
Fax: +41 44 632 1325
vonrohr@ipe.mavt.ethz.ch

Netherlands

Ooms, G.
J.M. Burgerscentrum,
Research School for Fluid Mechanics,
Mekelweg 2,
NL-2628 CD Delft,
Netherlands.
Tel: +31 15 278 1176
Fax: +31 15 278 2979
g.ooms@wbmt.tudelft.nl

United Kingdom

Standingford, D.
BAE Systems,
ATC – Sowerby, FPC 267,
P.O. Box 5,
Bristol BS34 7QW,
England.
Tel: +44 117 302 8253
Fax: +44 117 302 8007
david.standingford@baesystems.com

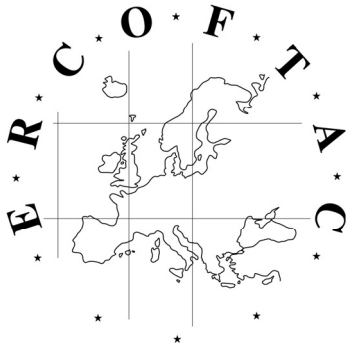

The ERCOFTAC Best Practice Guidelines for Industrial Computational Fluid Dynamics

The Best Practice Guidelines (BPG) were commissioned by ERCOFTAC following an extensive consultation with European industry which revealed an urgent demand for such a document. The first edition was completed in January 2000 and constitutes generic advice on how to carry out quality CFD calculations. The BPG therefore address mesh design; construction of numerical boundary conditions where problem data is uncertain; mesh and model sensitivity checks; distinction between numerical and turbulence model inadequacy; preliminary information regarding the limitations of turbulence models etc. The aim is to encourage a common best practice by virtue of which separate analyses of the same problem, using the same model physics, should produce consistent results. Input and advice was sought from a wide cross-section of CFD specialists, eminent academics, end-users and, (particularly important) the leading commercial code vendors established in Europe. Thus, the final document can be considered to represent the consensus view of the European CFD community.

Inevitably, the Guidelines cannot cover every aspect of CFD in detail. They are intended to offer roughly those 20% of the most important general rules of advice that cover roughly 80% of the problems likely to be encountered. As such, they constitute essential information for the novice user and provide a basis for quality management and regulation of safety submissions which rely on CFD. Experience has also shown that they can often provide useful advice for the more experienced user. The technical content is limited to single-phase, compressible and incompressible, steady and unsteady, turbulent and laminar flow with and without heat transfer. Versions which are customised to other aspects of CFD (the remaining 20% of problems) are planned for the future.

The seven principle chapters of the document address numerical, convergence and round-off errors; turbulence modelling; application uncertainties; user errors; code errors; validation and sensitivity tests for CFD models and finally examples of the BPG applied in practice. In the first six of these, each of the different sources of error and uncertainty are examined and discussed, including references to important books, articles and reviews. Following the discussion sections, short simple bullet-point statements of advice are listed which provide clear guidance and are easily understandable without elaborate mathematics. As an illustrative example, an extract dealing with the use of turbulent wall functions is given below:

- Check that the correct form of the wall function is being used to take into account the wall roughness. An equivalent roughness height and a modified multiplier in the law of the wall must be used.
- Check the upper limit on $y+$. In the case of moderate Reynolds number, where the boundary layer only extends to $y+$ of 300 to 500, there is no chance of accurately resolving the boundary layer if the first integration point is placed at a location with the value of $y+$ of 100.
- Check the lower limit of $y+$. In the commonly used applications of wall functions, the meshing should be arranged so that the values of $y+$ at all the wall-adjacent integration points is only slightly above the recommended lower limit given by the code developers, typically between 20 and 30 (the form usually assumed for the wall functions is not valid much below these values). This procedure offers the best chances to resolve the turbulent portion of the boundary layer. It should be noted that this criterion is impossible to satisfy close to separation or reattachment zones unless $y+$ is based upon $y*$.
- Exercise care when calculating the flow using different schemes or different codes with wall functions on the same mesh. Cell centred schemes have their integration points at different locations in a mesh cell than cell vertex schemes. Thus the $y+$ value associated with a wall-adjacent cell differs according to which scheme is being used on the mesh.
- Check the resolution of the boundary layer. If boundary layer effects are important, it is recommended that the resolution of the boundary layer is checked after the computation. This can be achieved by a plot of the ratio between the turbulent to the molecular viscosity, which is high inside the boundary layer. Adequate boundary layer resolution requires at least 8-10 points in the layer.

All such statements of advice are gathered together at the end of the document to provide a 'Best Practice Checklist'. The examples chapter provides detailed expositions of eight test cases each one calculated by a code vendor (viz FLUENT, AEA Technology, Computational Dynamics, NUMECA) or code developer (viz Electricité de France, CEA, British Energy) and each of which highlights one or more specific points of advice arising in the BPG. These test cases range from natural convection in a cavity through to flow in a low speed centrifugal compressor and in an internal combustion engine valve.

Copies of the Best Practice Guidelines can be acquired from:

Ms. Anne Laurent,
ADO-Ercoftac,
Avn. Franklin Roosevelt 5
B-1050 Brussels, Belgium.

Tel: +32 2 642 2800, Fax: +32 3 647 9398
Email: anne.laurent@ercoftac.be

The price per copy (not including postage) is:

Non-ERCOFTAC members:	150 Euros
Non-ERCOFTAC academics:	75 Euros
ERCOFTAC members:	100 Euros
ERCOFTAC academic members:	50 Euros